METAL-TO-LIGAND CHARGE TRANSFER (MLCT) EXCITED STATES OF RUTHENIUM POLYPYRIDYL COMPOUNDS RELEVANT TO DYE-SENSITIZED SOLAR CELLS (DSSCs)

by

Ryan M. O'Donnell

A dissertation submitted to Johns Hopkins University in conformity with the requirements for the degree of Doctor of Philosophy

Baltimore, Maryland

November, 2014

Abstract

Climate change is of increasing global concern and has stimulated the development of alternative renewable energy sources. Dye-sensitized solar cells (DSSCs) are a promising third generation photovoltaic technology due to their low manufacturing costs, spectral tunability, flexibility, and potential for residential and commercial building integration. DSSCs employ ruthenium polypyridyl compounds to sensitize wide-bandgap semiconductors, typically titanium dioxide, to visible light. The aforementioned topics are introduced in Chapter 1. This thesis will elucidate the fate of metal-to-ligand charge transfer (MLCT) excited states of ruthenium polypyridyl compounds both in fluid solution and anchored to mesoporous metal oxide thin films and relate the findings to DSSCs.

Chapter 2 describes the excited state relaxation pathways of ruthenium polypyridyl compounds containing isothiocyanate groups. This research demonstrates that the activation energy associated with ligand loss photochemistry in fluid solution increases significantly once the compounds are anchored to TiO_2 or ZrO_2 thin films and helps to explain the remarkable photostability of DSSCs.

Chapter 3 begins by reviewing Stark effects observed at semiconductor-sensitizer interfaces. Excited state electron injection into titanium dioxide nanocrystals generates an interfacial electric field which perturbs the MLCT excited states of surface-bound sensitizers. Experimental measurements on the charge screening of interfacial electric fields by monovalent and divalent Lewis acidic metal cations are presented. The compound $[Ru^{II}(dtb)_2(dcbH_2)]^{2+}$, where dtb is 4,4'-di-*tert*-butyl-2,2'-bipyridine and dcb is 2,2'-bipyridine-4,4'-dicarboxylic acid, was used to quantify the magnitude of these fields in the presence of different cations and the charge-screening kinetics of the cations following excited state electron injection.

Chapter 4 presents kinetic studies performed in the presence of the triiodide redox mediator, I_3^-, which provide compelling evidence that the anionic nature of I_3^- inhibits unwanted charge recombination in DSSCs.

Chapter 5 presents the excited state acid-base reactions of $[Ru^{II}(dtb)_2(dcbH_2)]^{2+}$ and $[Ru^{II}(btfmb)_2(dcbH_2)]^{2+}$, where btfmb is 4,4'-bis(trifluoromethyl)-2,2'-bipyridine. Although the protonatable ligand, $dcbH_2$, was identical for both compounds, it was found that the ancillary ligands could tune the excited state to be either more acidic ($pK_a^* = 2.0$ for btfmb) or basic ($pK_a^* = 3.8$ for dtb) than the ground state ($pK_a = 2.9$ for both compounds).

Thesis Committee: Gerald J. Meyer (Advisor), Kenneth D. Karlin, D. Howard Fairbrother

Acknowledgments

I am eternally grateful to the wonderful characters who have inspired, challenged, and supported me during my academic career.

My chemistry research career began as a freshman undergraduate at Ohio University thanks to Dr. Peter de B. Harrington who was gracious enough to let me research forensic applications of ion mobility spectrometry in his labs. I would like to thank my undergraduate academic advisor Dr. Lauren McMills for her guidance and for teaching me the value of scientific outreach. I owe my love for inorganic photochemistry and synthesis to Dr. Jeff Rack who allowed me to research photochromic ruthenium sulfoxide complexes in his labs during my junior and senior years.

I am thankful for the research independence that Dr. Jerry Meyer, my graduate research advisor, has provided and for the characteristics of a careful and diligent scientist that he embodies. Dr. Meyer has cultivated a remarkable research group filled with diverse and talented individuals whom I am fortunate to have worked with and to call my friends. I am especially thankful for the mentorship that Dr. Patrik Johansson provided when I first joined the lab and our friendship that ensued. My academic cohort Dr. Ke Hu has been a wonderful friend and an excellent springboard for ideas. The research atmosphere was always fun and enjoyable thanks to my lab mates: Dr. John Rowley, Dr. Byron Farnum, Dr. Patrik Johansson, Dr. Darren Achey, Dr. Atefeh Taheri, Dr. William Ward, Dr. Ke Hu, Dr. Renato Sampaio, Dr. Guocan Li, Dr. Cassandra Ward, Erinn Brigham, Tim Barr, Evan Beauvilliers, Brian DiMarco, Tyler Motley, and Wesley Swords. My thesis committee, Dr. Ken Karlin and Dr. Howard Fairbrother, have been excellent scientific role models and I thank them for their time and assistance. I would like to thank the National Science

Foundation (NSF) for financially supporting my doctoral studies through the Graduate Research Fellowship Program (GRFP).

The "Eureka!" moments of graduate research are sporadic but extraordinary and result from frequent encounters with failed experiments and incremental progress. A special thanks go out to the friends who helped me keep perspective along the way by providing intellectual stimulation, laughter and all-around good company: Tod Grusenmeyer, Kevin O'Banion, Logan Wise, Emily Bacha, David Goodwin, Katie Holmes, John Sheckelton, Steven Bloom, Heather Neu, and Jesse Neu. My Baltimore friends made Charm City feel like home and I consider them all family.

My mother, Joni, and my father, Tim, are a continual source of encouragement and a lifelong inspiration. Through example, they taught me the benefit of a hard work ethic and strong moral values. Their devotion to their profession as family physicians motivates me to follow my passion while reminding me to give back to the community that has provided so many opportunities. My sister Erin reminds me that acting your age is not everything and impresses me with the good she accomplishes as an educator. I am lucky to have married into a caring family who I enjoy being around. My in-laws, Jim and Patty, and their son, JC, treat me as if I have always been a part of the family. My dog, Molly B. Denum, has provided many smiles and sources of entertainment for the whole family.

The love and support that my beautiful wife and best friend Christine provides cannot be overstated. Her selflessness, strong work ethic, and inquisitive nature are traits I seek to emulate. She is an excellent partner who knows how to make me laugh, helps me to achieve my goals, and inspires me to be the best version of myself. I look forward to the future that we will build together.

Table of Contents

List of Figures

List of Tables

Chapter 1. The Need for Renewable Energy and the Prospect of Dye-Sensitized Solar Cells (DSSCs)

1.1 Global Energy Demand

The global demand for energy is perpetually increasing and necessitates the development of sustainable, renewable energy resources. Global energy consumption in 2010 was 150 petawatt hours (PWh) and is expected to increase to 185 PWh by 2020 and to 240 PWh by 2040.[1-2] In 2010, the United States alone used 3.9 terawatt hours (TWh) of electricity accounting for 21% of the global total, 18.5 TWh.[3] The United States uses a disproportionate amount of global energy considering that in 2010 the American population of 309 million individuals constituted less than 5% of the global population, totaling 6.87 billion people.[4-5]

While the largest portion of American energy consumption occurs in the transportation sector, 27% of the total, the prodigious increase in electronic device usage indicates that we should be concerned about electricity consumption and thus electricity generation on a much broader scale.[6] In 2013, the average American individual owned 5.4 internet connected devices and that number is predicted to reach 9.3 by 2018. Globally, the average of 1.7 internet connected devices per capita in 2013 is predicted to increase to 2.7 by 2018.[7] An assessment of electronic devices connected to the internet concluded that sometime between 2008 and 2009 the number of those devices surpassed the world population.[8] It is clear that the number of electronic items owned per individual will only continue to increase with further advancement of entertainment devices and the connection of “smart” household appliances to the internet. This growth is expected to be a global phenomenon as device costs decrease and developing countries attain higher standards of living. Although efforts are underway to manufacture more efficient electronic goods, the sheer number of devices and their increasing complexity suggests that energy consumption will continue to increase on a domestic and global scale.

1.2 Global Climate Change

An undesirable consequence of traditional energy generation is the release of large quantities of carbon dioxide as a combustion byproduct. According to the United States Energy Information Administration, roughly 0.5 to 1.0 kg of carbon dioxide is released per kilowatt hour (kWh) of electricity used depending on the power source, i.e. coal versus natural gas.[9] In 2012, the average American household was responsible for the release of approximately 8,000 kg of carbon dioxide due to an average annual consumption of 10,837 kWh of electricity.[10]

Society should be concerned with the environmental effects of releasing unprecedented amounts of carbon dioxide into the earth’s atmosphere. Carbon dioxide is a classic greenhouse gas that trap heat by absorbing the thermal energy emitted from the earth’s surface.[11] Alarmingly, atmospheric carbon dioxide concentrations are well above historical values and each year continues to bring record-setting levels. Prior to 1915, the atmospheric carbon dioxide concentration had never exceeded 300 parts per million (ppm). Yet, between April and July of 2014 the concentration level surpassed 400 ppm for the first time in history. The annual carbon dioxide concentration is shown in Figure 1.1 using public datasets available from the National Oceanic and Atmospheric Administration (NOAA) Earth System Research Laboratory and the Scripps CO_2 Program.[12-14]

Analysis of air contained in Antarctic ice cores established a correlation between atmospheric carbon dioxide concentration and temperature spanning the past 800,000 years.[15] Global changes in temperature patterns, commonly referred to as global warming, are attributed to the increasing levels of carbon dioxide in the atmosphere. The observed, globally averaged temperature anomaly is shown in Figure 1.2.A as annual or decadal averages from 1850 to 2012. A clear, increasing trend can be seen in the temperature anomaly data with record values observed near present day. The observed change in surface temperature from 1901 to 2012 is mapped onto the earth in Figure 1.2.B and depicts temperature increases as large as 2.5 °C over the 111 year time span.[16]. The map highlights the widespread impact of these temperature changes on the international community. Unfortunately, the term "global warming" does not adequately address the full implications of global climate change and may give the public an inadequate understanding of the situation. In addition to fewer cold days and nights, global climate change also encompasses extreme weather events such as increases in the intensity, duration, and frequency of heavy precipitation events, heat waves, droughts, and tropical cyclones.[16] The Intergovernmental Panel on Climate Change stated that "it is *extremely likely* that human influence has been the dominant cause of the observed warming [of the atmosphere and the ocean] since the mid-20th century."[16] While the majority of scientists are in agreement that anthropogenic climate change is occurring due to the combustion of fossil fuels and the subsequent release of carbon dioxide, there has been much debate in the media and in the public sphere as to how society should deal with this issue.

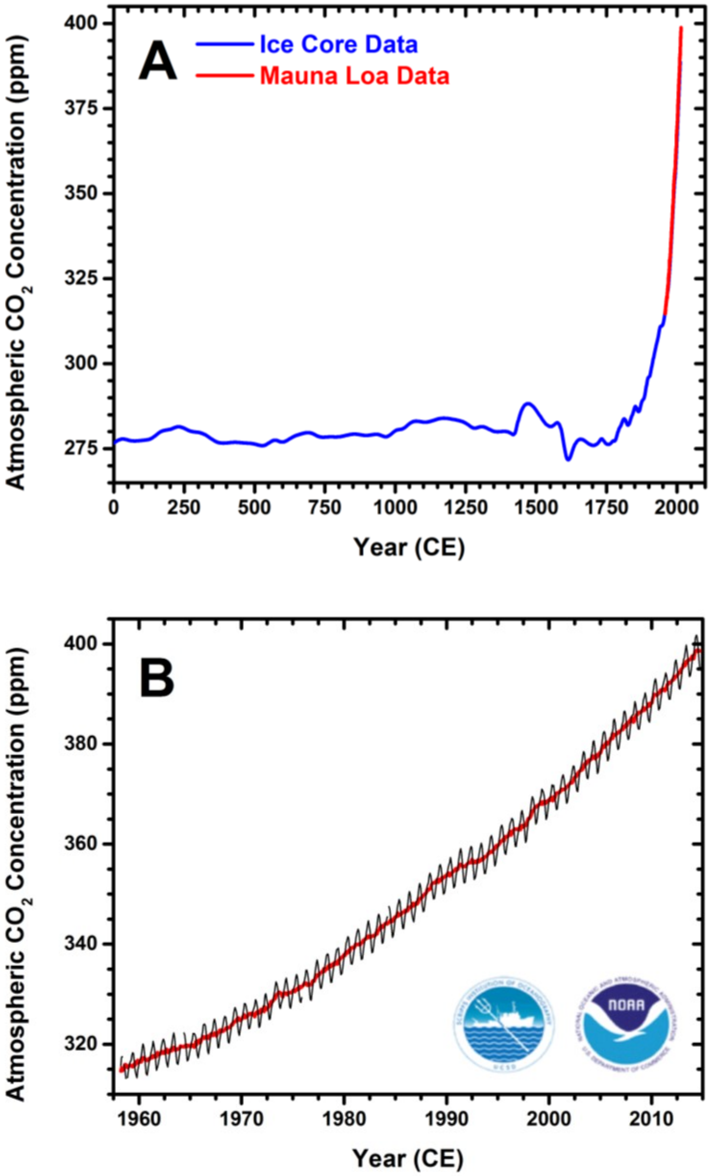

Figure 1.1. Atmospheric carbon dioxide concentration (ppm) as a function of year measured at the Mauna Loa Observatory in Hawaii plotted from year 1 to 2014 (A) and from 1958 to 2014 (B). Prior to 1958, carbon dioxide concentrations were obtained from ice-core data. From 1958 onwards, the atmospheric carbon dioxide concentrations were determined using ice-core data and direct measurements.[12-14]

(a) Observed globally averaged combined land and ocean surface temperature anomaly 1850–2012

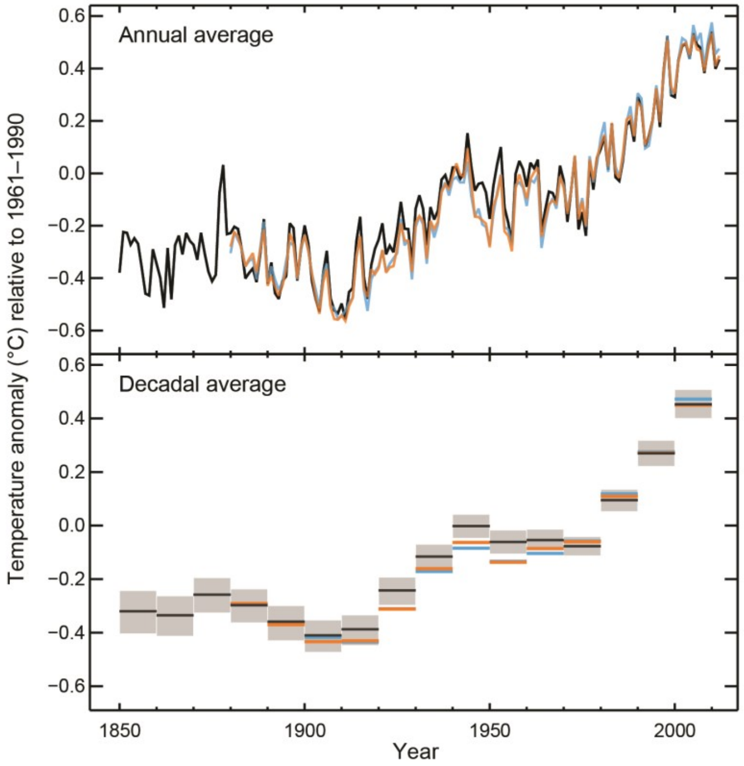

(b) Observed change in surface temperature 1901–2012

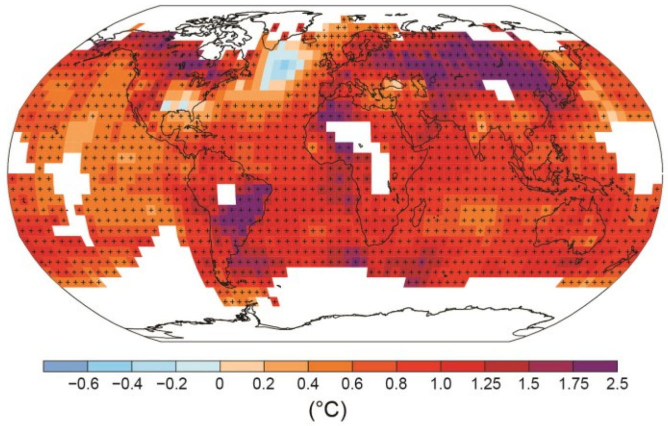

Figure 1.2. (A) Observed annual and decadal global mean surface temperature anomalies from 1850 to 2012 and (B) map of the observed surface temperature change from 1901 to 2012.[16]

1.3 Solar Energy Conversion

1.3.1 Renewable Energy Alternatives

Dependence on fossil fuels for energy production clearly results in detrimental environmental effects, predominantly from carbon dioxide emission, and has prompted interest in alternative energy sources. In order to fulfill the massive global energy demands, a realistic approach would likely implement energy production from a broad portfolio of resources including traditional fossil fuels while expanding the use of renewable alternatives. Biomass, hydroelectric, wind, geothermal, and solar photovoltaics are the primary renewable energy resources currently in the marketplace which produce 10% of U.S. and global energy.[6,17] Each of these technologies come with their own unique set of advantages and potential drawbacks. For example, biomass materials such as wood or corn are considered carbon neutral and cost-effective resources but they require growth periods of months to years and may compete with food production. Hydroelectric and wind power are time-tested technologies that produce large quantities of electricity but are restricted to specific geographic locations and require large structures for effective deployment.

Solar energy is an enticing alternative due to the seemingly limitless amount of available energy. More energy from sunlight reaches the earth's surface in 1.5 hours, 180 PWh, than all of the energy consumed globally in 1 year, 150 PWh in 2010.[1,18] The ability to manufacture various sizes of photovoltaic devices ranging from small, handheld components up to large solar arrays the size of several football fields allows for scalable integration in many areas around the world. The inherent disadvantage of solar energy production is the intermittent nature of solar irradiation resulting from the diurnal cycle of sunlight and the threat of adverse weather conditions. These intermittency issues could be overcome through the conversion and storage of solar energy in chemical bonds, generating so-called solar fuels.[18-21] In this scenario, photovoltaics would generate electricity and produce solar fuels, such as water or methanol, during the day which could then be used during the night or when solar irradiation is impeded. Solar energy conversion is not a new concept for the inorganic chemistry field. The Oil Crises of 1973 and 1979 have spurred many research groups to study the use of inorganic chromophores for electricity generation from sunlight, particularly ruthenium-based compounds.[22-25]

1.3.2 Ruthenium Polypyridyl Compounds

Arguably the most well studied inorganic compound is the ruthenium polypyridyl dication $[\mathrm{Ru^{II}(bpy)_3}]^{2+}$, where bpy is 2,2'-bipyridine, shown in Figure 1.3. Mononuclear Ru(II) compounds have attracted broad interest due to their unique photophysical properties including ease of electronic tunability, redox chemistry, long-lived excited states, excited-state reactivity, photoluminescence, and chemical stability. Exploitation of these beneficial properties has led to the use of Ru(II) compounds in a variety of applications such as photocatalysis in organic synthesis,[26-27] photodynamic therapy,[28-30] optical switching,[31-32] electroluminescent devices,[33-35] and solar energy conversion.[36-38] Most polypyridyl Ru(II) compounds owe their chemical inertness to the pseudo-octahedral geometry, formally D_3 symmetry, and electronic structure of d^6 metal ions in addition to the large ligand-field splitting associated with second row transition metal elements. The commonly used polypyridine ligands bond through σ donor orbitals on the nitrogen atoms and possess π donor and π^* acceptor orbitals that are delocalized over the aromatic rings.

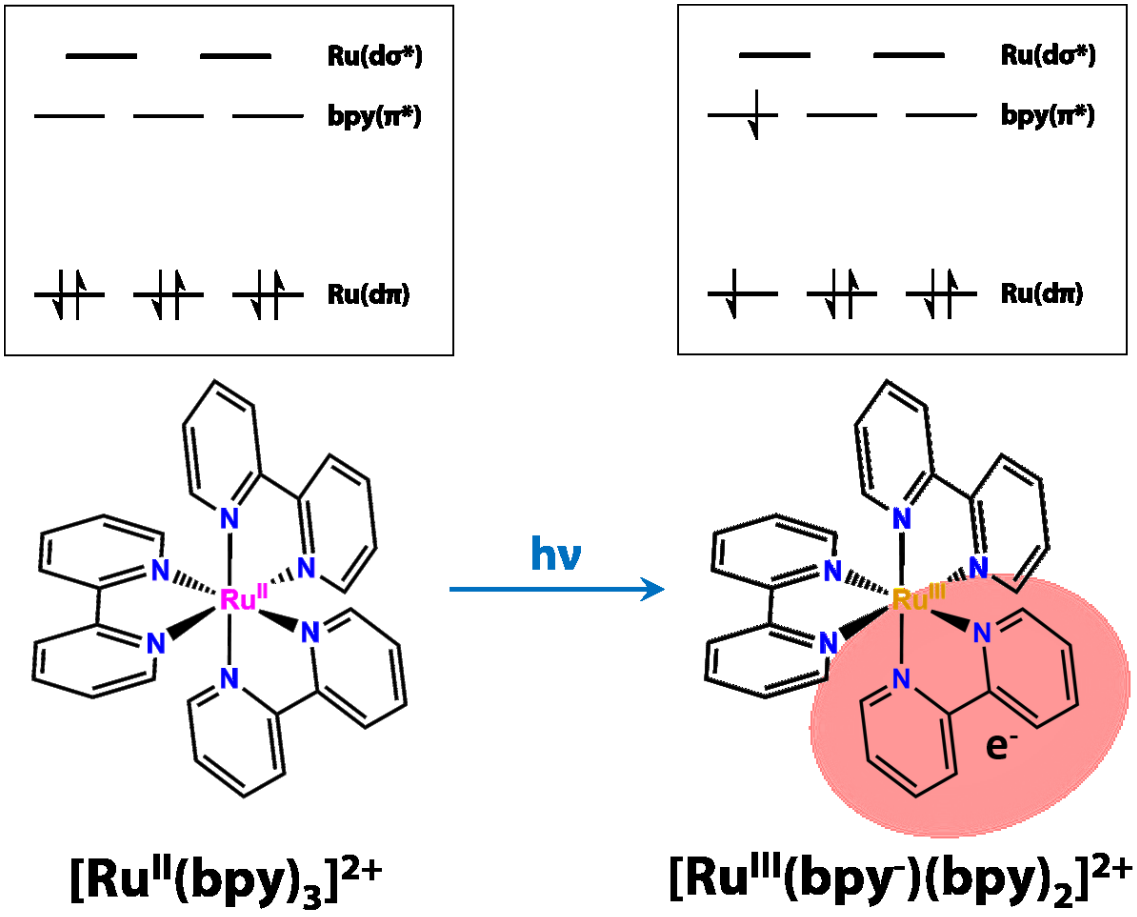

Figure 1.3. Depiction of the electronic state of $[Ru^{II}(bpy)_3]^{2+}$ and of the triplet metal-to-ligand charge transfer (^{3}MLCT) state following light excitation. The red oval indicates electron localization on a single bipyridine ligand in the excited state.

As a result of the large ligand-field splitting of Ru(II) and the energetics of bipyridine, the highest occupied molecular orbital (HOMO) for $[Ru^{II}(bpy)_3]^{2+}$ is predominantly metal in parentage while the lowest occupied molecular orbital (LUMO) is associated with the π^* orbitals of the bipyridine ligand. The energetic splitting between the HOMO and LUMO, or the band-gap energy, determines the lowest energy electronic transition of a compound. Through simple cyclic voltammetry measurements, it is possible to determine the formal reduction potential for the metal center, $E^0(Ru^{III/II})$, as well as those of the ligands, $E^0(L^{0/-})$, which are associated with the HOMO and LUMO energies, respectively. The formal ruthenium reduction potential for $[Ru^{II}(bpy)_3]^{2+}$ in acetonitrile is $E^0(Ru^{III/II}) = +1.25$ V vs. the normal hydrogen electrode (NHE).[20] The first ligand reduction of bipyridine occurs more negative on an electrochemical scale with $E^0(bpy^0/^-) = -1.25$ V vs. NHE.[23,39] Through alteration of the ligand set, the reduction potentials, and consequently the absorption properties, of Ru(II) compounds can be tuned across a wide range of values.

Promotion of an electron from the Ru-based HOMO to the bpy-based LUMO results in a metal-to-ligand charge transfer (MLCT) transition; see Figure 1.3 for an electronic and structural depiction. Other electronic transitions are also possible, including ligand-centered (LC) and ligand field (LF) transitions. While Ru(II) polypyridyl compounds are most famous for their MLCT excited states, the LF excited states are also of interest as they are formally anti-bonding with respect to metal-ligand bonds and are associated with ligand loss photochemistry. This photochemical ligand loss can be beneficial for photodynamic therapy applications, but is detrimental for long-term applications that require chemical integrity such as in electroluminescent or solar energy conversion devices.[40]

The molar absorptivity spectrum of $[Ru^{II}(bpy)_3](PF_6)_2$ is shown in Figure 1.4 as a function of wavelength. The characteristic MLCT absorption band at 450 nm (ε = 14,200 $M^{-1}cm^{-1}$) tails to almost 575 nm. This is consistent with predictions of an electronic transition at 500 nm based on the band-gap energy of 2.50 eV measured electrochemically.[20,23,39] The strong, sharp absorption around 285 nm (ε = 84,400 $M^{-1}cm^{-1}$) is attributed to a bpy-based π-π^* LC transition.[23,41] Excitation into the MLCT or LC absorption band results in room-temperature photoluminescence, which maximizes around 615 nm, see Figure 1.4. The broad, featureless nature of the photoluminescence band coupled with its solvent dependence indicate that the excited state is MLCT in character.

The physical description of the electron in the MLCT excited state was a matter of controversial debate for several decades. The primary question was whether the electron localized on one single bipyridine or delocalized across all three with 1/3 of an electronic charge formally residing on each bipyridine. Solvent dependent absorption data and time-resolved resonance Raman spectroscopy indicated that the localized electron model was most appropriate for tris-heteroleptic ruthenium polypyridyl compounds. Electroabsorption experiments by the groups of Boxer and Hupp further supported the electron localized model through direct measurement of the change in dipole moment between the ground and excited states, $\Delta\mu$.[42-44] The charge transfer distance of the electron was calculated using the experimentally determined $\Delta\mu$ values and found to be less than the theoretical value for full charge transfer (~65% for $[Ru^{II}(bpy)_3]^{2+}$).[43] The discrepancy was attributed to π back bonding in the ground state and movement of electron density towards the formally oxidized ruthenium metal center in the excited state.[45] Subsequent ultrafast transient spectroscopy experiments showed that while the electron localizes on a single ligand, it becomes "randomized" through interligand hopping.[23,41]

Transient experiments have been used to extensively characterize the photophysics and photochemistry of $[Ru^{II}(bpy)_3]^{2+*}$ and are summarized in the Jablonski diagram shown in Figure 1.5. Initial light excitation of the compound generates a Franck-Condon (FC) state, which relaxes in the ^{1}MLCT state manifold and undergoes intersystem crossing to the ^{3}MLCT manifold with a quantum yield of unity on the ~15 - 100 fs timescale.[23,46] Internal conversion to the lowest energetic level of the ^{3}MLCT state occurs within ~20 ps.[23,41,46-47] Although Crosby provided evidence against the validity and appropriateness of using spin as a quantum number for ruthenium compounds due to the relatively large spin-orbit coupling constant of Ru (ζ = 900 - 1000 cm^{-1}), spin multiplicity is still commonly referred to for convenience.[48-50] Following Kasha's rule, the lowest energetic excited state of ruthenium polypyridyl compounds, the ^{3}MLCT state, is the emissive state.[51] Photoluminescence of $[Ru^{II}(bpy)_3]^{2+}$ is characterized by a quantum yield (Φ_{PL}) of 0.062 with a lifetime (τ) of 825 ns in fluid acetonitrile solution.[52-53] Using Φ_{PL} and τ, the radiative (k_r) and non-radiative (k_{nr}) decay constants can be calculated using Equation (1.1) and (1.2), respectively:

$$k_r = \frac{\Phi_{PL}}{\tau} \tag{1.1}$$

$$k_{nr} = \frac{1}{\tau} - k_r \tag{1.2}$$

yielding $k_r = 7.5 \times 10^4$ s^{-1} and $k_{nr} = 1.1 \times 10^6$ s^{-1}.[53]

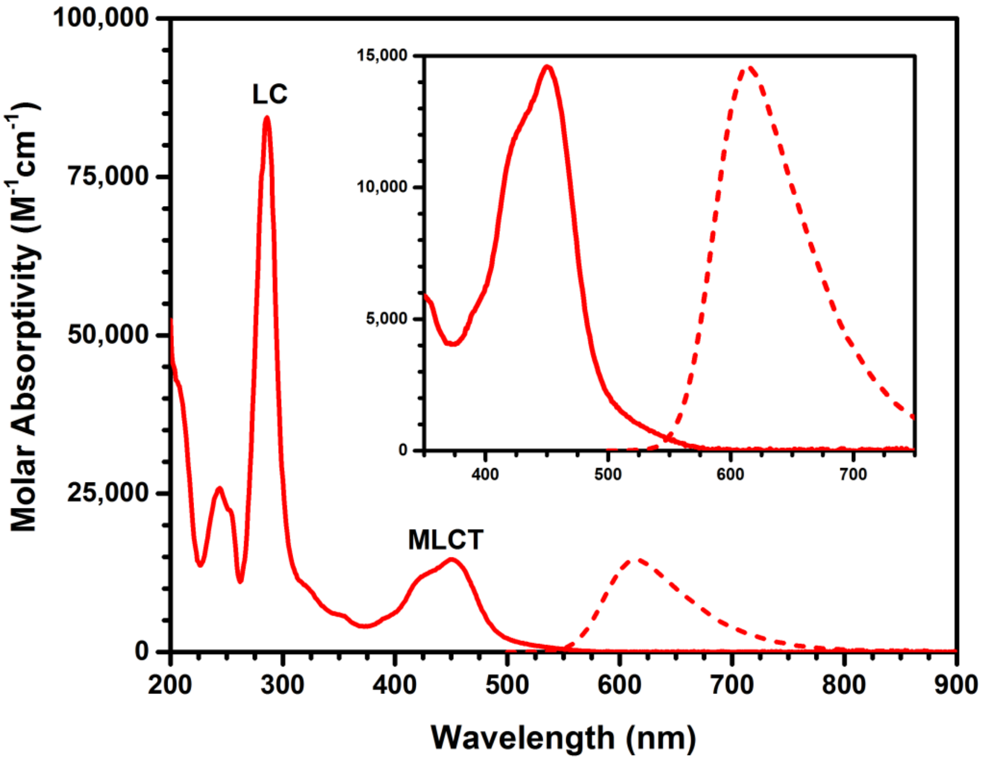

Figure 1.4. UV-vis absorption (solid line) and photoluminescence (dashed line) of $[Ru^{II}(bpy)_3](PF_6)_2$ in acetonitrile solution. The absorption spectrum is given as molar absorptivity while the photoluminescence spectrum has been arbitrarily normalized to the maximum of the MLCT absorption band.

Temperature-dependent, time-resolved photoluminescence studies on ruthenium polypyridyl and other related d^3 and d^6 compounds have provided further insight into their excited state relaxation pathways through Arrhenius analyses. Hager and Crosby determined that the ^{3}MLCT state of $[\mathrm{Ru^{II}(bpy)_3}]^{2+}$ is actually comprised of three distinct states separated by 10 and 60 $\mathrm{cm^{-1}}$ in energy.[54] These three states behave as a single entity above 30 K and are termed a thermally equilibrated excited state (thexi).[55] Related measurements near room temperature found evidence for thermal activation from the thexi state to LF states. Activation energies were greater than 2,800 $\mathrm{cm^{-1}}$ and typically accompanied by photochemical ligand loss.[56] Ruthenium compounds with strong field ligands, such as cyanide, or physically constricted samples, such as $[\mathrm{Ru^{II}(bpy)_3}]^{2+}$ encapsulated in zeolites, did not undergo ligand loss photochemistry but rather the excited state lifetimes displayed a weak temperature dependence.[57-59] This weak temperature dependence was characterized by activation energies ranging from 300 to 1,000 $\mathrm{cm^{-1}}$ and attributed to thermal population of a fourth MLCT state based on theoretical studies, comparison to $[\mathrm{Os^{II}(bpy)_3}]^{2+}$, and spectral modeling of photoluminescence spectra.[60-62] The excited state relaxation pathways for ruthenium polypyridyl compounds containing formally weak-field isothiocyanate ligands are discussed in Chapter 2 for compounds in fluid solution and attached to metal oxide thin films. The spectral tunability, excited state lifetimes, and photostability outlined above make ruthenium polypyridyl compounds useful candidates for solar energy conversion. However, in order to effectively generate electricity the compounds must be physically integrated into functional devices.

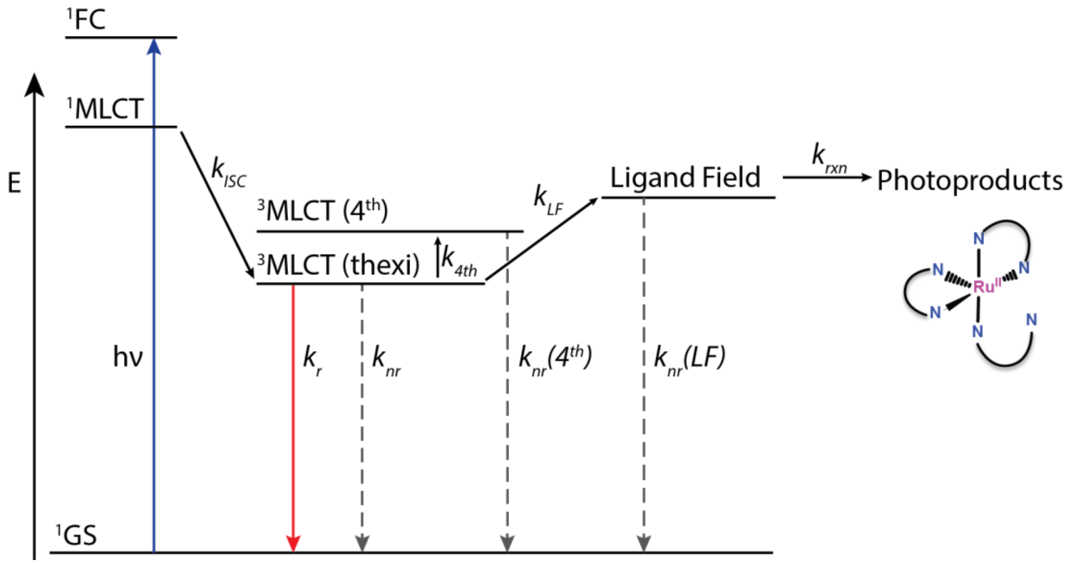

Figure 1.5. Jablonski diagram of $[\mathrm{Ru^{II}(bpy)_3}]^{2+}$ where solid lines indicate radiative transitions and dashed lines indicate non-radiative transitions. The structure to the right indicates a photochemical ligand loss product generated through the ligand field state.

1.3.3 Dye-Sensitized Solar Cells (DSSCs)

The first solar cells to gain prominence were inorganic, crystalline silicon photovoltaics. Silicon-based devices saw continual improvement from the initial report of 1% efficiency in 1941 up to 25% in 2009.[63-64] The energy separation between the valence band (E_{VB}) and conduction band (E_{CB}) edges, i.e. the band gap, of (poly)crystalline silicon materials is 1.1 eV, thus enabling the generation of electricity from absorbed photons with wavelengths less than 1,130 nm. Unfortunately, photons containing energy greater than the minimum amount required for band gap excitation undergo thermal losses by activating phonon modes of the semiconductor. In order to generate larger photovoltages, and hence increase the amount of available energy, wide band-gap semiconductors could be used such as crystalline anatase titanium dioxide. The band gap of anatase titanium dioxide, 3.2 eV, is greater than that of silicon, but has limited efficacy as a photovoltaic material because it only absorbs 3% of the photons in the solar spectrum, which limits its efficacy as a photovoltaic material.[65-67] A larger spectral range of solar radiation could be harvested using ruthenium polypyridyl compounds due to their tunable absorption bands in the visible region.

Early work in the 1970s utilized monolayers of dye molecules on planar semiconductor substrates in order to sensitize the semiconductor to visible light.[67-69] Using this approach, photon absorption promotes a sensitizer to an excited state that can then transfer an electron to the semiconductor, a process termed electron injection. In this manner, the spectral properties of the sensitizer could be tuned independently of the semiconductor for broader harvesting of the solar spectrum. Experimental and theoretical efforts by Heinz Gerischer provided a framework to understand electron injection efficiency by describing the interaction of donor states of the excited dye molecule with the acceptor states of the semiconductor.[70-71]

The use of planar, semiconductor substrates and monolayer sensitizer surface coverage (Figure 1.6) meant that only a small portion of the incident light was absorbed by the sensitizers, less than 3%, resulting in low efficiencies around 0.1 – 0.5%.[66,68] Initial attempts to increase efficiency focused on increasing light absorption through the deposition of multiple sensitizer layers on the substrate. Although these thick films did absorb more light than their monolayer counterparts, they produced very low incident photon to current efficiencies (IPCE), less than 0.05%, due to small exciton diffusion lengths.[72]

In 1991, the work of O'Regan and Grätzel introduced a paradigm shift that advanced dye-sensitized solar cells (DSSCs) from the realm of the purely academic to the practical.[73] They pioneered the use of mesoporous, nanocrystalline anatase titanium dioxide thin films which afforded surface areas three orders of magnitude greater than those for planar substrates. These mesoscopic thin films, 5 – 10 μm thick, could absorb greater than 99% of the incident light with monolayer surface coverage of the sensitizer while maintaining quantitative electron collection efficiencies due to the proximity of each sensitizer to the semiconductor.[73] The structural evolution of the sensitizer-semiconductor strategy is depicted in Figure 1.6. Using the trinuclear compound $[Ru(bpy)_2(\mu\text{-}CN)_2]_2Ru(dcbH_2)_2$, where $dcbH_2$ is 2,2'-bipyridine-4,4'-dicarboxylic acid, as a sensitizer and the iodide/triiodide redox mediator in acetonitrile, O'Regan and Grätzel obtained unprecedented efficiencies of 7 – 8%.[73] The structure of the trinuclear compound is shown in Figure 1.7 alongside other champion ruthenium sensitizers, which are listed with their efficiencies reported at the time of initial publication.[73-76]

The working principle of DSSCs was established from the theories developed by Gerischer for planar electrodes and is shown schematically in Figure 1.8. In DSSCs, dye molecules, often called sensitizers, S, are attached to a wide band gap semiconductor using carboxylic acid linkages. In an operational DSSC, absorption of a photon of light promotes an electron to an excited state of the dye molecule. Subsequent excited state electron injection into the titanium dioxide acceptor states occurs on the ultrafast, fs – ps, timescale.[77-79] The injected electron emanates an interfacial electric field that perturbs the electronic states of surface-bound dye molecules.[65,80] After photoinjection, the electron thermally relaxes to the quasi-Fermi level of the semiconductor and can diffuse through the mesoporous network to the transparent conductive oxide electrode, TCO. The electron then travels through a circuit to perform useful work in the external circuit. Meanwhile, the oxidized sensitizer is regenerated by an electron donor present in the external electrolyte solution, typically iodide. The oxidized iodide product, tri-iodide, traverses out of the mesopores of the thin film and through the bulk electrolyte to a dark counter electrode, typically platinized TCO, where it is reduced back to iodide and completes the circuit. The mixture of reduced and oxidized donors, $D^{+/0}$, are often called redox mediators as they mediate electron transfer between the two electrodes.[65-66,79,81] In this way, no net photochemistry occurs and DSSCs are considered regenerative solar cells that convert photonic energy into electricity.

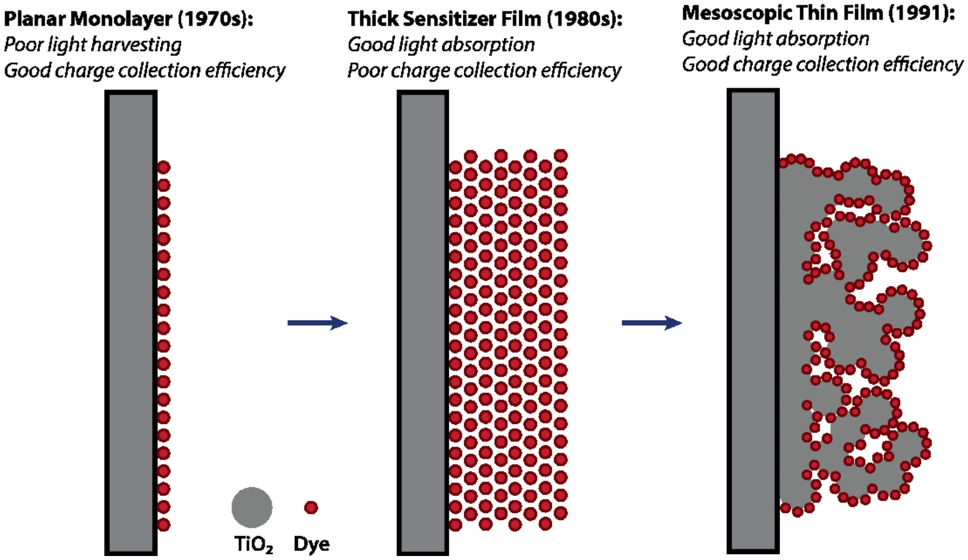

Figure 1.6. Cartoon evolution of the sensitized semiconductor approach to solar energy conversion. The black rectangles indicate planar semiconductor or transparent conductive oxide substrates.

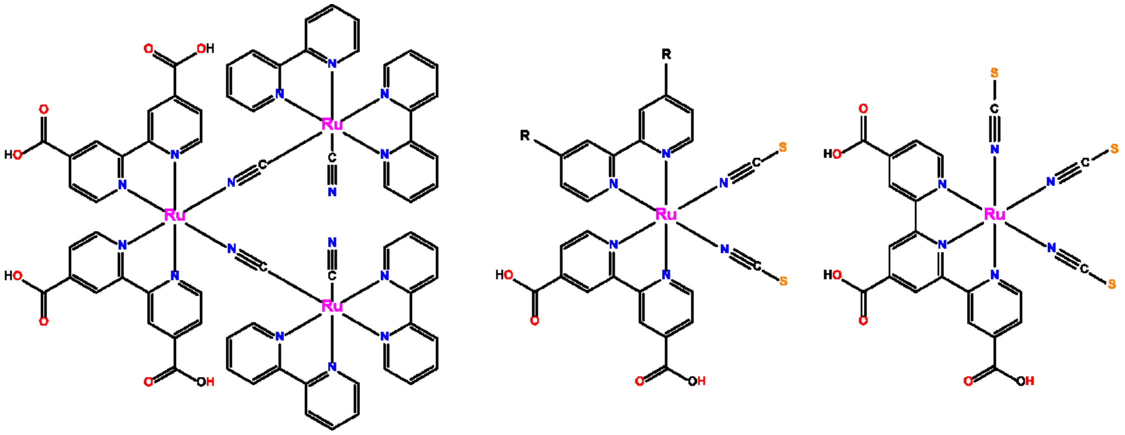

$[Ru(bpy)_2(\mu\text{-}CN)_2]_2Ru(dcbH_2)_2$
7 - 8%

***cis*-$[Ru(dcbH_2)(LL)(NCS)_2]$**
"N3" R = -COOH 10%
"Z907" R = *n*-nonyl 6.1%

$[Ru(tctpyH_3)(NCS)_3]$
"black dye"
10.4%

Figure 1.7. Structures of champion ruthenium polypyridyl sensitizers listed with the common codifications and the overall DSSC efficiencies reported when first published.

Some of the potential loss mechanisms for DSSC efficiency are indicated by the dashed red arrows in Figure 1.8 and include: excited state decay, through both radiative and non-radiative pathways; charge recombination from injected electrons to oxidized sensitizers; and charge recombination from injected electrons to the oxidized iodide species.

1.3.4 Recent Developments

Efforts to improve the efficiency and practicality of DSSCs over the past 23 years have primarily focused on sensitizer development, inhibition of charge recombination, development of alternative redox mediators, and modification of electrolyte composition.[65,79,82] Two major concerns for sensitizers are their absorption characteristics and photostability.[79,83] Ruthenium sensitizers are remarkably stable, capable of undergoing greater than 10^6 turnovers in an operational DSSC.[73] However, some researchers have expressed concerns about the stability of compounds containing isothiocyanate ligands and have turned to new ligand motifs, such as cyclometalating ligands.[84-86] The issue of sensitizer stability is addressed in Chapter 2 through temperature-dependent, time-resolved photoluminescence experiments. Another sensitizer design requirement is a method of attachment to the titanium dioxide surface with carboxylic acids being the most widely used functional groups. The ground and excited-state acid behavior of two ruthenium polypyridyl compounds containing carboxylic acids is described in Chapter 5.

Successful strategies for the inhibition of charge recombination include movement of charge away from the interface through sensitizer design and surface modification of the titanium dioxide nanocrystallites Sensitizers capable of moving the oxidizing equivalent away from the titanium dioxide surface, either through intramolecular hole transfer or

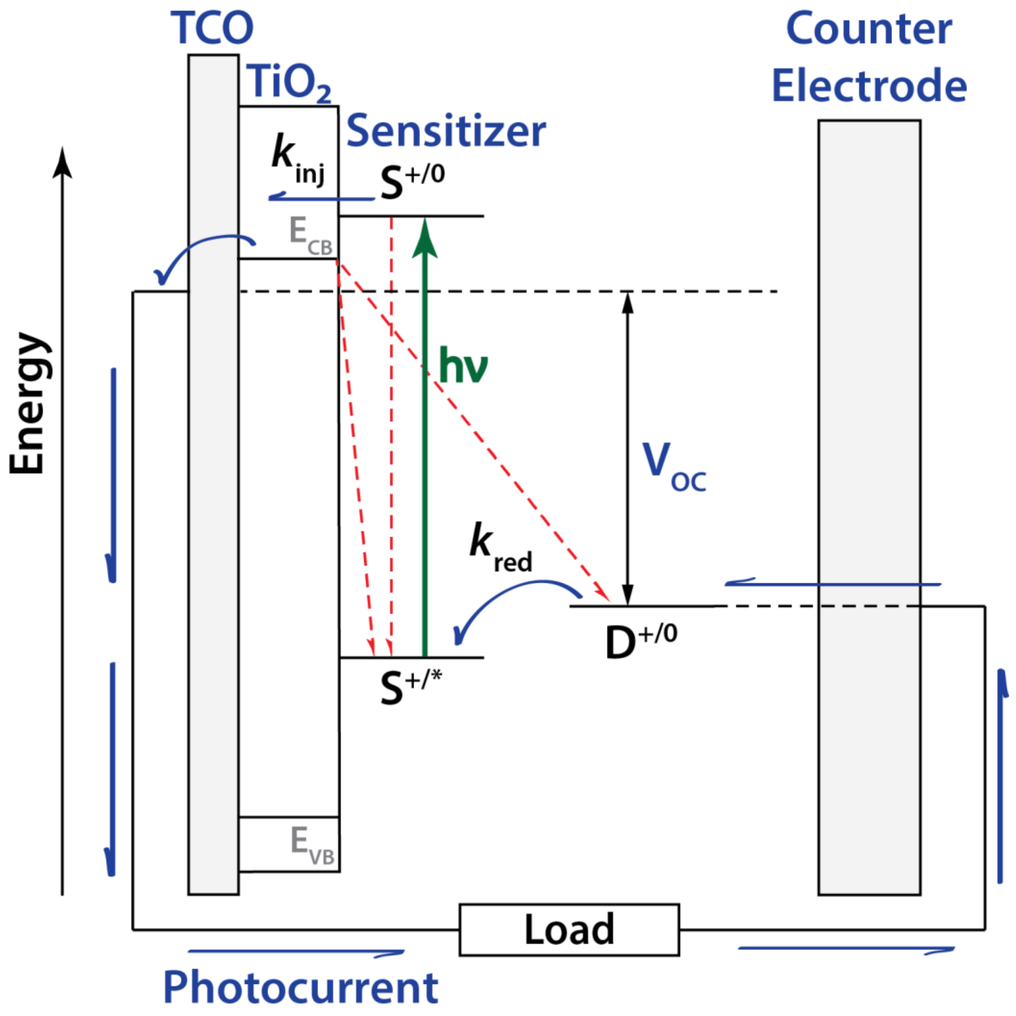

Figure 1.8. Schematic of a dye-sensitized solar cell (DSSC). The green arrow indicates light absorption processes. Solid, blue arrows indicate beneficial electron flow for generation of photocurrent. Dashed, red arrows indicate processes detrimental to efficiency: 1) photoluminescence; and 2) charge recombination from $TiO_2(e^-)$s either to the oxidized sensitizer, S^+, or the redox mediator, D^+, in solution. See text for a detailed description.

variable length ligand spacers, resulted in decreased rates of charge recombination compared to reference compounds.[87-88] The use of atomic layer deposition to coat titanium dioxide nanocrystallites with titania and alumina blocking layers or the use of core-shell nanoparticle architectures have resulted in increased efficiencies and sensitizer stability by hindering charge recombination processes.[89-92] Charge recombination to tri-iodide is studied in Chapter 4 and was found to be affected by electric fields present at the TiO_2-sensitizer interface.

Research programs devoted to improving DSSC efficiency and stability through the use of alternative redox mediators and electrolyte composition have seen some success. Replacement of the corrosive iodide/triiodide redox mediator has been particularly effective with the use of cobalt(III/II) polypyridine compounds and has led to improved open circuit photovoltages.[93-95] Efforts to eliminate volatile solvents altogether through development of solid-state DSSCs (ss-DSSCs) have seen marked improvement through the inclusion of 9,9'-spirobifluorene, spiro-MeOTAD, as a hole transport material.[79,96] Recent evidence suggests that the interfacial electric fields generated by injected electrons in titanium dioxide nanocrystallites can affect open circuit photovoltages and also complicate interpretation of spectroscopic data in traditional and solid-state DSSCs.[80,97-98] Chapters 3 and 4 present experiments that characterize these interfacial electric fields and examine the influence of electrolyte composition on these fields.

Although efficiencies remain below 15% and have not approached those of conventional silicon photovoltaics, DSSCs are finding niche applications and their future is bright. The current, confirmed record efficiency for a DSSC is 11.9% for a cell fabricated by the Sharp® corporation.[99] In 2010, Logitech® commercially launched a line of wireless solar keyboards which use DSSC technology and can retain a charge for three months in the dark.[100-101] Construction of the Swiss Tech Convention Center at the École Polytechnique Fédérale de Lausanne (EPFL) in Lausanne, Switzerland demonstrated the first instance of architectural integration of translucent DSSCs. The electricity production from 300 m^2 of these “stained glass solar cell windows” is estimated at 8 MWh annually.[102] While these efforts provide only a fraction of the electricity demands for consumers, the unobtrusive integration of DSSCs into previously existing technologies indicates the promise of DSSCs for solar energy conversion.

1.4 Summary

A global demand and environmental imperative exists for renewable, sustainable energy. Sunlight is an obvious alternative energy choice due to the massive amount of energy delivered to the earth’s surface in the form of photons. This thesis describes fundamental photophysical and photochemical studies of ruthenium polypyridyl compounds, particularly of their MLCT excited states, that have solidified their position as prime candidates for solar energy conversion. Implementation of ruthenium compounds as solar absorbers attached to mesoscopic thin films of titanium dioxide in DSSCs led to a modular paradigm in photovoltaics by decoupling the light harvesting and charge collection processes. Efficiencies exceeding 10% have been confirmed for operational devices. In addition to their practical applications, fundamental studies of DSSCs have furthered our understanding of concepts with broad chemical relevance and specific examples related to excited state photophysics (Chapters 2 and 5) and interfacial electric fields (Chapters 3 and 4) are presented in this thesis.

1.5 References

(1) U.S. Energy Information Administration, "International Energy Statistics: Total Primary Energy Consumption (Quadrillion Btu)", 2013. International Energy Statistics, http://www.eia.gov/cfapps/ipdbproject/IEDIndex3.cfm?tid=44&pid=44&aid=2 (accessed 10/14/2014).

(2) U.S. Energy Information Administration, "Annual Energy Outlook 2013: World Total Primary Energy Consumption by Region, Reference Case (Quadrillion Btu)", 2013. International Energy Statistics, http://www.eia.gov/oiaf/aeo/tablebrowser/#release=IEO2013&subject=0-IEO2013&table=1-IEO2013&region=0-0&cases=Reference-d041117 (accessed 10/14/2014).

(3) U.S. Energy Information Administration, "International Energy Statistics: Total Electricity Net Consumption (Billion Kilowatthours)", 2013. International Energy Statistics, http://www.eia.gov/cfapps/ipdbproject/IEDIndex3.cfm?tid=2&pid=2&aid=2 (accessed 10/14/2014).

(4) U.S. Census Bureau, "Demographic Overview - Custom Region - United States", 2013. U.S. Census Bureau, International Data Base, http://www.census.gov/population/international/data/idb/region.php?N=%20Results%20&T=13&A=separate&RT=0&Y=2010&R=-1&C=US (accessed 10/14/2014).

(5) U.S. Census Bureau, "Total Midyear Population for the World: 1950 - 2050", 2013. U.S. Census Bureau, International Data Base, http://www.census.gov/population/international/data/worldpop/table_population.php (accessed 10/14/2014).

(6) U.S. Energy Information Administration. "Monthly Energy Review: Table 2.1 Energy Consumption by Sector (Trillion Btu)". http://www.eia.gov/totalenergy/data/monthly/pdf/sec2_3.pdf (accessed 10/14/2014).

(7) Cisco Public. "The Zettabyte Era: Trends and Analysis", 2014. Cisco, White Paper, http://www.cisco.com/c/en/us/solutions/collateral/service-provider/visual-networking-index-vni/VNI_Hyperconnectivity_WP.pdf (accessed 10/14/2014).

(8) Evans, D. "The Internet of Things", 2011. Cisco, White Paper, http://www.cisco.com/web/about/ac79/docs/innov/IoT_IBSG_0411FINAL.pdf (accessed 10/14/2014).

(9) U.S. Energy Information Administration. "How much carbon dioxide is produced by burning gasoline and diesel fuel?". http://www.eia.gov/tools/faqs/faq.cfm?id=307&t=11 (accessed 10/14/2014).

(10) U.S. Energy Information Administration. "How much electricity does an American home use?". http://www.eia.gov/tools/faqs/faq.cfm?id=97&t=3 (accessed 10/14/2014).

(11) National Research Council. *Climate Change: Evidence, Impacts, and Choices;* Huddleston, N., Eds.; National Academy of Science: Washington, DC, USA, 2012; pp 1-40.

(12) Etheridge, D. M.; et al. *Law Dome Ice Core 2000-Year* CO_2*,* CH_4*, and* N_2O *Data*; World Data Center for Paleoclimatology Boulder and NOAA Paleoclimatology Program: Boulder, CO, USA, ftp://ftp.ncdc.noaa.gov/pub/data/paleo/icecore/antarctica/law/law2006.txt (accessed 10/15/2014).

(13) Keeling, R. F.; Piper, S. C.; Bollenbacher, A. F.; Walker, S. J. *Merged Ice-Core Record - Spline*; Scripps CO_2 Program: La Jolla, CA, USA, http://scrippsco2.ucsd.edu/data/merged_ice_core/spline_merged_ice_core_yearly.csv (accessed 10/15/2014).

(14) Tans, P.; Keeling, R. F. *Mauna Loa CO_2 Monthly Mean Data*; NOAA Earth System Research Laboratory and Scripps Institute of Oceanography: Boulder, CO, USA, ftp://aftp.cmdl.noaa.gov/products/trends/co2/co2_mm_mlo.txt (accessed 10/15/2014).

(15) Luthi, D.; Le Floch, M.; Bereiter, B.; Blunier, T.; Barnola, J.-M.; Siegenthaler, U.; Raynaud, D.; Jouzel, J.; Fischer, H.; Kawamura, K.; Stocker, T. F. *Nature* **2008,** *453*, 379-382.

(16) Intergovernmental Panel on Climate Change. *Climate Change 2013: The Physical Science Basis. Contribution of Working Group I to the Fifth Assessment Report of the Intergovernmental Panel on Climate Change;* Stocker, T. F.; Qin, D.; Plattner, G.-K.; Tignor, M.; Allen, S. K.; Boschung, J.; Nauels, A.; Xia, Y.; Bex, V.; Midgley, P. M., Eds.; Cambridge University Press: New York, NY, USA, 2013; pp 1-1535.

(17) U.S. Energy Information Administration. "Monthly Energy Review: Table 10.1 Renewable Energy Production and Consumption by Source (Trillion Btu)". http://www.eia.gov/totalenergy/data/monthly/pdf/sec10_3.pdf (accessed 10/14/2014).

(18) Lewis, N. S.; Nocera, D. G. *Proc. Natl. Acad. Sci. U. S. A.* **2006,** *103*, 15729-15735.

(19) Gray, H. B. *Nat. Chem.* **2009,** *1*, 7-7.

(20) Song, W.; Chen, Z.; Brennaman, M. K.; Concepcion Javier, J.; Patrocinio Antonio Otávio, T.; Murakami Iha Neyde, Y.; Meyer Thomas, J. *pac* **2011,** *83*, 749.

(21) Song, W.; Chen, Z.; Glasson, C. R. K.; Hanson, K.; Luo, H.; Norris, M. R.; Ashford, D. L.; Concepcion, J. J.; Brennaman, M. K.; Meyer, T. J. *ChemPhysChem* **2012,** *13*, 2882-2890.

(22) Armaroli, N.; Balzani, V., Solar Fuels. In *Energy for a Sustainable World*, Wiley-VCH Verlag GmbH & Co. KGaA: 2010; pp 203-229.

(23) Campagna, S.; Puntoriero, F.; Nastasi, F.; Bergamini, G.; Balzani, V., Photochemistry and Photophysics of Coordination Compounds: Ruthenium. In *Photochemistry and Photophysics of Coordination Compounds I*, Balzani, V.; Campagna, S., Eds. Springer Berlin Heidelberg: 2007; Vol. 280, pp 117-214.

(24) Vos, J. G.; Kelly, J. M. *Dalton Trans.* **2006**, 4869-4883.

(25) Hagfeldt, A.; Boschloo, G.; Sun, L.; Kloo, L.; Pettersson, H. *Chemical Reviews* **2010,** *110*, 6595-6663.

(26) Tucker, J. W.; Stephenson, C. R. J. *J. Org. Chem.* **2012,** *77*, 1617-1622.

(27) Schultz, D. M.; Yoon, T. P. *Science* **2014,** *343*.

(28) Knoll, J. D.; Turro, C. *Coord. Chem. Rev.* **2014,** *In Press*.

(29) Smith, G. S.; Therrien, B. *Dalton Trans.* **2011,** *40*, 10793-10800.

(30) Smith, N. A.; Sadler, P. J. *Philos. Trans. R. Soc. London, Ser. A* **2013,** *371*.

(31) Jin, Y.; Rack, J. J. *Isr. J. Chem.* **2013,** *53*, 280-287.

(32) Rack, J. J. *Coord. Chem. Rev.* **2009,** *253*, 78-85.

(33) Wei, H.; Wang, E. *TrAC, Trends Anal. Chem.* **2008,** *27*, 447-459.

(34) Bernhard, S.; Barron, J. A.; Houston, P. L.; Abruña, H. D.; Ruglovksy, J. L.; Gao, X.; Malliaras, G. G. *J. Am. Chem. Soc.* **2002,** *124*, 13624-13628.

(35) Slinker, J. D.; Rivnay, J.; Moskowitz, J. S.; Parker, J. B.; Bernhard, S.; Abruna, H. D.; Malliaras, G. G. *J. Mater. Chem* **2007,** *17*, 2976-2988.

(36) Licheng, S.; Björn, Å.; Leif, H.; Stenbjörn, S., Toward Solar Energy Conversion into Fuels: Design and Synthesis of Ruthenium-Manganese Supramolecular Complexes to Mimic the Function of Photosystem II. In *Utilization of Greenhouse Gases*, American Chemical Society: 2003; Vol. 852, pp 219-244.

(37) Meyer, G. J. *Inorg. Chem.* **2005,** *44*, 6852-6864.

(38) Concepcion, J. J.; Jurss, J. W.; Brennaman, M. K.; Hoertz, P. G.; Patrocinio, A. O. T.; Murakami Iha, N. Y.; Templeton, J. L.; Meyer, T. J. *Acc. Chem. Res.* **2009,** *42*, 1954-1965.

(39) Juris, A.; Balzani, V.; Barigelletti, F.; Campagna, S.; Belser, P.; von Zelewsky, A. *Coord. Chem. Rev.* **1988,** *84*, 85-277.

(40) Wagenknecht, P. S.; Ford, P. C. *Coord. Chem. Rev.* **2011,** *255*, 591-616.

(41) Thompson David, W.; Ito, A.; Meyer Thomas, J. *Pure Appl. Chem.* **2013,** *85*, 1257.

(42) Boxer, S. G. *J. Phys. Chem. B* **2009,** *113*, 2972-2983.

(43) Oh, D. H.; Boxer, S. G. *J. Am. Chem. Soc.* **1989,** *111*, 1130-1131.

(44) Vance, F. W.; Williams, R. D.; Hupp, J. T. *Int. Rev. Phys. Chem.* **1998,** *17*, 307-329.

(45) Brunschwig, B. S.; Creutz, C.; Sutin, N. *Coord. Chem. Rev.* **1998,** *177*, 61-79.

(46) McCusker, J. K. *Acc. Chem. Res.* **2003,** *36*, 876-887.

(47) Demas, J. N.; Taylor, D. G. *Inorg. Chem.* **1979,** *18*, 3177-3179.

(48) Crosby, G. A.; Hipps, K. W.; Elfring, W. H. *J. Am. Chem. Soc.* **1974,** *96*, 629-630.

(49) Demas, J. N.; Crosby, G. A. *J. Mol. Spectrosc.* **1968,** *26*, 72-77.

(50) Flamigni, L.; Barbieri, A.; Sabatini, C.; Ventura, B.; Barigelletti, F., Photochemistry and Photophysics of Coordination Compounds: Iridium. In *Photochemistry and Photophysics of Coordination Compounds II*, Balzani, V.; Campagna, S., Eds. Springer Berlin Heidelberg: 2007; Vol. 281, pp 143-203.

(51) Kasha, M. *Faraday Discuss.* **1950,** *9*, 14-19.

(52) Caspar, J. V.; Meyer, T. J. *Inorg. Chem.* **1983,** *22*, 2444-2453.

(53) O'Donnell, R. M.; Johansson, P. G.; Abrahamsson, M.; Meyer, G. J. *Inorg. Chem.* **2013,** *52*, 6839-6848.

(54) Hager, G. D.; Crosby, G. A. *Journal of the American Chemical Society* **1975,** *97*, 7031-7037.

(55) Adamson, A. W. *J. Chem. Educ.* **1983,** *60*, 797.

(56) Forster, L. S. *Coord. Chem. Rev.* **2002,** *227*, 59-92.

(57) Juris, A.; Barigelletti, F.; Balzani, V.; Belser, P.; von Zelewsky, A. *J. Chem. Soc., Faraday Trans.* **1987,** *83*, 2295-2306.

(58) Maruszewski, K.; Kincaid, J. R. *Inorg. Chem.* **1995,** *34*, 2002-2006.

(59) Maruszewski, K.; Strommen, D. P.; Kincaid, J. R. *J. Am. Chem. Soc.* **1993,** *115*, 8345-8350.

(60) Lumpkin, R. S.; Kober, E. M.; Worl, L. A.; Murtaza, Z.; Meyer, T. J. *J. Phys. Chem.* **1990,** *94*, 239-243.

(61) Sykora, M.; Kincaid, J. R. *Inorg. Chem.* **1995,** *34*, 5852-5856.

(62) Harriman, A.; Izzet, G. *Phys. Chem. Chem. Phys.* **2007,** *9*, 944-948.

(63) Wenham, S. R.; Green, M. A. *Progress in Photovoltaics: Research and Applications* **1996,** *4*, 3-33.

(64) Green, M. A. *Progress in Photovoltaics: Research and Applications* **2009,** *17*, 183-189.

(65) Ardo, S.; Meyer, G. J. *Chem. Soc. Rev.* **2009,** *38*, 115-164.

(66) Meyer, G. J. *ACS Nano* **2010,** *4*, 4337-4343.

(67) Gleria, M.; Memming, R. *zpch* **1975,** *98*, 303.

(68) Spitler, M. T.; Calvin, M. *J. Chem. Phys.* **1977,** *66*, 4294-4305.

(69) Anderson, S.; Constable, E. C.; Dare-Edwards, M. P.; Goodenough, J. B.; Hamnett, A.; Seddon, K. R.; Wright, R. D. *Nature* **1979,** *280*, 571-573.

(70) Gerischer, H. *Photochem. Photobiol.* **1972,** *16*, 243-260.

(71) Gerischer, H.; Michel-Beyerle, M. E.; Rebentrost, F.; Tributsch, H. *Electrochim. Acta* **1968,** *13*, 1509-1515.

(72) Jaeger, C. D.; Fan, F.-R. F.; Bard, A. J. *J. Am. Chem. Soc.* **1980,** *102*, 2592-2598.

(73) O'Regan, B.; Grätzel, M. *Nature* **1991,** *353*, 737-740.

(74) Nazeeruddin, M. K.; Kay, A.; Rodicio, I.; Humphry-Baker, R.; Mueller, E.; Liska, P.; Vlachopoulos, N.; Grätzel, M. *J. Am. Chem. Soc.* **1993,** *115*, 6382-6390.

(75) Wang, P.; Zakeeruddin, S. M.; Moser, J. E.; Nazeeruddin, M. K.; Sekiguchi, T.; Grätzel, M. *Nat. Mater.* **2003,** *2*, 402-407.

(76) Péchy, P.; Renouard, T.; Zakeeruddin, S. M.; Humphry-Baker, R.; Comte, P.; Liska, P.; Cevey, L.; Costa, E.; Shklover, V.; Spiccia, L.; Deacon, G. B.; Bignozzi, C. A.; Grätzel, M. *J. Am. Chem. Soc.* **2001,** *123*, 1613-1624.

(77) Kallioinen, J.; Benkö, G.; Myllyperkiö, P.; Khriachtchev, L.; Skårman, B.; Wallenberg, R.; Tuomikoski, M.; Korppi-Tommola, J.; Sundström, V.; Yartsev, A. P. *J. Phys. Chem. B* **2004,** *108*, 6365-6373.

(78) Asbury, J. B.; Anderson, N. A.; Hao, E.; Ai, X.; Lian, T. *J. Phys. Chem. B* **2003,** *107*, 7376-7386.

(79) Hagfeldt, A.; Boschloo, G.; Sun, L.; Kloo, L.; Pettersson, H. *Chem. Rev.* **2010,** *110*, 6595-6663.

(80) Ardo, S.; Sun, Y.; Staniszewski, A.; Castellano, F. N.; Meyer, G. J. *J. Am. Chem. Soc.* **2010,** *132*, 6696-6709.

(81) Grätzel, M. *Inorg. Chem.* **2005,** *44*, 6841-6851.

(82) Grätzel, M. *Acc. Chem. Res.* **2009,** *42*, 1788-1798.

(83) Asghar, M. I.; Miettunen, K.; Halme, J.; Vahermaa, P.; Toivola, M.; Aitola, K.; Lund, P. *Energy Environ. Sci.* **2010,** *3*, 418-426.

(84) Nguyen, H. T.; Ta, H. M.; Lund, T. *Sol. Energy Mater. and Sol. Cells* **2007,** *91*, 1934-1942.

(85) Nour-Mohhamadi, F.; Nguyen, S. D.; Boschloo, G.; Hagfeldt, A.; Lund, T. *J. Phys. Chem. B* **2005,** *109*, 22413-22419.

(86) Bomben, P. G.; Robson, K. C. D.; Koivisto, B. D.; Berlinguette, C. P. *Coord. Chem. Rev.* **2012,** *256*, 1438-1450.

(87) Argazzi, R.; Bignozzi, C. A.; Heimer, T. A.; Castellano, F. N.; Meyer, G. J. *J. Phys. Chem. B* **1997,** *101*, 2591-2597.

(88) Johansson, P. G.; Kopecky, A.; Galoppini, E.; Meyer, G. J. *J. Am. Chem. Soc.* **2013,** *135*, 8331-8341.

(89) Prasittichai, C.; Avila, J. R.; Farha, O. K.; Hupp, J. T. *J. Am. Chem. Soc.* **2013,** *135*, 16328-16331.

(90) Katz, M. J.; DeVries Vermeer, M. J.; Farha, O. K.; Pellin, M. J.; Hupp, J. T. *J. Phys. Chem. B* **2014**.

(91) Alibabaei, L.; Farnum, B. H.; Kalanyan, B.; Brennaman, M. K.; Losego, M. D.; Parsons, G. N.; Meyer, T. J. *Nano Lett.* **2014,** *14*, 3255-3261.

(92) Yum, J.-H.; Moehl, T.; Yoon, J.; Chandiran, A. K.; Kessler, F.; Gratia, P.; Grätzel, M. *J. Phys. Chem. C* **2014,** *118*, 16799-16805.

(93) Hamann, T. W. *Dalton Trans.* **2012,** *41*, 3111-3115.

(94) Sapp, S. A.; Elliott, C. M.; Contado, C.; Caramori, S.; Bignozzi, C. A. *J. Am. Chem. Soc.* **2002,** *124*, 11215-11222.

(95) Yella, A.; Lee, H.-W.; Tsao, H. N.; Yi, C.; Chandiran, A. K.; Nazeeruddin, M. K.; Diau, E. W.-G.; Yeh, C.-Y.; Zakeeruddin, S. M.; Grätzel, M. *Science* **2011,** *334*, 629-634.

(96) Yum, J.-H.; Chen, P.; Grätzel, M.; Nazeeruddin, M. K. *ChemSusChem* **2008,** *1*, 699-707.

(97) Hu, K.; Robson, K. C. D.; Beauvilliers, E. E.; Schott, E.; Zarate, X.; Arratia-Perez, R.; Berlinguette, C. P.; Meyer, G. J. *Journal of the American Chemical Society* **2013,** *136*, 1034-1046.

(98) Cappel, U. B.; Smeigh, A. L.; Plogmaker, S.; Johansson, E. M. J.; Rensmo, H. k.; Hammarström, L.; Hagfeldt, A.; Boschloo, G. *The Journal of Physical Chemistry C* **2011,** *115*, 4345-4358.

(99) Green, M. A.; Emery, K.; Hishikawa, Y.; Warta, W.; Dunlop, E. D. *Progress in Photovoltaics: Research and Applications* **2014,** *22*, 701-710.

(100) Logitech. If You've Got Light, You've Got Power: Logitech Introduces Solar-Powered Keyboard. Logitech: 2010. http://www.logitech.com/en-us/press/press-releases/7743 (accessed 10/15/2014).

(101) Logitech. Type With Light on Logitech's New Solar Keyboard for Mac, iPad, and iPhone. Logitech: 2012. http://news.logitech.com/press-release/consumer-products/type-light-logitechs-new-solar-keyboard-mac-ipad-and-iphone (accessed 10/15/2014).

(102) Barraud, E. Stained Glass Solar Windows for the Swiss Tech Convention Center. Mediacom: 2012. http://actu.epfl.ch/news/stained-glass-solar-windows-for-the-swiss-tech-con/ (accessed 10/15/2014).

Chapter 2. Excited State Relaxation of Ruthenium Polypyridyl Compounds Relevant to Dye-Sensitized Solar Cells

In part a compilation of one publication.[1]

This work was collaborative in conjunction with Patrik G. Johansson[†] *and Maria Abrahamsson*[‡]

[†]*Johns Hopkins University, Baltimore, Maryland*

[‡]*Chalmers University of Technology, Göteborg, Sweden*

2.1 Introduction

Excited state relaxation of the thermally equilibrated excited state of $Ru(bpy)_3^{2+}$ was quantified in considerable detail by Crosby and coworkers.[2-4] Temperature-dependent photoluminescence (PL) measurements revealed the presence of three closely spaced metal-to-ligand charge transfer (MLCT) excited states that behave as a single state near room temperature. Later, experimental and theoretical analysis identified a fourth MLCT state that accounted for the weak temperature dependence near room temperature.[5-8] Excitation spectra revealed that intersystem crossing from upper excited states to the thermally equilibrated (thexi) states occurred with a quantum yield of unity.[4,9] Higher in energy are ligand field (LF) states, sometimes called d-d states, which are antibonding with respect to metal-ligand bonds, Scheme 1. Internal conversion from the MLCT states to the LF states can therefore lead to ligand loss photochemistry. As was emphasized by Crosby, the Ru center induces spin-orbit coupling that makes spin a poor quantum number for these electronic excited states.[4,10-11] Nevertheless, the initially formed excited state is necessarily singlet in character while the thexi states have considerable triplet character. In this chapter, the term photoluminescence is used, which implies no restrictions on the spin change that accompanies excited state relaxation.

While it is often tacitly assumed that a Jablonski diagram like that shown in Figure 2.1 for $Ru(bpy)_3^{2+}$ is applicable to all MLCT excited states, there is evidence to suggest otherwise. For example, nonunity intersystem crossing yields have been observed under a variety of conditions.[12-18] Excitation wavelength dependent quantum yields for photochemical ligand loss have been reported.[19-22] Furthermore, the MLCT excited states are often found to be acutely sensitive to their external environment.[5,23-31] It is also noteworthy that excited-state relaxation pathways in compounds of lower symmetry, like the *cis*-$Ru(bpy)_2X_2$, where X is a halide or pseudohalide, have received remarkably little attention even though they represent the class of compounds most commonly utilized in dye-sensitized solar cells.[32-36] In this chapter, photophysical studies of this type are reported for compounds in fluid solution and anchored to semiconducting metal oxide surfaces.

Previous studies of MLCT excited states anchored to semiconductor surfaces have been limited, mainly because of rapid electron transfer to the semiconductor acceptor states.[37-44] However, it is possible to enhance the excited state lifetime by shifting the semiconductor acceptor states to energies where electron transfer is unfavored.[45-46] For example, Sutin and Clark took advantage of the Nernstian shift of the rutile TiO_2 conduction band edge position to abstract reorganization energies for interfacial electron transfer; excited state injection was favored under acidic conditions and was not observed when the pH was raised.[47]

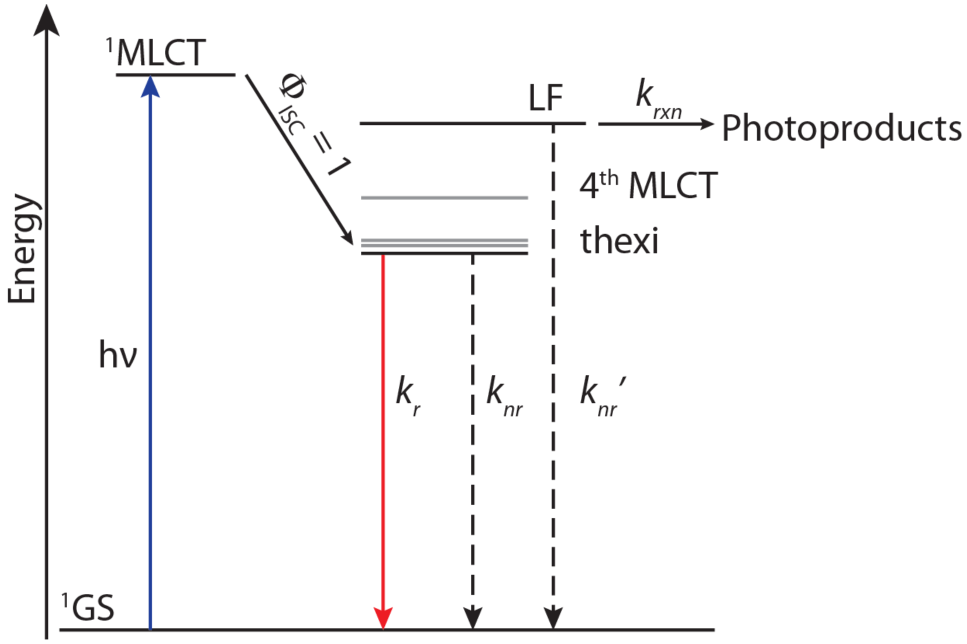

Figure 2.1. Jablonski diagram for $Ru(bpy)_3^{2+}$

In another example, the MLCT excited states of *cis*-Ru(bpy)$_2$(ina)$_2^{2+}$, where ina is isonicotinic acid, anchored to mesoporous TiO$_2$ nanocrystalline (anatase) thin films displayed non-unity intersystem crossing yields with an increased activation barrier for MLCT → LF internal conversion.[48] Lateral intermolecular energy transfer across the surface has also been quantified in these same TiO$_2$ thin films.[49-52]

There exists compelling evidence that excited state electron transfer from ruthenium polypyridyl compounds to anatase TiO$_2$ occurs on ultrafast time scales under many experimental conditions.[37-44] In addition to these subpicosecond electron transfer processes, there is evidence for slower interfacial electron transfer reactions that were likely occurring from the thexi state.[40-42,44] In principle, PL can report on the yields and rate constants for interfacial electron transfer from the thexi state. Several previous studies have reported data of exactly this type.[53-56] Furthermore, since PL is a contactless technique it can, in principle, be used for the *in situ* characterization of operational dye-sensitized solar cells. As PL is an indirect probe of electron transfer, its use as an *in situ* tool for solar cell efficiency requires that the excited states be thoroughly characterized. This chapter reports carefully designed experiments motivated toward this goal. Temperature dependent PL studies of compounds of the general type *cis*-Ru(LL)$_2$(X)$_2$, where LL is a diimine ligand and X is CN$^-$ or NCS$^-$, Figure 2.2, have been contrasted with the well-known Ru(bpy)$_3^{2+}$ and Os(bpy)$_3^{2+}$, where bpy is 2,2'-bipyridine, to identify relaxation pathways. In addition, the photophysical properties of *cis*-Ru(dcbH$_2$)$_2$(NCS)$_2$, often called N3, anchored to mesoporous nanocrystalline (anatase) TiO$_2$ and ZrO$_2$ thin films have been characterized.

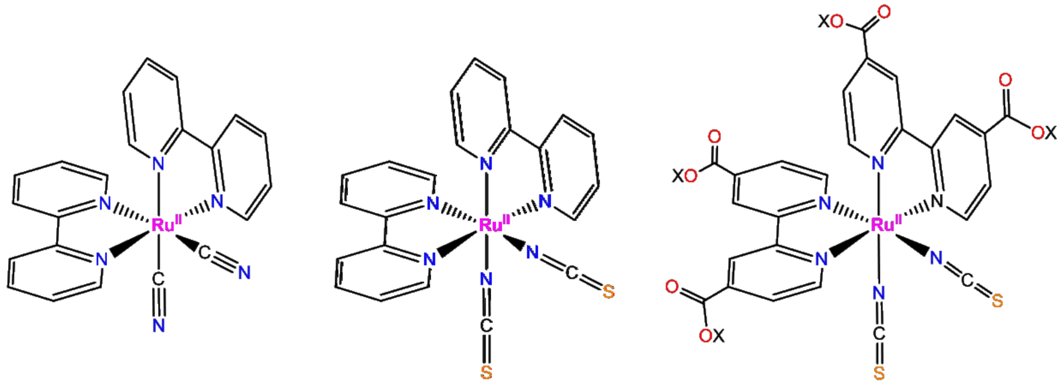

Figure 2.2. Chemical structures of molecules studied: (left to right) *cis*-Ru(bpy)$_2$(CN)$_2$, *cis*-Ru(bpy)$_2$(NCS)$_2$, and *cis*-Ru(dcbX$_2$)$_2$(NCS)$_2$ where X = H (N3) or X = tetrabutylammonium (N712).

An important finding in this chapter is that the population of dissociative LF excited states is unlikely to lead to unwanted photochemistry in dye-sensitized solar cells based on these sensitizers. This conclusion stands in sharp contrast to what one would anticipate based on the spectrochemical series, plausible explanations for this behavior are discussed.

2.2 Experimental

2.2.1 Materials

The following reagents were used as received from the following commercial suppliers: acetonitrile (Burdick & Jackson, spectrophotometric grade); ethanol (Pharmco-Aaper, 200 proof anhydrous); *tert*-butanol (Fisher, certified); propylene carbonate (Sigma-Aldrich, 99.7% anhydrous); deionized water; *n*-tetrabutylammonium hydroxide (TBAOH; Sigma-Aldrich, 1.0 M in methanol); potassium hydroxide (Fisher Scientific, >85%); potassium hexafluorophosphate (KPF_6; Aldrich, 98%); $[Ru(bpy)_3]Cl_2{\cdot}6H_2O$ (Aldrich, 99.95%); *cis*$[Ru(dcbH_2)_2(NCS)_2]$ (Solaronix); titanium(IV) isopropoxide (Sigma-Aldrich, 97%); zirconium(IV) isopropoxide (Alfa Aesar, 70% in *n*-propanol); argon gas (Airgas, >99.998%); nitrogen gas (Airgas, 99.999%); glass microscope slides (Fisher Scientific, 1 mm thick). $[Ru(bpy)_2(CN)_2]$, $[Ru(bpy)_2(NCS)_2]$, and $[Os(bpy)_3](PF_6)_2$ were available from previous studies.

2.2.2 Preparations.

$[Ru(bpy)_3](PF_6)_2$ was prepared from the anion metathesis reaction of $[Ru(bpy)_3]Cl_2{\cdot}6H_2O$ with KPF_6. The neutral $[Ru(dcbH_2)_2(NCS)_2]$ was fully deprotonated to form $(TBA)_4[Ru(dcb)_2(NCS)_2]$ using TBAOH similar to the method reported by Nazeeruddin *et al.*[57]

Nanocrystallites of TiO_2 (anatase, ~15 nm in diameter) and ZrO_2 (~15 nm in diameter) were prepared by hydrolysis of $Ti(i\text{-}OPr)_4$ or $Zr(i\text{-}OPr)_4$, respectively, using a sol-gel method previously described in the literature.[58] The sols were cast as transparent mesoporous thin films by doctor blading onto glass microscope slides with the aid of transparent cellophane tape as a mask and spacer (~10 μm thick). The films were sintered at 450°C for 30 min under an atmosphere of O_2 flow and either used immediately for surface attachment or stored in an oven for future use. The thin films were treated with aqueous base (pH 11) for ~15 min and rinsed with a 50:50 (v/v) mixture of CH_3CN/*tert*-butanol before sensitization in concentrated dyeing solutions. The sensitized thin films were then rinsed and stored in neat CH_3CN prior to use.

2.2.3 Spectroscopy.

UV-Visible Absorption. Steady-state UV-visible (vis) absorption spectra were obtained on a Varian Cary 50 spectrophotometer at room temperature in 1.0 cm pathlength quartz or Pyrex cells.

Infrared Absorption. Attenuated Total Reflectance (ATR) FTIR absorbance spectra were obtained using a Thermo Scientific Nicolet Nexus 670 spectrophotometer with a Golden Gate ATR accessory. The measurements were made under an N_2 atmosphere and the spectra were averaged for 64 scans and background corrected with 4 cm^{-1} resolution.

^{1}H-NMR. The ^{1}H-NMR spectra were obtained on a Bruker Avance 400 MHz instrument in CH_3OD at room temperature (25.0°C) and calibrated to residual solvent peaks.

Steady State Photoluminescence. Steady-state photoluminescence (PL) spectra were obtained with a Spex Fluorolog spectrophotometer equipped with a 450 W Xe lamp or an argon ion laser for the excitation source. PL spectra of argon purged solutions were acquired at room temperature with photoluminescence detected at a right angle to the excitation beam. Quantum yields were measured versus $Os(bpy)_3^{2+}$ in CH_3CN as the standard ($\Phi_r = 0.005$) using the optically dilute method.[59-60] Sensitized metal oxide thin films were measured by placing the glass film diagonally in a 1.0 cm square quartz cell, exciting 45° to the film surface, and monitoring from the front face of the sample.

Temperature Dependent, Time Resolved Photoluminescence. Nanosecond time resolved PL data were acquired at a right angle to excitation with pulsed 450 or 500 nm laser light from a N_2 dye laser (Photon Technologies International, GL301, Coumarin 450 or 500 (Exciton)). Transient data was digitized on a computer-interfaced oscilloscope (LeCroy LT322) with 5 ns time resolution. Typically, 300 laser shots were averaged for each kinetic trace. For the temperature dependence studies, the sample temperature was maintained to ±0.1°C using a liquid nitrogen cryostat (UniSoku CoolSpek USP-203-B).

Photolysis. Photolysis experiments were performed with the Spex Fluorolog spectrophotometer. Argon saturated samples were irradiated with light for 3 hours at an elevated temperature of +70.0°C which was maintained to ±0.1°C using a liquid nitrogen cryostat (UniSoku CoolSpek USP-203-B).

2.2.4 Data Fitting.

Kinetic data fitting and Arrhenius analyses were performed in Origin 8.5 with least-squares error minimization accomplished using the Levenberg-Marquardt iteration method. Solution sample lifetimes were fit to single exponential decay kinetics over at least three half-lives, Equation (2.1).

$$I(t) = I_0 exp\left(\frac{-t}{\tau_{obs}}\right) + c \tag{2.1}$$

The temperature dependent lifetimes were converted to observed rates and fitted to the modified Arrhenius expression, Equation (2.2). Unless otherwise noted, the Arrhenius analyses were performed with only one activation energy term (n=1) as the inclusion of a second (n=2) did not improve the fit.

$$\frac{1}{\tau_{obs}} = k_0 + \sum_{i=1}^{n}\left[A_i exp\left(\frac{-E_a}{k_B T}\right)\right] \tag{2.2}$$

2.3 Results

Representative absorption and photoluminescence spectra of the *cis*-$Ru(bpy)_2(X)_2$ compounds dissolved in acetonitrile are shown in Figure 2.3. The fully deprotonated form of *cis*-$Ru(dcbH_2)_2(NCS)_2$, $(TBA)_4[Ru(dcb)_2(NCS)_2]$ also known as N712, was studied in most detail for solubility reasons. The three compounds possess two MLCT absorption bands centered around 500 nm and between 340 – 380 nm as well as ligand centered π-π^* transitions between 290 and 310 nm. Visible light excitation resulted in room temperature photoluminescence (PL). The PL maxima of *cis*-$Ru(bpy)_2(NCS)_2$ at 745 nm was similar to that of $(TBA)_4[Ru(dcb)_2(NCS)_2]$ which occurred around 725 nm. The PL maximum of *cis*-$Ru(bpy)_2(CN)_2$ was blue-shifted in comparison to the isothiocyanate compounds and maximized at 680 nm; see Figure 2.3. The photophysical characteristics of the isothiocyanate and cyanide ligated compounds are given in Table 2.1 along with $Ru(bpy)_3^{2+}$ and $Os(bpy)_3^{2+}$ for comparison. All of the compounds studied exhibited low energy absorption and PL maxima that were red-shifted compared to $Ru(bpy)_3^{2+}$.

The isothiocyanate compounds were characterized via ATR-IR. A ν_{CN} = 2120 cm^{-1} and ν_{CS} = 768 cm^{-1} were observed in good agreement with literature values for N-coordinated isothiocyanate.[49,57] Likewise, the *cis*-$Ru(bpy)_2(NCS)_2$ sample used in this study exhibited ν_{CN} = 2099 cm^{-1} and ν_{CS} = 795 cm^{-1}.[61-62] Had the S-coordinated isomer been present in an appreciable amount, lower energy stretches would have been expected with $\nu_{CN} \approx 2056$ cm^{-1} and $\nu_{CS} \approx 700$ cm^{-1}.[63] There was no evidence for the presence of the *trans*-$Ru(dcbH_2)_2(NCS)_2$ isomer that exhibits a characteristic UV-vis absorption spectrum.[64] Furthermore, there is no literature precedence for formation of the *trans*-isomer by photoisomerization of *cis*-$Ru(dcbH_2)_2(NCS)_2$. The N-/N-coordinated *cis*-isomer is the only reported isomer for the $Ru(bpy)_2(NCS)_2$ compound.[64]

The ^{1}H-NMR analysis of *cis*-$Ru(dcbH_2)_2(NCS)_2$ was in good agreement with previous studies. The ^{1}H-NMR resonance at 9.58 ppm has been assigned to the N-/N-coordinated isothiocyanate isomer that integrated to ~98-99% of the total concentration. Weak resonances at 9.92 and 9.51 ppm have been attributed to the S-coordinated isomers that comprised the remaining ~1-2% of the sample.[63]

Pulsed light excitation of the compounds in acetonitrile yielded MLCT excited states that decayed to the ground state by a first-order kinetic model. The excited state lifetimes obtained at room temperature, τ_o, for the isothiocyanate compounds were comparable to $Os(bpy)_3^{2+}$ ranging from 27 to 115 ns. The quantum yields for PL, Φ_{PL}, were quantified by the optically dilute method with $Os(bpy)_3^{2+*}$ employed as the actinometer.[59] A reported $\Phi_{PL} = 0.005$ for $Os(bpy)_3^{2+*}$ in argon-saturated acetonitrile was utilized and any error in this value would result in systematic deviations of the data listed in Table 2.1.[60]

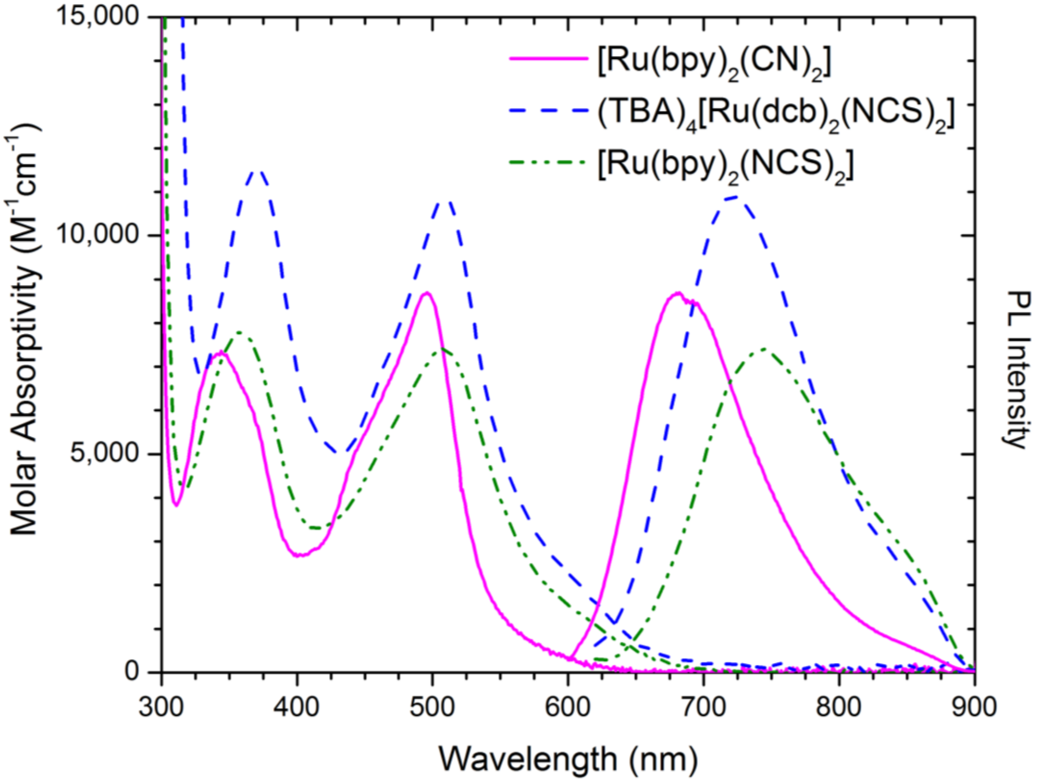

Figure 2.3. Absorption and photoluminescence spectra of *cis*-Ru(bpy)$_2$(CN)$_2$ (magenta, solid), *cis*-Ru(bpy)$_2$(NCS)$_2$ (green, dash dot), and (TBA)$_4$[Ru(dcb)$_2$(NCS)$_2$] (blue, dashed) in acetonitrile.

Compound	Solvent[a]	Abs. (nm)[b]	ε ($M^{-1}cm^{-1}$)[b]	PL (nm)	τ_{obs} (ns)[c]	k_{obs} (s^{-1})	Φ_{PL}[d]	k_r (s^{-1})[e]	k_{nr} (s^{-1})[f]
Ru(bpy)$_3^{2+}$	ACN	450	14,600	615	825	1.2×10^6	0.062†	7.5×10^4	1.1×10^6
	PC	452		615	891	1.1×10^6	0.071†	8.0×10^4	1.0×10^6
Os(bpy)$_3^{2+}$	ACN	640	1,800	736	59	1.7×10^7	0.005‡	8.5×10^4	1.7×10^7
	PC	640		736	52	1.9×10^7	0.004	7.7×10^4	1.9×10^7
Ru(bpy)$_2$(CN)$_2$	ACN	492	8,700	682	244	4.1×10^6	0.016	6.6×10^4	4.0×10^6
	PC	495		679	239	4.2×10^6	0.016	6.7×10^4	4.1×10^6
Ru(bpy)$_2$(NCS)$_2$	ACN	505	7,400	745	27	3.7×10^7	0.0006	2.2×10^4	3.7×10^7
	PC	507		743	29	3.4×10^7	0.0007	2.4×10^4	3.4×10^7
Ru(dcb)$_2$(NCS)$_2^{4-}$	ACN	507	10,900	723	115	8.7×10^6	0.0035	3.1×10^4	8.7×10^6
	PC	515		732	85	1.2×10^7	0.0020	2.4×10^4	1.2×10^7
Ru(dcbH$_2$)$_2$(NCS)$_2$	PC	529		780	30	3.3×10^7	0.0006	2.0×10^4	3.3×10^7

[a] ACN = Acetonitrile; PC = Propylene Carbonate. [b] Maxima of the lowest energy MLCT absorption. [c] Lifetimes are ±5%. [d] PL quantum yields measured using Os(bpy)$_3^{2+}$ in ACN as standard with errors of ±10%. [e] $k_r = \Phi_{PL} \cdot k_{obs}$. [f] $k_{nr} = k_{obs} - k_r$ †*J. Am. Chem. Soc.* **1983**, *105*, 5583. ‡*J. Phys. Chem.* **1986**, *90*, 3722. All measurements were obtained at +19°C ± 2°C. Wavelengths are ±2 nm.

Table 2.1. Photophysical data of the compounds in solution at room temperature (+20°C).

The PL quantum yield for *cis*-$Ru(dcb)_2(NCS)_2^{4-}$ was 3.5 x 10^{-3} in acetonitrile and 2.0 x 10^{-3} in propylene carbonate, both values being slightly less than the reported value of 5 x 10^{-3} for $Os(bpy)_3^{2+}$ in acetonitrile and the measured value of 4 x 10^{-3} in propylene carbonate. The quantum yields for *cis*-$Ru(bpy)_2(NCS)_2$ and *cis*-$Ru(dcbH_2)_2(NCS)_2$ were quite small, on the order of (5 – 7) x 10^{-4}. In addition to having a longer excited-state lifetime of around 240 ns in both solvents studied, *cis*-$Ru(bpy)_2(CN)_2$ also exhibited a PL quantum yield between that of $Ru(bpy)_3^{2+}$ and $Os(bpy)_3^{2+}$ equal to 1.6 x 10^{-2}.

Manipulation of the sample temperature from -40.0°C to +70.0°C in acetonitrile and from -40.0°C to +100.0°C in propylene carbonate led to shorter observed excited state lifetimes as expected for thermal activation to upper excited states. The observed relaxation rate constants for $Ru(bpy)_3^{2+*}$, $Os(bpy)_3^{2+*}$, *cis*-$Ru(bpy)_2(CN)_2^*$, and *cis*-$Ru(bpy)_2(NCS)_2^*$ with respect to temperature could all be modeled with one activation parameter through an Arrhenius analysis.

Two activation parameters were required to fit the Arrhenius data for $(TBA)_4[Ru(dcb)_2(NCS)_2]$, shown in Figure 2.4.A, which yielded activation energies of 4620 cm^{-1} and 750 cm^{-1} with corresponding pre-exponential factors of 1.7 x 10^{15} s^{-1} and 1.3 x 10^{8} s^{-1}, respectively. Similar results were obtained in propylene carbonate solution, although the activation energy values needed to be fixed for the function to converge. Specifying activation energies of 4620 and 750 cm^{-1}, taken from the acetonitrile values, allowed the function to converge. The inset of Figure 2.4.B depicts the fitted data with pre-exponential factors of 4.8 x 10^{15} s^{-1} and 9.7 x 10^{7} s^{-1} that were in good agreement with the acetonitrile data. The temperature range for $(TBA)_4[Ru(dcb)_2(NCS)_2]$ in propylene carbonate was restricted from -40.0°C to +70.0°C as irreversible photochemistry was observed at higher temperatures.

The temperature-dependent relaxation rates are shown in Figure 2.5 and the excited-state decay parameters obtained from the Arrhenius analyses are collected in Table 2.2. The $Ru(bpy)_3^{2+}$ data yielded an activation energy around 4200 cm^{-1} while the $Os(bpy)_3^{2+}$ value was approximately 420 cm^{-1}, or about one tenth of the ruthenium value. The bpy-based compounds *cis*-$Ru(bpy)_2(X)_2$, where X is either NCS^- or CN^-, exhibited temperature-dependent activation to only one upper excited state with activation energies less than 1000 cm^{-1}. The fully deprotonated, tetraanionic $(TBA)_4[Ru(dcb)_2(NCS)_2]$ compound exhibited thermal population to two different upper excited states with one activation energy less than 1000 cm^{-1} and the other around 4600 cm^{-1} as described above.

The sensitizer *cis*-$Ru(dcbH_2)_2(NCS)_2$ was attached to base pretreated TiO_2 and ZrO_2, *cis*-$Ru(dcb)_2(NCS)_2/TiO_2$ and *cis*-$Ru(dcb)_2(NCS)_2/ZrO_2$. Under these conditions, steady-state PL was observed upon light excitation of the sensitized thin films. The PL spectrum measured for $Ru(dcb)_2(NCS)_2/ZrO_2$ was in line with that expected for this sensitizer and was slightly broader than that observed in fluid solution. The *cis*-$Ru(dcb)_2(NCS)_2/TiO_2$ PL spectrum was red-shifted by 720 cm^{-1} relative to *cis*-$Ru(dcb)_2(NCS)_2/ZrO_2$. The spectrum was also broadened in comparison with the solution data. Pulsed light excitation of *cis*-$Ru(dcb)_2(NCS)_2/TiO_2$ led to a short-lived PL decay that was adequately described by a first-order kinetic model, see Figure 2.6.A. Temperature-dependent lifetimes were analyzed from -40.0°C to +40.0°C with an activation energy of 690 cm^{-1} abstracted from the data as shown in Figure 2.6.A.

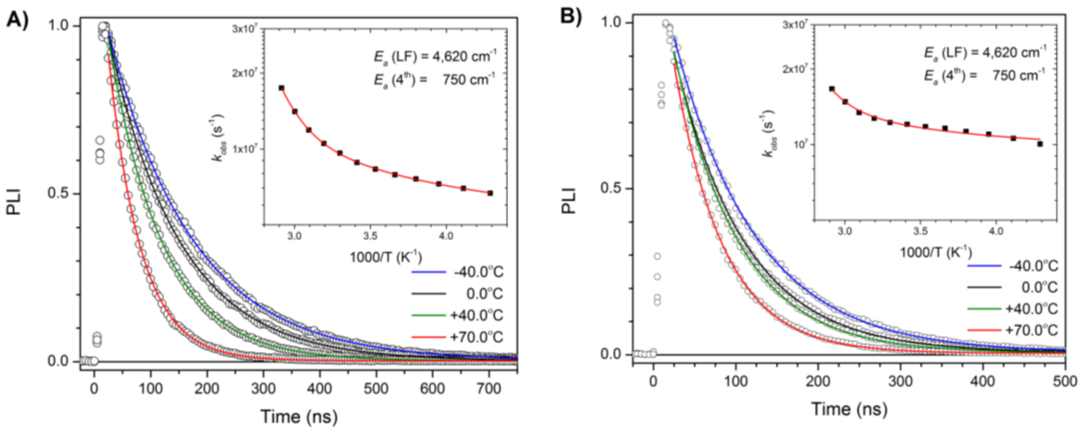

Figure 2.4. Time-resolved PL data measured after pulsed laser excitation of $(TBA)_4[Ru(dcb)_2(NCS)_2]$ in neat acetonitrile (A) and propylene carbonate (B) at the indicated temperatures. The insets depict Arrhenius analyses of the kinetic data.

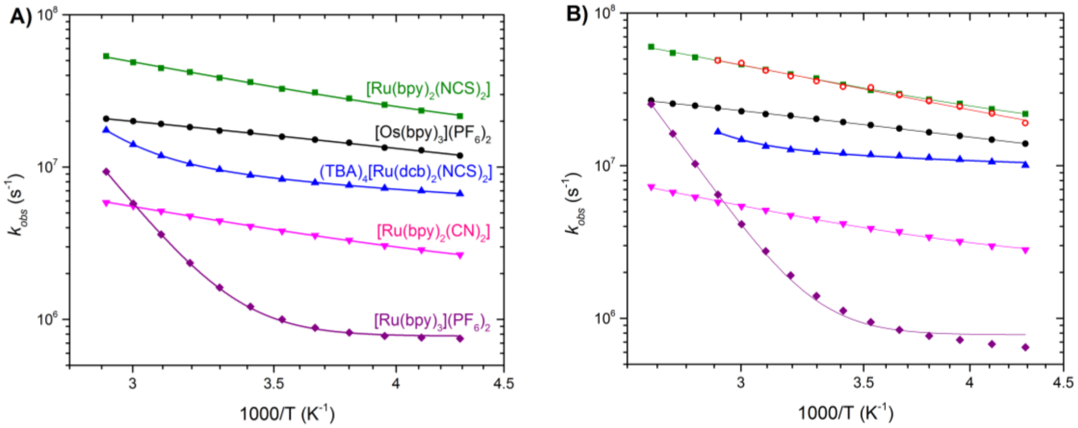

Figure 2.5. Arrhenius comparisons in acetonitrile (A) and propylene carbonate (B) of the studied compounds. $Ru(bpy)_3^{2+}$ (purple, diamond); *cis*-$Ru(bpy)_2(CN)_2$ (magenta, down triangle); *cis*-$Ru(dcb)_2(NCS)_2^{4-}$ (blue, up triangle); $Os(bpy)_3^{2+}$ (black, circle); *cis*-$Ru(bpy)_2(NCS)_2$ (green, square); *cis*-$Ru(dcbH_2)_2(NCS)_2$ (red, open circle).

Compound	**Solvent**	**Temp. Range (K)**	k_0' **(s^{-1})**	k_1 **(s^{-1})**	k_1/k_0'	**E_a (cm^{-1})**
$Ru(bpy)_3^{2+}$	ACN	233 - 343	7.8×10^5	4.4×10^{14}	5.6×10^8	**4,240**
	PC	233 - 373	7.8×10^5	4.0×10^{14}	5.1×10^8	**4,310**
$Os(bpy)_3^{2+}$	ACN	233 - 343	5.1×10^6	8.9×10^7	17	**410**
	PC	233 - 373	6.6×10^6	1.0×10^8	16	**430**
$Ru(bpy)_2(CN)_2$	ACN	233 - 343	1.8×10^6	1.2×10^8	67	**810**
	PC	233 - 373	2.3×10^6	1.7×10^8	79	**930**
$Ru(bpy)_2(NCS)_2$	ACN	233 - 343	1.4×10^7	1.2×10^9	86	**810**
	PC	233 - 373	1.5×10^7	9.1×10^8	67	**780**
$Ru(dcb)_2(NCS)_2^{4-}$	ACN	233 - 343	5.5×10^6	1.7×10^{15}	3.1×10^8	**4,620**
				1.3×10^8	24	**750**
	PC	233 - 343	9.7×10^6	8.3×10^{14}	8.6×10^7	***4,620****
				8.5×10^7	9	***750****
$Ru(dcbH_2)_2(NCS)_2$	PC	233 - 313	9.5×10^6	6.6×10^8	70	**670**

ACN = Acetonitrile. PC = Propylene Carbonate. *Denotes values held constant during fitting, see text for details.

Table 2.2. Arrhenius parameters for the compounds in fluid solution.

The PL decays of *cis*-$Ru(dcb)_2(NCS)_2/ZrO_2$ obtained from -40.0°C to +70.0°C could not be adequately described by a first-order kinetic model and fit well to a biexponential model. The fast and slow kinetic components of the PL decays were analyzed using a global fit to the activation energy with independent k_0 and k_1 terms for each component yielding an activation energy of 890 cm^{-1}, see Figure 2.6.B. The excite-state decay parameters from the Arrhenius analyses for *cis*-$Ru(dcb)_2(NCS)_2/TiO_2$ and *cis*-$Ru(dcb)_2(NCS)_2/ZrO_2$ are collected in Table 2.3. The PL decay kinetics were found to be independent of the observation wavelength for both *cis*-$Ru(dcb)_2(NCS)_2/TiO_2$ and *cis*-$Ru(dcb)_2(NCS)_2/ZrO_2$.

Photolysis of $(TBA)_4[Ru(dcb)_2(NCS)_2]$ with 510 nm light was performed in acetonitrile at +70°C for three hours. After photolysis, the lowest energy MLCT maximum blue-shifted from 507 to 475 nm and decreased in intensity, Figure 2.7.A. Photolysis of $Ru(dcb)_2(NCS)_2/TiO_2$ with 532 nm excitation under otherwise identical conditions did not lead to any significant change in the UV-Vis absorbance spectrum, Figure 2.7.B.

2.4 Discussion

The activated relaxation pathways abstracted from temperature-dependent measurements for [*cis*-$Ru(dcb)_2(NCS)_2]^{4-*}$ and *cis*-$Ru(dcb)_2(NCS)_2^{*}/TiO_2$ are summarized in Figure 2.8. The potential energy surfaces for the ground, thexi, and Franck-Condon (^{1}FC) states were placed on the indicated electrochemical scale from previously reported data.[33] It should be emphasized that the data provides the activation energy between states, not necessarily their absolute values. Therefore, the minima for the 4th MLCT and the LF states are unknown.

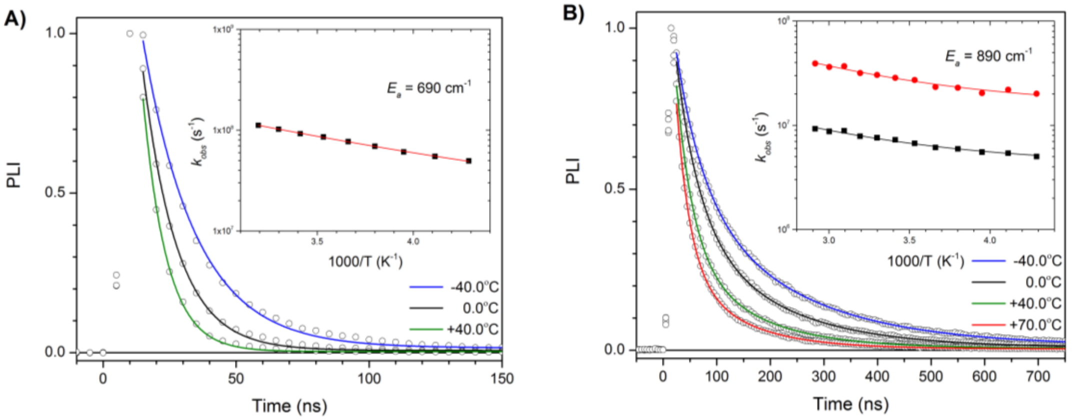

Figure 2.6. Time-resolved photoluminescence decays of Ru(dcb)$_2$(NCS)$_2$/TiO$_2$ (A) and Ru(dcb)$_2$(NCS)$_2$/ZrO$_2$ (B) in neat acetonitrile baths. Insets show the Arrhenius analyses with activation energies equal to 690 cm^{-1} for the TiO$_2$ data and 890 cm^{-1} for the ZrO$_2$ data.

MO_2	**Abs. (nm)**	**PL (nm)**	**Temp. Range (K)**	**k_0' (s^{-1})**	**k_1 (s^{-1})**	**k_1/k_0'**	**E_a (cm^{-1})**
TiO_2	532	765	233 - 313	1.7×10^7	2.2×10^9	130	**690**
ZrO_2	508	725	233 - 343	4.2×10^6	2.2×10^8	52	**890**
				1.5×10^7	1.0×10^9	67	

Table 2.3. Arrhenius parameters for *cis*-Ru(dcb)$_2$(NCS)$_2$/MO_2.

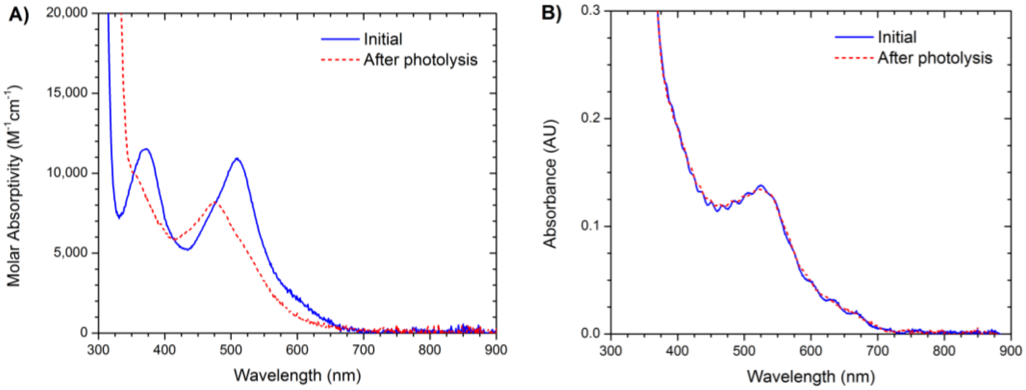

Figure 2.7. Absorption spectra of (a) $(TBA)_4[Ru(dcb)_2(NCS)_2]$ and (b) $Ru(dcb)_2(NCS)_2/TiO_2$ in CH_3CN before and after photolysis at +70°C for three hours.

The analysis implies that the activation energy for internal conversion from the thexi state to ligand field (LF) states increased when the compound was anchored to the semiconductor surface. Furthermore, under all conditions studied, the LF states were not as accessible to these MLCT excited states as the spectrochemical series would predict. Below the kinetic modeling is discussed from which the activational parameters were abstracted, followed by a discussion of the photophysical behavior in fluid solution and at metal oxide interfaces.

2.4.1 Kinetic Modeling

The detailed studies of Crosby and coworkers mentioned in the Introduction were performed for $Ru(bpy)_3^{2+}$ immobilized in polymethylmethacrylate (PMMA) thin films from 4 to 350 K.[2-3] Quantum yield and lifetimes data enabled the temperature dependence of both the radiative and the nonradiative rate constants to be quantified. Measurements below 5 K were required to resolve the three closely spaced electronic states that have significant Boltzmann population and behave as one state near room temperature. Since this pioneering work, there have been no subsequent studies of this scope. Far more common is to measure excited state lifetimes over a limited temperature range as is reported herein.[5-6,65-69] With temperatures above the fluid-to-glass transition of the solvent, the data is often described by a single activational process plus a constant, k_o, Equation (2.3).

$$\frac{1}{\tau_{obs}} = k_0 + A_1 \exp\left(\frac{-E_a}{k_B T}\right) \tag{2.3}$$

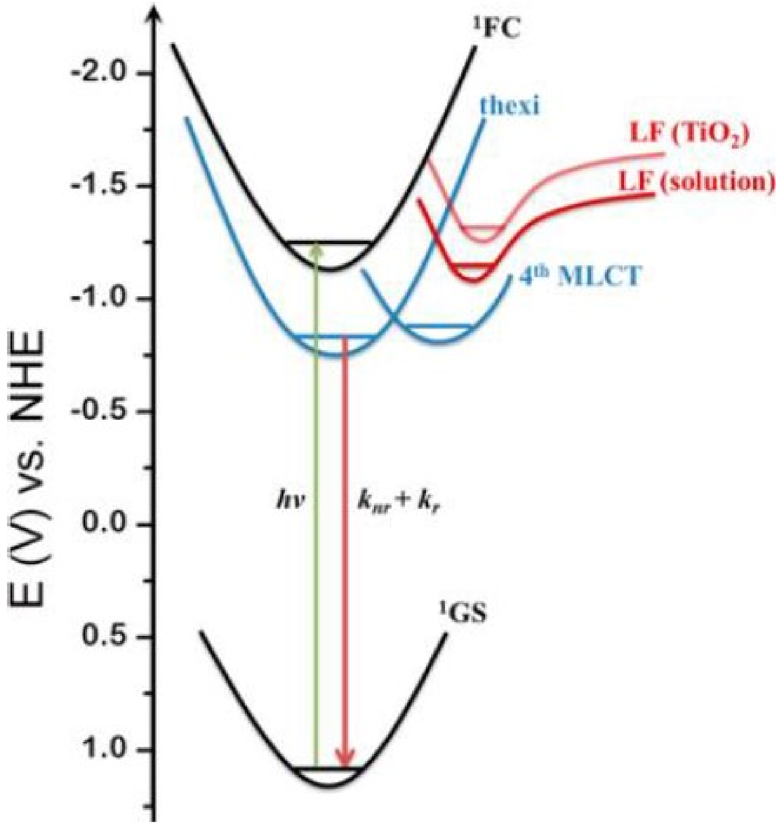

Figure 2.8. Excited-state potential energy diagram

Some researchers have elected to fix k_o to a limiting value measured at lower temperatures.[5,66] In these studies, this procedure was problematic as the lifetimes were temperature dependent over all ranges studied and fixing k_o to discrete values led to quantitatively different activational parameters. The k_0 value was therefore allowed to float in the minimization process. Equation (2.3) was found to satisfactorily fit all of the data described herein with only one exception in $(TBA)_4[Ru(dcb)_2(NCS)_2]^*$ where a second activational process was needed. The activational energy reported in this chapter differs from that reported previously by Balzani and coworkers for *cis*-$Ru(bpy)_2(CN)_2$; their experimental data was in good agreement with the data reported here, but the kinetic analysis differed.[32]

2.4.2 Fluid Solution

The activational parameters abstracted from excited-state relaxation of $Ru(bpy)_3^{2+*}$ and $Os(bpy)_3^{2+*}$ were in good agreement with previously published data.[5,68] Internal conversion from the thexi state to ligand field states, $(t_{2g})^5(\pi^*)^1 \rightarrow (t_{2g})^5(e_g^*)^1$, was irreversible with pre-exponential factors of 10^{14} s^{-1} and E_a of 4200 cm^{-1}. For $Os(bpy)_3^{2+*}$, the temperature range afforded by the acetonitrile or propylene carbonate solvents did not enable significant population of the ligand field states. Instead, a small temperature dependence was observed from which pre-exponential factors of 10^8 s^{-1} and E_a of 420 cm^{-1} were abstracted, parameters that are consistent with relaxation through the fourth MLCT excited state.[5,68]

Excited state relaxation of *cis*-$Ru(bpy)_2X_2$ can, in principle, be predicted based on the data for $Ru(bpy)_3^{2+*}$ and the spectrochemical series.[70] Replacement of one bpy ligand with two strong field CN^- ligands would be expected to raise the energy of the LF states and, assuming similar force constants, increase the activation energy. Indeed, at the highest temperatures utilized (+100 °C in propylene carbonate) there was no experimental evidence for thexi → LF internal conversion for *cis*-$Ru(bpy)_2(CN)_2^*$ and excited state relaxation was very similar to that measured for $Os(bpy)_3^{2+*}$ with contributions from only the 4th MLCT excited state.

Isothiocyanate is a weak field ligand positioned above the halides on the opposite end of the spectrochemical series with respect to cyanide.[70] Therefore, one would expect the ligand field states to be readily accessible from the MLCT excited state of *cis*-$Ru(bpy)_2(NCS)_2$. Surprisingly, this was not found to be the case and excited-state relaxation occurred through the fourth MLCT excited state. In fact, based on the spectrochemical series it is surprising in the first place that *cis*-$Ru(bpy)_2(NCS)_2^*$ displays room temperature photoluminescence with a lifetime of ~30 ns because related compounds with stronger field pyridine ligands, that is, *cis*-$Ru(bpy)_2(py)_2^{2+*}$, are nonemissive at room temperature with short excited-state lifetimes and high quantum yields for photochemical ligand loss; behavior consistent with facile population of antibonding ligand field states.[30-31,71-73] In the vast literature of isothiocyanate coordination chemistry as an ambidentate ligand, NCS^- is always considered a σ-donor with no π-accepting behavior.[74-75] Some more recent data, however, suggest that this is not necessarily the case.[76-80]

Schugar and coworkers noted that *cis*-$Ru(bpy)_2(NCS)_2$ displayed only a single ν_{CN} stretch.[61] Similar behavior was recently reported for a series of compounds of the type *cis*-$Ru(LL)_2(NCS)_2$.[77] The appearance of one single absorption band was surprising in two regards. First, a single IR absorption band was more consistent with the *trans*- form of the compound and the presence of an inversion center even though the geometry of these compounds and those in the present study clearly was *cis*-. Second, both an antisymmetric and symmetric ν_{CN} stretches were expected, yet only the single band was observed. This has been rationalized on the basis of the importance of two different resonance structures shown in Figure 2.9.[76-77] Backbonding into the π* orbitals of resonance structure A is approximately equivalent to backbonding to bipyridine which diminishes the energy separation between the anti-symmetric and symmetric ν_{CN} combinations. X-ray crystallographic data were analyzed to check for evidence of π backbonding of this nature in the solid state.[61,78-80] The five crystal structures of *cis*-$Ru(LL)_2(NCS)_2$ compounds exhibit an average N-C bond length of 1.13 Å that is consistent with an N-C triple bond and inconsistent with π backbonding from the Ru center. However, the average C-S bond length from crystal data is 1.65 Å that is intermediate between a C-S single bond, 1.81 Å, and a C-S double bond, 1.55 Å.[70] Therefore, the crystallographic data provides some support for the proposal that π backbonding into the nitrile portion of resonance structure A in Figure 2.9 is operative in the ground state.

The above discussion suggests that $NCS^- \rightarrow Ru^{II}$ backbonding may be more important in these compounds than the spectrochemical series predicts, at least in the ground electronic state. The ligand field strength in the excited state is potentially a more complicated issue. Upon light excitation, an electron is transferred from the Ru d-orbitals to the π * levels of the bpy ligand, Equation (2.4).

$$cis\text{-}Ru^{II}(bpy)_2(NCS)_2 + h\nu \rightarrow cis\text{-}Ru^{III}(bpy^-)(bpy)(NCS)_2^* \qquad (2.4)$$

The ligand field splitting parameter Δ_o is expected to be 30% larger for Ru^{III} than for Ru^{II}.[70,81] However, the formal oxidation states are most relevant to the initial formed Franck-Condon excited state because intersystem crossing and vibrational relaxation transfer charge back to the metal center in the thexi state. Nevertheless, the excited state is more Ru^{III} like than is the ground state. The appearance of absorption bands in the near infrared region for both the excited and oxidized state have been previously assigned as ligand-to-metal charge transfer absorptions and provide direct evidence for $NCS^- \rightarrow Ru$. Theoretical studies also indicated partial ‘hole transfer’ from the Ru to the sulfur atom in the isothiocyanate ligand.[82-85] Furthermore, electrochemical measurements have shown that the isothiocyanate oxidation is proximate to the metal centered $Ru^{III/II}$ redox process.[86]

The coordinated isothiocyanate ligand can be viewed as two resonance forms, Figure 2.9. Kaim has shown that upon oxidation of *cis*-$Ru^{II}(LL)_2(NCS)_2$, the decreased electron density at the ruthenium center promotes a structural conversion from A to B.[77] Indeed, recent time-resolved X-ray data indicates that the Ru-N(NCS) bond length decreases by 0.06 Å upon oxidation.[87] This may represent the most significant inner-sphere reorganization in these compounds that display unusually small reorganization energies for MLCT excitation[88] and excited-state electron transfer.[36]

The inductive effect brought about by substitution of the bipyridine ligands in the 4,4’- positions can rationalize the temperature dependence of *cis*-$Ru(bpy)_2(NCS)_2$, *cis*-$Ru(dcbH_2)_2(NCS)_2$, and $(TBA)_4[Ru(dcb)_2(NCS)_2]$. The electron-withdrawing carboxylic acid groups stabilize the thexi state thereby increasing the thexi-LF energy gap. On the other hand, carboxylate acts as an electron donor, such that $(TBA)_4[Ru(dcb)_2(NCS)_2]$ has

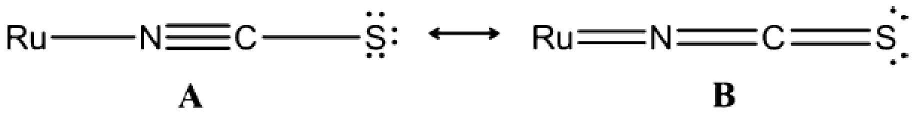

Figure 2.9. Resonance structure of isothiocyanate bound to ruthenium

the smallest thexi-LF energy gap. It is for this reason that the LF state population was only observed for this excited state.

2.4.3 Metal Oxide Interfaces

Steady state photoluminescence was observed from *cis*-$Ru(dcbH_2)_2(NCS)_2$ anchored to mesoporous thin films of insulating ZrO_2 and semiconducting TiO_2, abbreviated $Ru(dcb)_2(NCS)_2/MO_2$. The PL from $Ru(dcb)_2(NCS)_2/TiO_2$ was enhanced by a pretreatment of the TiO_2 thin films with aqueous base.[45-47] This treatment shifts the acceptor states in TiO_2 negative on an electrochemical scale (i.e., toward the vacuum level). Previous studies on closely related sensitized materials have shown that this pretreatment lowers the excited state injection yield measured when the films are immersed in neat acetonitrile.[89-90] Indeed under such conditions, the TiO_2 behaves more like an insulator in that the MLCT excited state does not undergo efficient electron transfer and the photophysical behavior was very similar to that observed for $Ru(dcb)_2(NCS)_2/ZrO_2$.

Lateral intermolecular energy transfer is known to complicate kinetic analysis of MLCT excited-state relaxation on semiconductor surfaces.[50-52] Energy migration leads to triplet-triplet annihilation reactions that are second-order in excited-state concentration. Monte–Carlo simulations were consistent with a $(30\text{ ns})^{-1}$ energy hopping rate for $Ru(bpy)_3^{2+}$ type sensitizers.[50] For the data presented in this chapter, excited-state decay was satisfactorily described by a first-order kinetic model, presumably because the irradiance was kept low and the short excited-state lifetimes resulted in inefficient energy transfer.

Infrared measurements were consistent with previous studies that indicate all of the carboxylic acid groups are deprotonated in the $Ru(dcb)_2(NCS)_2/MO_2$ thin films.[91-92] The fully deprotonated compound, $(TBA)_4[Ru(dcb)_2(NCS)_2]$, is therefore a better model for the surface behavior than is *cis*-$Ru(dcbH_2)_2(NCS)_2$. The key difference in excited-state relaxation observed in solution relative to the metal oxide surfaces was that there was no evidence for ligand field population at the oxide interfaces. Presumably, relaxation through the ligand field states had a much larger barrier for the metal oxide surface than it did in fluid solution. Indeed, previous studies have shown that entrapment of $Ru(bpy)_3^{2+}$ in zeolites and polymers also resulted in an increased activation energy for LF state population.[25-26,30-31,73,93] Population of the LF states results in an elongation of metal-ligand bonds that is restricted by the metal oxide surface. As a result, the excited states are expected to be more stable toward photochemical ligand loss when anchored to a TiO_2 nanocrystallite.

In this regard, it is of interest to compare excited-state relaxation pathways of $(TBA)_4[Ru(dcb)_2(NCS)_2]$ with $Ru(dcb)_2(NCS)_2/TiO_2$ in acetonitrile solution. The fraction of excited states that decay through each pathway are shown as a function of temperature in Figure 2.10.[5,68] In fluid solution at +67 °C, excited state relaxation occurs with equal probability through the thexi, fourth MLCT, and LF states. In contrast, at the same temperature, 13% decay through the thexi state with 87% through the fourth MLCT state for $Ru(dcb)_2(NCS)_2/TiO_2$.

Consistent with this model, steady-state photolysis at the MLCT maximum showed very different behavior for the sensitizer in fluid solution and anchored to TiO_2 thin films at +70°C. Photolysis of *cis*-$Ru(dcb)_2(NCS)_2^{4-}$ in CH_3CN at +70°C led to spectral changes consistent with ligand loss photochemistry. In contrast, excitation of $Ru(dcb)_2(NCS)_2/TiO_2$ under the same conditions of temperature and solvent gave no evidence for photochemistry.

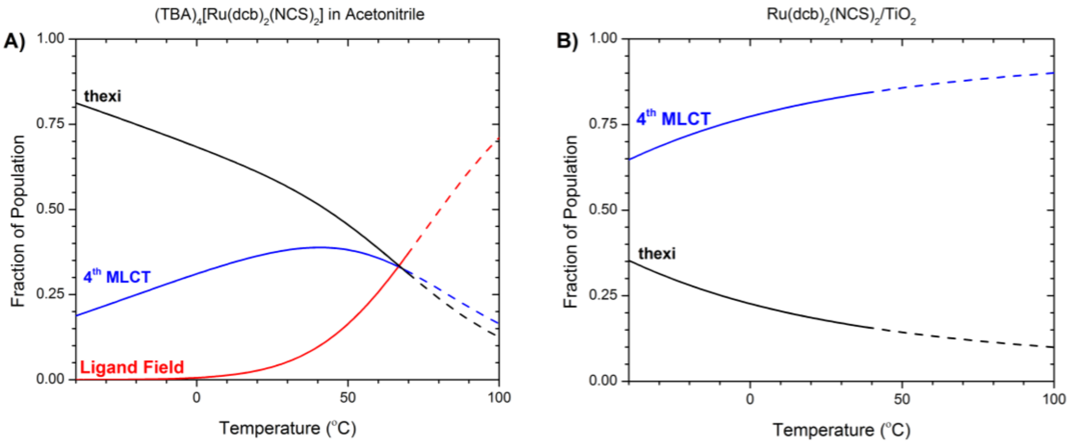

Figure 2.10. The fraction of excited states that relax through the thexi (black), 4th MLCT (blue), and LF (red) states as a function of temperature for (a) *cis*-$Ru(dcb)_2(NCS)_2^{4-}$ in CH_3CN and (b) $Ru(dcb)_2(NCS)_2/TiO_2$ thin film immersed in CH_3CN. The dashed lines are predictions based on the experimental data from lower temperatures shown as solid lines

2.5 Conclusion

The temperature-dependent lifetime data of *cis*-Ru(bpy)$_2$(CN)$_2$ and *cis*-Ru(bpy)$_2$(NCS)$_2$ were well described by an Arrhenius model from which activation energies of 810 cm^{-1} and pre-exponential factors of ~10^8 s^{-1} were abstracted. By analogy to previously reported data for MLCT excited states, these activational parameters were attributed to population of a higher lying "fourth" MLCT excited state. Notably absent was the expected population of antibonding ligand field states for *cis*-Ru(bpy)$_2$(NCS)$_2$, behavior that was attributed to π–bonding into the NCS$^-$ ligand and partial charge transfer from the NCS$^-$ to the metal center in the excited state. The inductive influence of substituents in the 4 and 4' positions of the bpy ligands was also quantified. The introduction of electron-withdrawing carboxylic acid groups in *cis*-Ru(dcbH$_2$)$_2$(NCS)$_2$ increased the energy gap between the thexi and LF states. Carboxylate groups in *cis*-Ru(dcb)$_2$(NCS)$_2^{4-}$ resulted in excited states that relaxed through the fourth MLCT and LF states. Excited state relaxation of the compound anchored to TiO$_2$, Ru(dcb)$_2$(NCS)$_2$/TiO$_2$, was through the thexi and fourth MLCT states without evidence for thexi → LF state internal conversion. Therefore, the temperature-dependent lifetime data predicted that Ru(dcb)$_2$(NCS)$_2$/TiO$_2$ would be stable with regard to ligand loss photochemistry, a prediction that was supported by photolysis experiments at +70°C. This finding is also consistent with previous studies that attributed ligand loss photochemistry of Ru(dcb)$_2$(NCS)$_2$/TiO$_2$ to the oxidized form of the compound[94-96] which has long been known to be reactive.[97]

2.6 References

(1) O'Donnell, R. M.; Johansson, P. G.; Abrahamsson, M.; Meyer, G. J. *Inorg. Chem.* **2013,** *52*, 6839-6848.

(2) Hager, G. D.; Crosby, G. A. *J. Am. Chem. Soc.* **1975,** *97*, 7031-7037.

(3) Hager, G. D.; Watts, R. J.; Crosby, G. A. *J. Am. Chem. Soc.* **1975,** *97*, 7037-7042.

(4) Crosby, G. A.; Demas, J. N. *J. Am. Chem. Soc.* **1971,** *93*, 2841-2847.

(5) Lumpkin, R. S.; Kober, E. M.; Worl, L. A.; Murtaza, Z.; Meyer, T. J. *J. Phys. Chem.* **1990,** *94*, 239-243.

(6) Sykora, M.; Kincaid, J. R. *Inorg. Chem.* **1995,** *34*, 5852-5856.

(7) Alary, F.; Heully, J. L.; Bijeire, L.; Vicendo, P. *Inorg. Chem.* **2007,** *46*, 3154-3165.

(8) Harriman, A.; Izzet, G. *Phys. Chem. Chem. Phys.* **2007,** *9*, 944-948.

(9) Demas, J. N.; Taylor, D. G. *Inorg. Chem.* **1979,** *18*, 3177-3179.

(10) Demas, J. N.; Crosby, G. A. *J. Mol. Spectrosc.* **1968,** *26*, 72-77.

(11) Crosby, G. A.; Hipps, K. W.; Elfring, W. H. *J. Am. Chem. Soc.* **1974,** *96*, 629-630.

(12) Fan, J.; Tysoe, S.; Strekas, T. C.; Gafney, H. D.; Serpone, N.; Lawless, D. *J. Am. Chem. Soc.* **1994,** *116*, 5343-5351.

(13) Pinnick, D. V.; Durham, B. *Inorg. Chem.* **1984,** *23*, 1440-1445.

(14) Pinnick, D. V.; Durham, B. *Inorg. Chem.* **1984,** *23*, 3841-3842.

(15) Wright, D. W.; Schmehl, R. H. *Inorg. Chem.* **1990,** *29*, 155-157.

(16) Wacholtz, W. M.; Auerbach, R. A.; Schmehl, R. H.; Ollino, M.; Cherry, W. R. *Inorg. Chem.* **1985,** *24*, 1758-1760.

(17) Reveco, P.; Schmehl, R. H.; Cherry, W. R.; Fronczek, F. R.; Selbin, J. *Inorg. Chem.* **1985,** *24*, 4078-4082.

(18) Henderson, L. J.; Cherry, W. R. *Chem. Phys. Lett.* **1985,** *114*, 553-556.

(19) Chaisson, D. A.; Hintze, R. E.; Stuermer, D. H.; Petersen, J. D.; McDonald, D. P.; Ford, P. C. *J. Am. Chem. Soc.* **1972,** *94*, 6665-6673.

(20) Malouf, G.; Ford, P. C. *J. Am. Chem. Soc.* **1977,** *99*, 7213-7221.

(21) Carlos, R. M.; Neumann, M. G.; Tfouni, E. *Inorg. Chem.* **1996,** *35*, 2229-2234.

(22) Singh, T. N.; Turro, C. *Inorg. Chem.* **2004,** *43*, 7260-7262.

(23) Allsopp, S. R.; Cox, A.; Kemp, T. J.; Reed, W. J. *J. Chem. Soc., Faraday Trans.* **1978,** *74*, 1275-1289.

(24) Masschelein, A.; Mesmaeker, A. K.-D.; Willsher, C. J.; Wilkinson, F. *J. Chem. Soc., Faraday Trans.* **1991,** *87*, 259-267.

(25) Maruszewski, K.; Strommen, D. P.; Kincaid, J. R. *J. Am. Chem. Soc.* **1993,** *115*, 8345-8350.

(26) Maruszewski, K.; Kincaid, J. R. *Inorg. Chem.* **1995,** *34*, 2002-2006.

(27) Kitamura, N.; Sato, M.; Kim, H.-B.; Obata, R.; Tazuke, S. *Inorganic Chemistry* **1988,** *27*, 651-658.

(28) Kober, E. M.; Sullivan, B. P.; Meyer, T. J. *Inorg. Chem.* **1984,** *23*, 2098-2104.

(29) Chen, P.; Meyer, T. J. *Chem. Rev.* **1998,** *98*, 1439-1478.

(30) Thompson, D. W.; Fleming, C. N.; Myron, B. D.; Meyer, T. J. *J. Phys. Chem. B* **2007,** *111*, 6930-6941.

(31) Calvert, J. M.; Meyer, T. J. *Inorg. Chem.* **1982,** *21*, 3978-3989.

(32) Barigelletti, F.; Juris, A.; Balzani, V.; Belser, P.; Von Zelewsky, A. *J. Phys. Chem.* **1987,** *91*, 1095-1098.

(33) Nazeeruddin, M. K.; Kay, A.; Rodicio, I.; Humphry-Baker, R.; Mueller, E.; Liska, P.; Vlachopoulos, N.; Grätzel, M. *J. Am. Chem. Soc.* **1993,** *115*, 6382-6390.

(34) Ardo, S.; Meyer, G. J. *Chem. Soc. Rev.* **2009,** *38*, 115-164.

(35) Grätzel, M. *Acc. Chem. Res.* **2009,** *42*, 1788-1798.

(36) Grätzel, M. *Inorg. Chem.* **2005,** *44*, 6841-6851.

(37) Hannappel, T.; Burfeindt, B.; Storck, W.; Willig, F. *J. Phys. Chem. B* **1997,** *101*, 6799-6802.

(38) Kallioinen, J.; Benkö, G.; Myllyperkiö, P.; Khriachtchev, L.; Skårman, B.; Wallenberg, R.; Tuomikoski, M.; Korppi-Tommola, J.; Sundström, V.; Yartsev, A. P. *J. Phys. Chem. B* **2004,** *108*, 6365-6373.

(39) Benkö, G.; Kallioinen, J.; Myllyperkiö, P.; Trif, F.; Korppi-Tommola, J. E. I.; Yartsev, A. P.; Sundström, V. *J. Phys. Chem. B* **2004,** *108*, 2862-2867.

(40) Benkö, G.; Kallioinen, J.; Korppi-Tommola, J. E. I.; Yartsev, A. P.; Sundström, V. *J. Am. Chem. Soc.* **2001,** *124*, 489-493.

(41) Kuciauskas, D.; Monat, J. E.; Villahermosa, R.; Gray, H. B.; Lewis, N. S.; McCusker, J. K. *J. Phys. Chem. B* **2002,** *106*, 9347-9358.

(42) Smeigh, A. L.; Katz, J. E.; Brunschwig, B. S.; Lewis, N. S.; McCusker, J. K. *J. Phys. Chem. C* **2008,** *112*, 12065-12068.

(43) Listorti, A.; O'Regan, B.; Durrant, J. R. *Chem. Mater.* **2011,** *23*, 3381-3399.

(44) Asbury, J. B.; Anderson, N. A.; Hao, E.; Ai, X.; Lian, T. *J. Phys. Chem. B* **2003,** *107*, 7376-7386.

(45) Enright, B.; Redmond, G.; Fitzmaurice, D. *J. Phys. Chem.* **1994,** *98*, 6195-6200.

(46) Lyon, L. A.; Hupp, J. T. *J. Phys. Chem. B* **1999,** *103*, 4623-4628.

(47) Clark, W. D. K.; Sutin, N. *J. Am. Chem. Soc.* **1977,** *99*, 4676-4682.

(48) Qu, P.; Thompson, D. W.; Meyer, G. J. *Langmuir* **2000,** *16*, 4662-4671.

(49) Farzad, F.; Thompson, D. W.; Kelly, C. A.; Meyer, G. J. *J. Am. Chem. Soc.* **1999,** *121*, 5577-5578.

(50) Higgins, G. T.; Bergeron, B. V.; Hasselmann, G. M.; Farzad, F.; Meyer, G. J. *J. Phys. Chem. B* **2006,** *110*, 2598-2605.

(51) Ardo, S.; Meyer, G. J. *J. Am. Chem. Soc.* **2011,** *133*, 15384-15396.

(52) Kelly, C. A.; Farzad, F.; Thompson, D. W.; Meyer, G. J. *Langmuir* **1999,** *15*, 731-737.

(53) Koops, S. E.; Durrant, J. R. *Inorg. Chim. Acta* **2008,** *361*, 663-670.

(54) Heimer, T. A.; Meyer, G. J. *J. Lumin.* **1996,** *70*, 468-478.

(55) Vinodgopal, K.; Hua, X.; Dahlgren, R. L.; Lappin, A. G.; Patterson, L. K.; Kamat, P. V. *J. Phys. Chem.* **1995,** *99*, 10883-10889.

(56) Fessenden, R. W.; Kamat, P. V. *J. Phys. Chem.* **1995,** *99*, 12902-12906.

(57) Nazeeruddin, M. K.; Zakeeruddin, S. M.; Humphry-Baker, R.; Jirousek, M.; Liska, P.; Vlachopoulos, N.; Shklover, V.; Fischer, C.-H.; Grätzel, M. *Inorg. Chem.* **1999,** *38*, 6298-6305.

(58) Heimer, T. A.; D'Arcangelis, S. T.; Farzad, F.; Stipkala, J. M.; Meyer, G. J. *Inorg. Chem.* **1996,** *35*, 5319-5324.

(59) Crosby, G. A.; Demas, J. N. *J. Phys. Chem.* **1971,** *75*, 991-1024.

(60) Kober, E. M.; Caspar, J. V.; Lumpkin, R. S.; Meyer, T. J. *J. Phys. Chem.* **1986,** *90*, 3722-3734.

(61) Herber, R. H.; Nan, G.; Potenza, J. A.; Schugar, H. J.; Bino, A. *Inorg. Chem.* **1989,** *28*, 938-942.

(62) Wajda, S.; Rachlewicz, K. *Inorg. Chim. Acta* **1978,** *31*, 35-40.

(63) Kohle, O.; Ruile, S.; Grätzel, M. *Inorg. Chem.* **1996,** *35*, 4779-4787.

(64) Zakeeruddin, S. M.; Nazeeruddin, M. K.; Humphry-Baker, R.; Grätzel, M. *Inorg. Chim. Acta* **1999,** *296*, 250-253.

(65) Wacholtz, W. F.; Auerbach, R. A.; Schmehl, R. H. *Inorg. Chem.* **1986,** *25*, 227-234.

(66) Abrahamsson, M.; Becker, H.-C.; Hammarström, L.; Bonnefous, C.; Chamchoumis, C.; Thummel, R. P. *Inorg. Chem.* **2007,** *46*, 10354-10364.

(67) Abrahamsson, M.; Wolpher, H.; Johansson, O.; Larsson, J.; Kritikos, M.; Eriksson, L.; Norrby, P.-O.; Bergquist, J.; Sun, L.; Åkermark, B.; Hammarström, L. *Inorg. Chem.* **2005,** *44*, 3215-3225.

(68) Forster, L. S. *Coord. Chem. Rev.* **2002,** *227*, 59-92.

(69) Cherry, W. R.; Henderson, L. J. *Inorg. Chem.* **1984,** *23*, 983-986.

(70) Miessler, G. L.; Tarr, D. A. *Inorganic Chemistry*. 4th ed.; Prentice Hall: Upper Saddle River, New Jersey, 2011.

(71) Durham, B.; Walsh, J. L.; Carter, C. L.; Meyer, T. J. *Inorg. Chem.* **1980,** *19*, 860-865.

(72) Rillema, D. P.; Blanton, C. B.; Shaver, R. J.; Jackman, D. C.; Boldaji, M.; Bundy, S.; Worl, L. A.; Meyer, T. J. *Inorg. Chem.* **1992,** *31*, 1600-1606.

(73) Adelt, M.; Devenney, M.; Meyer, T. J.; Thompson, D. W.; Treadway, J. A. *Inorg. Chem.* **1998,** *37*, 2616-2617.

(74) Burmeister, J. *Coord. Chem. Rev.* **1990,** *105*, 77-133.

(75) Norbury, A. H. *J. Chem. Soc.* **1971**, 1089-1091.

(76) Asbury, J. B.; Ellingson, R. J.; Ghosh, H. N.; Ferrere, S.; Nozik, A. J.; Lian, T. *J. Phys. Chem. B* **1999,** *103*, 3110-3119.

(77) Kämper, S.; Paretzki, A.; Fiedler, J.; Záliš, S.; Kaim, W. *Inorg. Chem.* **2012,** *51*, 2097-2104.

(78) Shklover, V.; Nazeeruddin, M. K.; Zakeeruddin, S. M.; Barbé, C.; Kay, A.; Haibach, T.; Steurer, W.; Hermann, R.; Nissen, H. U.; Grätzel, M. *Chem. Mater.* **1997,** *9*, 430-439.

(79) Shklover, V.; Ovchinnikov, Y. E.; Braginsky, L. S.; Zakeeruddin, S. M.; Grätzel, M. *Chem. Mater.* **1998,** *10*, 2533-2541.

(80) Tuikka, M.; Hirva, P.; Rissanen, K.; Korppi-Tommola, J.; Haukka, M. *Chem. Comm.* **2011,** *47*, 4499-4501.

(81) Meyer, T. J. *pac* **1986,** *58*, 1193.

(82) Guillemoles, J.-F.; Barone, V.; Joubert, L.; Adamo, C. *J. Phys. Chem. A* **2002,** *106*, 11354-11360.

(83) Nazeeruddin, M. K.; De Angelis, F.; Fantacci, S.; Selloni, A.; Viscardi, G.; Liska, P.; Ito, S.; Takeru, B.; Grätzel, M. *J. Am. Chem. Soc.* **2005,** *127*, 16835-16847.

(84) Rensmo, H.; Södergren, S.; Patthey, L.; Westermark, K.; Vayssieres, L.; Kohle, O.; Brühwiler, P. A.; Hagfeldt, A.; Siegbahn, H. *Chem. Phys. Lett.* **1997,** *274*, 51-57.

(85) Fantacci, S.; De Angelis, F. *Coord. Chem. Rev.* **2011,** *255*, 2704-2726.

(86) Wolfbauer, G.; Bond, A. M.; Deacon, G. B.; MacFarlane, D. R.; Spiccia, L. *J. Am. Chem. Soc.* **1999,** *122*, 130-142.

(87) Zhang, X.; Smolentsev, G.; Guo, J.; Attenkofer, K.; Kurtz, C.; Jennings, G.; Lockard, J. V.; Stickrath, A. B.; Chen, L. X. *J. Phys. Chem. Lett.* **2011,** *2*, 628-632.

(88) Shoute, L. C. T.; Loppnow, G. R. *J. Am. Chem. Soc.* **2003,** *125*, 15636-15646.

(89) Kelly, C. A.; Farzad, F.; Thompson, D. W.; Stipkala, J. M.; Meyer, G. J. *Langmuir* **1999,** *15*, 7047-7054.

(90) Qu, P.; Meyer, G. J. *Langmuir* **2001,** *17*, 6720-6728.

(91) Finnie, K. S.; Bartlett, J. R.; Woolfrey, J. L. *Langmuir* **1998,** *14*, 2744-2749.

(92) Nazeeruddin, M. K.; Humphry-Baker, R.; Liska, P.; Grätzel, M. *J. Phys. Chem. B* **2003,** *107*, 8981-8987.

(93) Vaidyalingam, A.; Dutta, P. K. *Anal. Chem.* **2000,** *72*, 5219-5224.

(94) Nour-Mohhamadi, F.; Nguyen, S. D.; Boschloo, G.; Hagfeldt, A.; Lund, T. *J. Phys. Chem. B* **2005,** *109*, 22413-22419.

(95) Nguyen, H. T.; Ta, H. M.; Lund, T. *Sol. Energy Mater. and Sol. Cells* **2007,** *91*, 1934-1942.

(96) Andersen, A. R.; Halme, J.; Lund, T.; Asghar, M. I.; Nguyen, P. T.; Miettunen, K.; Kemppainen, E.; Albrektsen, O. *J. Phys. Chem. C* **2011,** *115*, 15598-15606.

(97) Das, S.; Kamat, P. V. *J. Phys. Chem. B* **1998,** *102*, 8954-8957.

Chapter 3. Electric Fields and Charge Screening in Dye Sensitized Mesoporous Nanocrystalline TiO_2 Thin Films

In part a compilation of two publications.[1-2]

This work was collaborative in conjunction with Shane Ardo, [†] *Renato N. Sampaio,*[†‡] *and Timothy J. Barr*[†]

[†]*Johns Hopkins University, Baltimore, Maryland*

[‡]*Federal University of Uberlândia, Uberlândia, Brazil*

3.1 Introduction

Charge transfer processes that occur at semiconductor-electrolyte interfaces are essential to the function of many technologies including organic light-emitting diodes (OLEDs),[3] organic photovoltaics (OPVs),[4-5] dye-sensitized solar cells (DSSCs),[6-7] and dye-sensitized photoelectrosynthesis cells (DSPECs).[8] Since electric fields affect any process or electronic transition that involves the movement of charge, it is worthwhile to gain an understanding of the interfacial electric fields present in these devices.

The 1991 Nature paper by Grätzel and O'Regan introduced the clever idea of utilizing mesoporous thin films of nanocrystalline TiO_2 in photoelectrochemical cells.[9] The idea turned out to be revolutionary and created whole new fields of science based on energy conversion with nanometer-sized semiconductor materials.[10-11] The nanometer length scale can result in very different photoelectrochemical behavior than that observed in bulk semiconductor materials. For example, in single crystal and thin film materials, electron-hole pairs are efficiently separated by a surface electric field (the 'depletion' or 'space charge' region) that is absent in weakly doped semiconductor nanocrystallites.[12] In fact, the three bias conditions identified for single crystal semiconductor materials, i.e. depletion, inversion, and accumulation, are not particularly useful for quantifying or modelling the photoelectrochemistry of semiconductor nanocrystallites. In the case of dye-sensitized solar cells (DSSCs), it has generally been assumed that any electric fields that might be present under steady-state illumination would be quantitatively "screened" from the surface anchored dye molecules by the large dielectric constant of TiO_2, $\varepsilon_r = 7 – 50$;[13] the high permittivity of acetonitrile, $\varepsilon_r = 37$;[14] and the half molar ionic strength.[15-16] Furthermore, it was thought that the reorganization of interfacial ions and solvent molecules would also screen photo-injected electrons under non-equilibrium conditions.

The assumption of quantitative charge screening at sensitized TiO_2 interfaces was proven to be incorrect in 2010, when Ardo *et al.* and Cappel *et al.* reported that electrons injected into TiO_2 had a profound influence on the absorption spectrum of dye molecules anchored to the surface.[17-18] The absorption changes measured after the injection of charge were similar to those previously reported in traditional Stark spectroscopic measurements,[19-22] but were unidirectional due to the fixed orientation of the molecular dipole moment relative to the TiO_2 surface. Therefore, their data provided compelling evidence for Stark effects, electroabsorption changes, at sensitized TiO_2 interfaces.

3.1.1 Traditional Stark Spectroscopy

Traditional Stark (electroabsorption) spectroscopy was pioneered by Boxer for both electronic and vibrational transitions of chemical systems in the 1980s and 1990s.[23-24] The two characteristic parameters measured experimentally include the change in polarizability, $\Delta\alpha$, and the change in dipole moment, $\Delta\mu$, between the ground and excited states. Determination of $\Delta\alpha$ for a compound provides insight into the sensitivity of the corresponding transition to an external electric field. For example, $\Delta\alpha$ can be used to probe the local environment surrounding a molecule in biological systems.[25-26] Although $\Delta\alpha$ can be significant for some systems, $\Delta\mu$ generally constitutes the largest component of experimentally observed Stark signals. This is particularly true for $Ru(bpy)_3^{2+}$ since the ground state has no net dipole where the MLCT excited state, $[Ru^{III}(bpy^-)(bpy)_2]^{2+*}$, has a significant dipole moment of ~12 D. The $\Delta\mu$ value is directly related to distance, *r*, by Equation (3.1):

$$\Delta\mu = e\,r \tag{3.1}$$

where *e* is the unit charge.[23-24,27-28] Theoretical treatments of electroabsorption spectroscopy formulated by Liptay[29] have been widely applied to experimental data and extended to inorganic compounds by Reimers and Hush.[30]

Traditional electroabsorption spectroscopy experiments immobilize randomly oriented samples either in frozen solvent glasses or polymer thin films sandwiched between two parallel, optically transparent electrodes spaced 10 – 100 μm apart, Figure 3.1. The absorption change of the sample is then monitored using lock-in amplification techniques during the sinusoidal application of a large voltage, typically 0 – 10 kV. These applied voltages and sample thicknesses result in electric fields on the order of 1 MV/cm prior to dielectric breakdown.[23-24]

The measured electroabsorption spectra are subsequently interpreted in terms of a lineshape analysis using the Liptay treatment in order to quantify the parameters of interest. Possible lineshapes resulting from application of a uni-directional, applied electric field, F_z, on a chromophore are shown in Figure 3.2 for various orientations of $\Delta\mu$ with respect to F_z. In the absence of an applied electric field, there would be no perturbation to an electronic transition and this reference case is indicated by the gray lines. Application of an electric field oriented anti-parallel to $\Delta\mu$ of a chromophore would result in a blue-shift of the absorption spectrum compared to the reference case and would be observed experimentally as a first-derivative lineshape, blue lines in Figure 3.2. The opposite case, where $\Delta\mu$ is collinear with the electric field, would result in a red-shift of the absorption spectrum and also appear experimentally as a first-derivative lineshape but of different sign, red lines in Figure 3.2. However, it is experimentally difficult to align each molecule and isotropically oriented samples are used almost exclusively. The random orientation of $\Delta\mu$ with respect to the applied field is illustrated by the purple circle in Figure 3.2 and the observed electroabsorption spectra is effectively a sum of the other three cases. Therefore, second-derivative-type lineshapes are typically observed in traditional electroabsorption spectroscopy.[23-24,27-28]

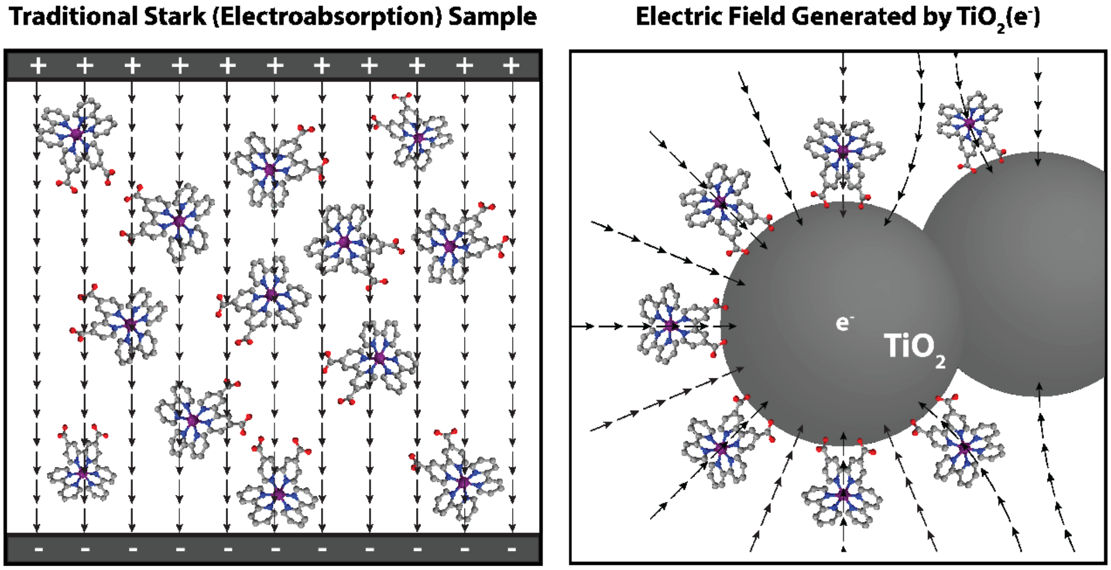

Figure 3.1. Depiction of external electric field applied across parallel electrodes in a traditional sample for Stark spectroscopy (left) compared to the interfacial electric fields generated by electrons injected into titanium dioxide nanocrystallites found in DSSCs (right).

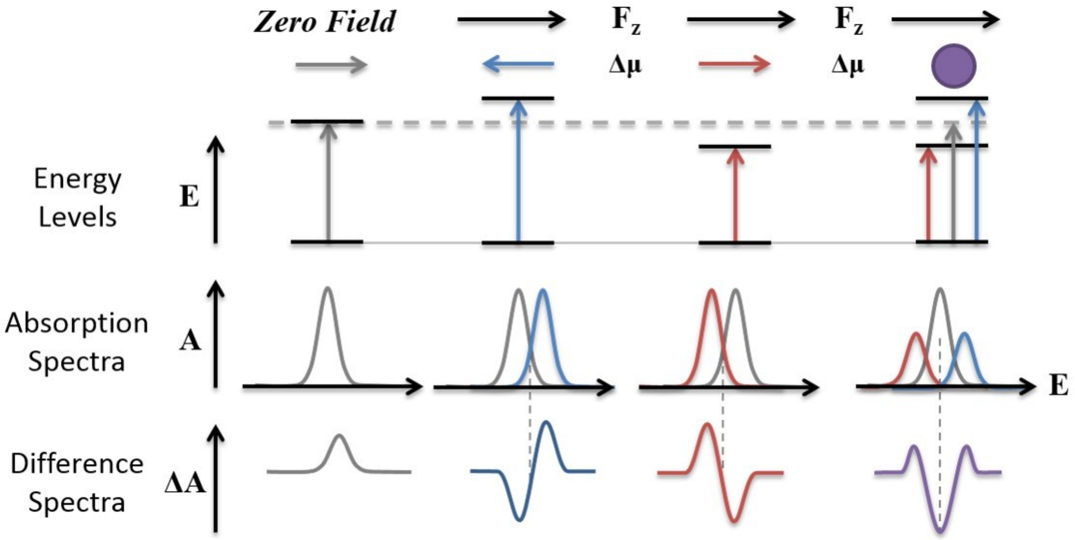

Figure 3.2. Depiction of difference spectra lineshapes resulting from the application of an electric field acting upon a compound. See text for a more detailed description.

Initial measurements on ruthenium polypyridyl compounds determined the extent of electron localization in their metal-to-ligand charge transfer (MLCT) and ligand-to-metal charge transfer (LMCT) excited states. Boxer and Oh measured $\Delta\mu = 8.8$ D for the 454 nm MLCT transition of $[\mathrm{Ru^{II}(bpy)_3}]^{2+}$, a value corresponding to 65% of full charge transfer from the Ru(II) center to the bpy ligand. Discrepancy from 100% charge transfer character was attributed to electron polarization in the excited state.[19] Experiments on related mononuclear ruthenium polypyridyl compounds yielded $\Delta\mu$ values spanning 1 to 11 D.[19,31-32] Electroabsorption spectroscopy has only been performed on a very small number of ruthenium polypyridyl compounds to date, but the evidence provided supports complete localization of the electron on a single ligand.

Electroabsorption measurements were used to determine interfacial electron transfer distances of sensitized TiO_2 nanocrystallites dispersed as colloids. Stark emission spectroscopy was used by Hupp and co-workers in 2002 to differentiate between electron injection from either locally excited or interfacial charge transfer states of eosin Y and Coumarin-343 attached to TiO_2. Their system also allowed for determination of a back electron transfer distance of 3.9 eÅ that was attributed to an electron transfer from a localized TiO_2 trap state to the oxidized dye molecule as opposed to the TiO_2 conduction band.[33] Brunschwig and co-workers provided further support for the involvement of TiO_2 trap states during electron transfer studies of TiO_2 nanocrystallites sensitized with $\mathrm{M(CN)}_n^{4-}$ compounds ($\mathrm{M} = \mathrm{Ru^{II}}, \mathrm{Fe^{II}}$ for $n = 4$; $\mathrm{M} = \mathrm{Mo^{IV}}, \mathrm{W^{IV}}$ for $n = 6$), which form metal-to-particle charge transfer (MPCT) complexes. Experimentally determined charge transfer distances of 4.1 - 5.3 eÅ were independent of the TiO_2 nanocrystallite diameter over a range of 2 to 20 nm.[34-35] More recently, Zdyb and Krawczyk have examined small organic molecules attached to TiO_2 nanocrystallites that exhibit direct charge transfer absorption properties. A new band appears at 438 nm in the absorption spectrum of catechol after attachment to TiO_2 which is associated with $\Delta\mu = 15.7$ D. Although the size of the nanocrystallites were not reported, the $\Delta\mu$ for catechol yields a short charge transfer distance of 2.9 eÅ.[36] Electroabsorption spectroscopy of anthracene-9-carboxylic acid adsorbed onto TiO_2 was performed in acidic and basic aqueous solutions. The measured $\Delta\mu$ changed from 2 – 3 D under basic conditions and increased to 7 – 10 D in acidic solutions. The difference in $\Delta\mu$ was attributed to pH dependent binding modes of anthracene-9-carboxylic acid and differences in their electron injection efficiency.[37] Taken together, these results indicate that direct charge injection from the metal center localizes on an acceptor orbital (i.e. trap state) located on a single or a few Ti(IV) centers located near the point of attachment and does not delocalize into the conduction band.

The data highlighted above illustrate the use of traditional electroabsorption measurements for description of the MLCT states of ruthenium polypyridyl compounds. Furthermore, determination of $\Delta\mu$ for colloidal TiO_2 suspensions provides a physical description of the molecular entities involved in electron transfer reactions at sensitized-TiO_2 interfaces.

3.1.2 Electric Fields Generated at the Sensitized TiO_2 Interfaces

The initial reports of a Stark effect present at sensitized TiO_2 interfaces by Ardo *et al.* and Cappel *et al.* were based on analogy to the traditional electroabsorption spectroscopy data.[17] In the work by Ardo *et al.*, a large, first-derivative lineshape was observed for ruthenium polypyridyl compounds following excited state electron injection on mesoporous, nanocrystalline TiO_2 thin film samples. With some assumptions, the spectral shifts reported directly on the magnitude of the electric field that was found to be substantial, on the order of 2.7 MV/cm. It was determined that injected electrons generate an electric field that emanates from the TiO_2 nanocrystallites normal to the surface, Figure 3.1. Co-sensitization of TiO_2 thin films with different ruthenium polypyridyl compounds allowed for selective excitation of one compound and showed that compounds not associated with excited-state injection also exhibited spectral shifts. Although the Stark effect was observed immediately after pulsed laser excitation, < 10 ns, during transient absorption experiments, the electric field was rapidly screened by solvent molecules and the electrolyte, termed interfacial ionic reorganization. Spectroelectrochemical studies performed under steady-state conditions in the presence of high ionic-strength electrolyte solutions exhibited difference spectra comparable to those observed during transient measurements.[17]

Complementary work by Cappel *et al.* provided evidence for the Stark effect at sensitized TiO_2 using two organic sensitizers. In order to determine the electroabsorption properties of the organic sensitizers, a modified electroabsorption apparatus was built. Instead of using a traditional, randomly oriented sample, a monolayer of sensitizer was adsorbed onto dense, planar TiO_2 fabricated on a conductive glass substrate. Application of an external electric field resulted in a first-derivative lineshape in the electroabsorption spectra consistent with alignment of the sensitizers at the TiO_2 surface. The observed value of $\Delta\mu = 1$ D was small compared to the theoretical value of 7.1 D obtained from time-dependent density functional theory (TD-DFT) calculations. The deviation was attributed to a small angle between the surface and the molecules that oriented them almost parallel to the surface. The authors noted that the Δμ value could be smaller than expected if the TiO_2 surface was not perfectly flat. The photoinduced absorption spectra (PIA) of the indoline D149 dye attached to TiO_2 thin films under solar cell conditions was similar to the electroabsorption spectra.[18]

One important concern raised by these studies was the idea that the electroabsorption changes generated by interfacial electric fields can influence the interpretation of kinetic data obtained from transient absorption spectroscopy. Spectral signatures of the Stark effect have been observed following electron injection from ruthenium polypyridyl compounds into conductive Sn-doped In_2O_3 (ITO) nanoparticles;[38] for ruthenium polypyridyl compounds anchored to TiO_2 through phosphonate linkages in aqueous solution;[39] and in solid-state DSSCs (ssDSSCs) using triarylamine-substituted perylene monoimides, fullerenes, or acenequinones as organic sensitizers.[40-42] Using the spectroscopic Stark signal associated with organic sensitizers attached to metal oxide thin films, Lenzer and co-workers were able to determine the time scale for interfacial electric field generation. Following ultrafast electron injection, <250 fs, of the organic indoline dye D149 on ZnO and TiO_2 thin films, a non-instantaneous Stark signal was observed for injected electrons and oxidized sensitizer. In fact, the Stark signature actually increased in intensity following pulsed excitation which was attributed to the build-up of a local electric field and characterized by a time constant of ~20 ps.[43] Similar results were observed for the triarylamine-based D35 and E6 sensitizers which displayed biphasic growth of the Stark effect characterized by 0.2 and 12 ps time constants.[44-45] The transient increase of the Stark signal was attributed to reorientational motion of the sensitizers in response to the interfacial electric field and non-uniform alignment of the sensitizers on the surface.

Diffusion of electrons from surface trap states into the bulk was invoked to explain the decay of the Stark signal occurred on the ns timescale prior to charge recombination.

3.1.3 Future Directions and the Impact of Lewis Acidic Cations

It remains unclear whether surface electric fields or charge screening is relevant to power conversion in DSSCs. The spectral shift of the dye molecules is generally small and does not appreciably change the light harvesting efficiency of the sensitized thin film. Likewise, the potential drop experienced by the dye molecules represents a fairly small value of ~ 40 mV that corresponds to only about 5% of the open circuit photovoltages reported for gold standard DSSCs.[17] In fact, charge screening may have a deleterious influence on energy conversion efficiencies with anionic redox mediators like I^-/I_3^-. Synonymous to increasing the width of the space-charge layer in bulk semiconductor solar cells, increasing the Debye length for charge screening at the semiconductor electrolyte interface should aid in the generation of even further spatially separated and longer-lived anionic charges, *i.e.* $TiO_2(e^-)$s and I_3^-, and hence improve solar conversion efficiencies. While speculative, fundamental studies of surface electric fields and charge screening may provide new insights into the fabrication of superior DSSCs. Such studies are also of intellectual interest in their own right.

An intriguing observation from previous research was that following pulsed laser excitation of sensitized TiO_2 thin films immersed in an acetonitrile electrolyte, the magnitude of the Stark effect decreased over time periods in which the $TiO_2(e^-)$ concentration was constant. This behavior was attributed to the reorganization of interfacial ions and solvent molecules responding to photo-injected $TiO_2(e^-)$s and to diffusion of electrons away from the TiO_2 surface after injection.[17,43-46] While screening of this type is well known in the electrochemical and photo-electrochemical literature,[15-16,47-50] this chapter presents the first measurements to probe the dynamics of this process on short time scales. It was found that the kinetics for charge screening were sensitive to whether Mg^{2+} or Li^+ cations were present in the electrolyte, see the Appendix to this chapter.[51] The study of $[Ru(dtb)_2(dcb)](PF_6)_2$, where dtb is 4,4′-(*tert*-butyl)$_2$-2,2′-bipyridine and dcb is 4,4′-$(CO_2H)_2$-2,2′-bipyridine, was utilized as the compound is a particularly sensitive probe of the surface electric field, Figure 3.3. In this chapter the charge screening studies were expanded to include Na^+ and Ca^{2+}. The inclusion of these ions influenced the screening dynamics as well as the interfacial density of states and the excited state injection yield.

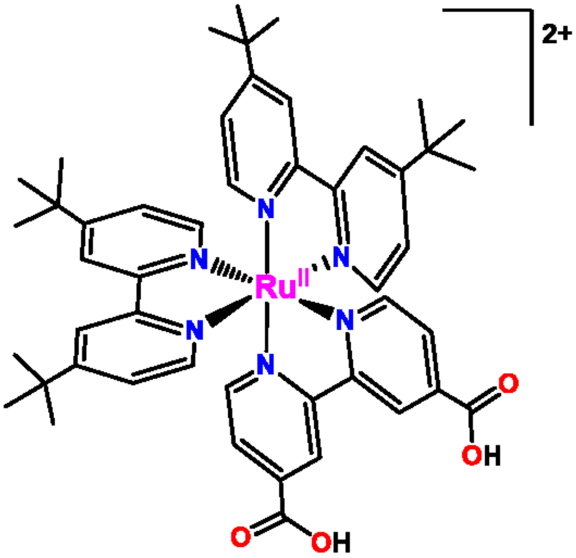

Figure 3.3. The structure of $Ru(dtb)_2(dcb)^{2+}$.

3.2 Experimental

3.2.1 Materials.

The following reagents and substrates were used as received from the indicated commercial suppliers: acetonitrile (CH_3CN; Burdick & Jackson, spectrophotometric grade); deionized water; lithium perchlorate ($LiClO_4$; Sigma-Aldrich 99.99%); sodium perchlorate ($NaClO_4$; Sigma-Aldrich, 99%); magnesium perchlorate ($Mg(ClO_4)_2$; Sigma-Aldrich, ACS Reagent); calcium perchlorate tetrahydrate ($Ca(ClO_4)_2{\cdot}4H_2O$; Sigma-Aldrich, 99%); tetra-*n*-butylammonium perchlorate ($TBAClO_4$; Aldrich, ≥99.0%); tetra-*n*-butylammonium iodide (TBAI; Fluka, ≥99.0%); argon gas (Airgas, >99.998%); oxygen gas (Airgas, industrial grade); titanium(IV) isopropoxide (Sigma-Aldrich, 97%); fluorine-doped SnO_2-coated glass (FTO; Hartford Glass Co., Inc., 2.3 mm thick, 15Ω/□); and glass microscope slides (Fisher Scientific, 1mm thick). $[Ru(dtb)_2(dcb)](PF_6)_2$ was available from previous studies.[17]

3.2.2 Preparations.

Transparent TiO_2 nanocrystallites (anatase, ~15 nm in diameter) were prepared by acid hydrolysis of $Ti(i\text{-}OPr)_4$ using a sol-gel method previously described in the literature.[52] The sols were cast as transparent mesoporous thin films by doctor blading onto glass microscope slides for spectroscopic measurements and transparent FTO conductive substrates for electrochemical measurements with the aid of transparent cellophane tape as a mask and spacer (~10 μm thick). The films were sintered at 450 ºC for 30 minutes under an atmosphere of O_2 flow and either used immediately or stored in an oven for future use. Sensitization was achieved by immersing the thin films in acetonitrile sensitizer solutions (mM concentrations) for hours to days depending on the desired surface coverage. Unless otherwise noted, the thin films were sensitized to roughly maximum surface coverage, $\Gamma \sim 7 \times 10^{-8}$ mol/cm^2, which was determined using a modified Beer-Lambert law, Equation (3.2),[53]

$$\text{Abs} = 1000 \times \Gamma \times \varepsilon \tag{3.2}$$

where ε is the molar decadic extinction (absorption) coefficient (16,400 $M^{-1}cm^{-1}$ at 465 nm) that was assumed to have the same value when anchored to the surface. Sensitized films were soaked in neat acetonitrile for at least one hour prior to experimentation.

3.2.3 Spectroscopy.

UV-Visible Absorption. Steady-state UV-Visible absorption spectra were obtained on a Varian Cary 50 or an Agilent Cary 60 spectrophotometer at room temperature in 1.0 cm path length quartz cuvettes. Sensitized TiO_2 thin films were positioned at a 45° angle in cuvettes filled with the indicated acetonitrile solutions. The solutions were purged with argon gas for a minimum of 30 min prior to transient absorption and spectroelectrochemical studies.

Photoluminescence. Steady-state photoluminescence (PL) spectra were obtained with a Spex Fluorolog spectrophotometer equipped with a 450 W Xe lamp for the excitation source. PL spectra of sensitized thin films were obtained under ambient conditions at room temperature with excitation 45° to the surface and detection from the front face of the sample. Quenching experiments were performed by obtaining the PL spectrum of the sensitized thin film in neat solvent and after replacement of the neat solvent with the electrolyte solution of interest.

Transient Absorption. Nanosecond transient absorption measurements were obtained with an apparatus similar to that which has been previously described in the literature.[54] Briefly, samples were excited by a Q-switched, pulsed Nd:YAG laser (Quantel USA (BigSky) Brilliant B; 5-6 ns full width at half-maximum (fwhm), 1 Hz, ~10 mm in diameter) tuned to 532 nm with the appropriate nonlinear optics. The excitation fluence was measured by a thermopile power meter (Molectron) and was typically 1-5 mJ/pulse so that the absorbed fluence was typically <1 mJ/pulse. A 150 W xenon arc lamp served as the probe beam and was aligned orthogonal to the laser excitation light. The lamp was pulsed with 100 V for detection at sub-100 microsecond time scales. Detection was achieved with a monochromator (Spex 1702/04) optically coupled to an R928 photomultiplier tube (Hamamatsu). Appropriate glass filters were positioned between the probe lamp/sample and the sample/detection monochromator. Transient data was acquired with a computer-interfaced digital oscilloscope (LeCroy 9450, Dual 350 MHz) with an overall instrument response time of ~10 ns. Typically, 30 laser pulses were averaged at each observation wavelength over the range 400 – 750 nm, at 3 or 5 nm intervals. Full spectra were generated by averaging 2-10 points on either side of the desired time value to reduce noise in the raw data. For single wavelength measurements, 90-180 laser pulses were typically averaged to achieve satisfactory signal-to-noise ratios. Relative excited-state electron injection yields were measured by comparative actinometry on the nanosecond time scale for samples in different metal cation solutions using lithium as the reference.[55-56]

3.2.4 Electrochemistry.

A potentiostat (Bioanalytical Scientific Instruments, Inc. (BAS) model CV-50W or EC Epsilon electrochemical analyzer) was employed for electrochemical measurements in a standard three-electrode arrangement with a TiO_2 thin film working electrode, a Pt gauze counter electrode (BAS), and a non-aqueous silver reference electrode (BAS). The ferrocenium/ferrocene ($Fc^{+/0}$) half-wave potential was measured both before and after experiments in a 100 mM $TBAClO_4$/acetonitrile electrolyte that was used as an external standard to calibrate the reference electrode. All potentials are reported versus the normal hydrogen electrode (NHE) through the use of a conversion constant of -630 mV from NHE to $Fc^{+/0}$ in acetonitrile at 25 ºC.[57]

Spectroelectrochemistry was conducted via simultaneous application of an applied potential while monitoring the UV-vis absorption spectra of TiO_2 thin-film electrodes in the indicated electrolytes. Each applied potential was held for 2-3 min, until the absorbance in the 700-900 nm region became invariant in time. Single-wavelength absorption features plotted as a function of the applied potential were proportional to the cumulative formation/loss of states; for the $TiO_2(e^-)$ absorption features, this was directly related to the cumulative TiO_2 density of acceptor states.[58]

Spectroelectrochemical charge extraction measurements were performed on un-sensitized TiO_2 thin films to obtain the extinction coefficient of the $TiO_2(e^-)$s. In these experiments, the absorbance at 700 nm was recorded as the potential was stepped from +200 mV to increasingly negative values. The charge present in the film was measured coulometrically after stepping the potential back to the original +200 mV value. [59-61] The absorption values were corrected for the 45º angle of the thin film in relation to the optical path. Each charge extraction cycle was repeated 3 times at each monitored wavelength.

3.2.5 Data Analysis

Kinetic data fitting and spectral modeling were performed in Origin 9.0 with least-squares error minimization accomplished using the Levenberg-Marquardt iteration method.

3.3 Results

Thin films of TiO_2 on glass substrates were reacted with $Ru(dtb)_2(dcb)^{2+}$, abbreviated $Ru(dtb)_2(dcb)/TiO_2$, in acetonitrile solutions to a maximum surface coverage, $\Gamma \sim 7 \times 10^{-8}$ M^{-1} cm^2.[17] Representative absorption spectra of $Ru(dtb)_2(dcb)/TiO_2$ immersed in neat acetonitrile and 100 mM perchlorate acetonitrile solutions are shown in Figure 3.4.A. The $Ru(dtb)_2(dcb)/TiO_2$ samples exhibit a metal-to-ligand charge transfer (MLCT) absorption band centered at 465 nm in neat acetonitrile and the fundamental TiO_2 absorption below 380 nm. The spectrum measured in neat acetonitrile and in 100 mM $TBAClO_4$ (where TBA is tetra-*n*-butylammonium) were, within experimental error, the same. Replacement of the neat acetonitrile solvent bath with 100 mM metal perchlorate salt acetonitrile electrolytes resulted in a bathochromic shift, the magnitude of which was dependent on the cation. The MLCT absorption shifts to ~480 nm for monovalent cations, Li^+ and Na^+, and to ~486 nm for divalent cations, Mg^{2+} and Ca^{2+}, shown in Figure 3.4.A.

Visible light excitation of the MLCT absorption band resulted in room temperature photoluminescence (PL), shown in Figure 3.4.B. In neat acetonitrile, $Ru(dtb)_2(dcb)/TiO_2$ exhibited a PL maximum at 665 nm. Upon replacement of the neat solvent with 100 mM metal perchlorate electrolytes: the PL maximum red-shifted and the PL intensity was quenched to varying extents dependent on the nature of the cation. The corresponding quantities are compiled in Table 3.1.

Electrochemical reduction of un-sensitized TiO_2 thin films resulted in a blue shift of the fundamental absorption and the appearance of a broad absorption in the visible region. When measured as difference spectra, the blue shift of the fundamental absorption appears as a bleach, the magnitude of which was sensitive to the identity of the cation, Figure 3.5. Charge extraction experiments were performed on un-sensitized TiO_2 thin films to determine the molar extinction coefficients of the $TiO_2(e^-)$ absorption band in each of the four metal perchlorate electrolytes. The absorption at 700 nm was monitored while the applied potential was stepped from 200 mV to -400 mV for 65 s and then was returned to the initial 200 mV potential, Figure 3.6. The absorption was corrected for the 45° angle of the thin film relative to the optical path. Plotting the corrected absorbance versus the extracted charge from the film allowed for determination of the molar extinction coefficient from the slope of a linear fit to the data, shown in Figure 3.7. The extinction coefficient was within experimental error independent of the electrolyte and determined to be $\varepsilon(TiO_2(e^-)) = 930 \pm 50\ M^{-1}cm^{-1}$. The application of more negative potentials, i.e. < -1.2 V, resulted in new absorption features that were not studied in detail due to irreversible absorption changes, Figure 3.8.

In order to understand the ground-state behavior, spectroelectrochemistry was performed on sensitized TiO_2 thin films in 100 mM metal perchlorate acetonitrile electrolytes. Application of a positive applied potential resulted in spectral changes consistent with the oxidation of Ru^{II} to Ru^{III}, shown in Figure 3.9. The equilibrium potential where the concentration of Ru^{II} and Ru^{III} were equal was taken as the $E°(Ru^{III/II})$ reduction potential for $Ru(dtb)_2(dcb)/TiO_2$. The spectroelectrochemical data were fit to Equation (3.3).

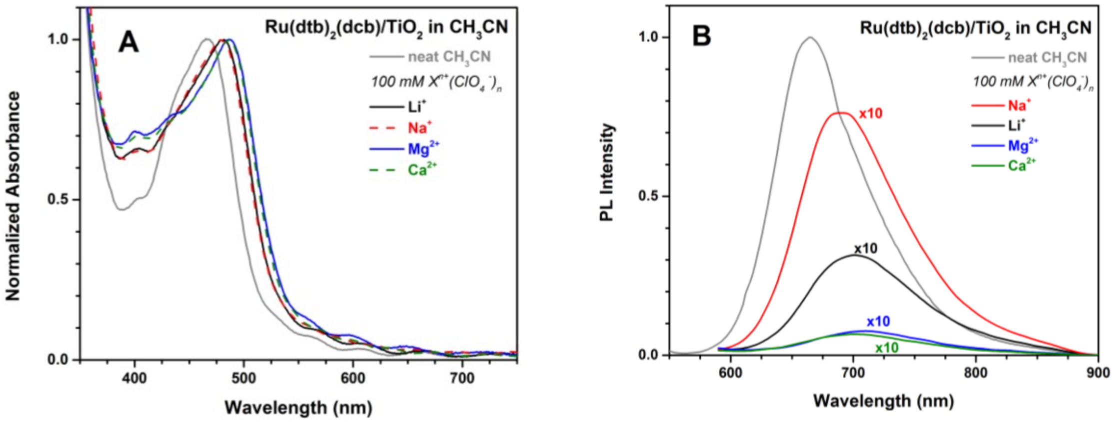

Figure 3.4. Steady-state UV-Vis absorbance (A) and photoluminescence (B) spectra of $Ru(dtb)_2(dcb)/TiO_2$ in neat acetonitrile and in the presence of 100 mM metal perchlorate electrolyte.

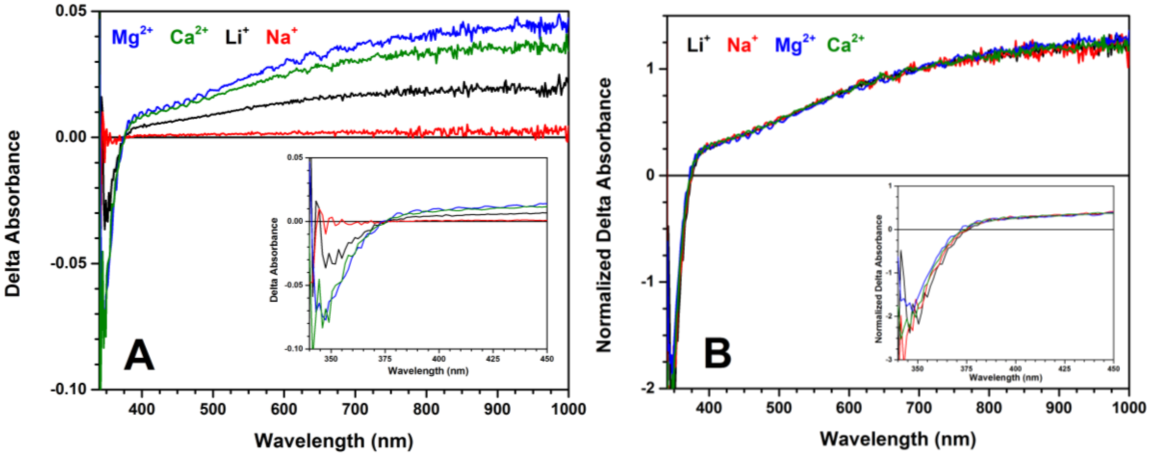

Figure 3.5. Difference spectra of un-sensitized TiO_2 thin films in 100 mM metal perchlorate acetonitrile solutions. (A) Spectra obtained with an applied bias of -400 mV vs. NHE. (B) Normalized spectra obtained at either -500 mV (Li^+, Mg^{2+}, and Ca^{2+}) or -800 mV (Na^+). The insets show close-ups of the 340 – 450 nm regions of the spectra.

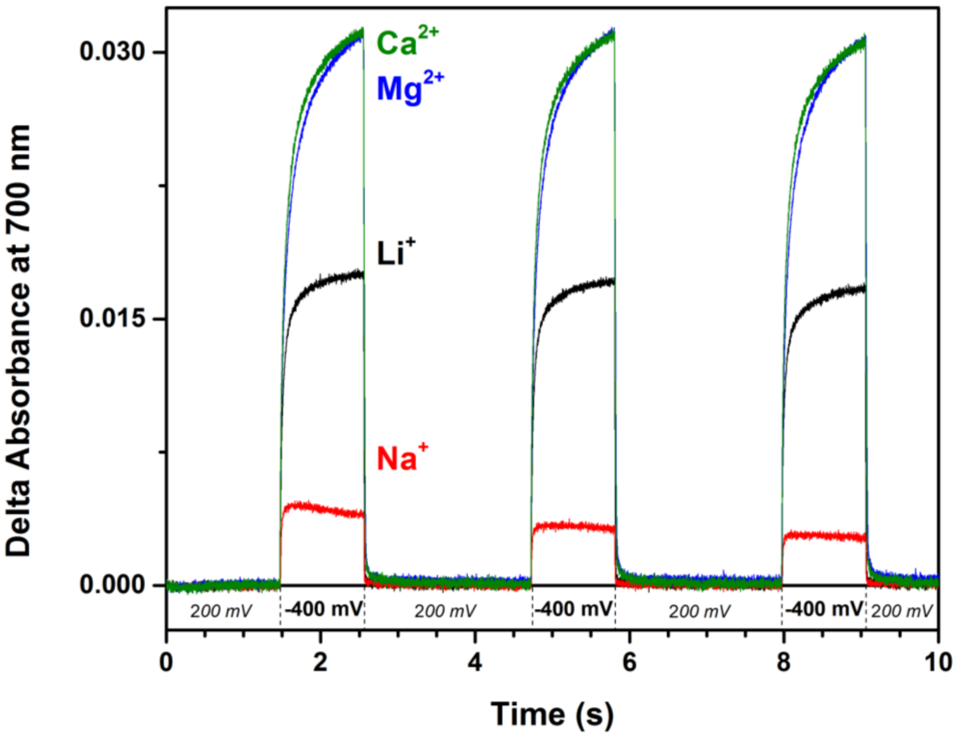

Figure 3.6. Representative spectroelectrochemical charge extraction data for un-sensitized TiO_2 in 100 mM metal perchlorate electrolytes. The change in absorbance at 700 nm was monitored with applied potentials of 200 and -400 mV vs. NHE.

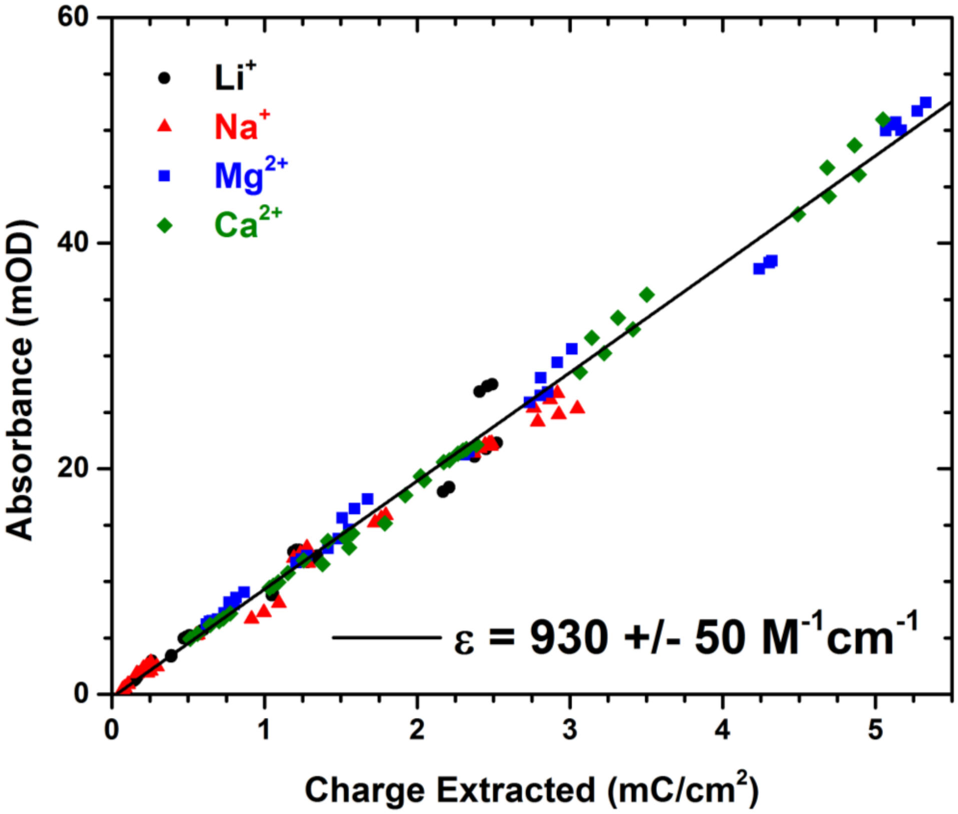

Figure 3.7. Absorbance as a function of the charge extracted from un-sensitized TiO_2 thin films immersed in 100 mM metal perchlorate acetonitrile solutions. The black line indicates the best fit to the data which yields a molar extinction coefficient of 930 ± 50 $M^{-1}cm^{-1}$.

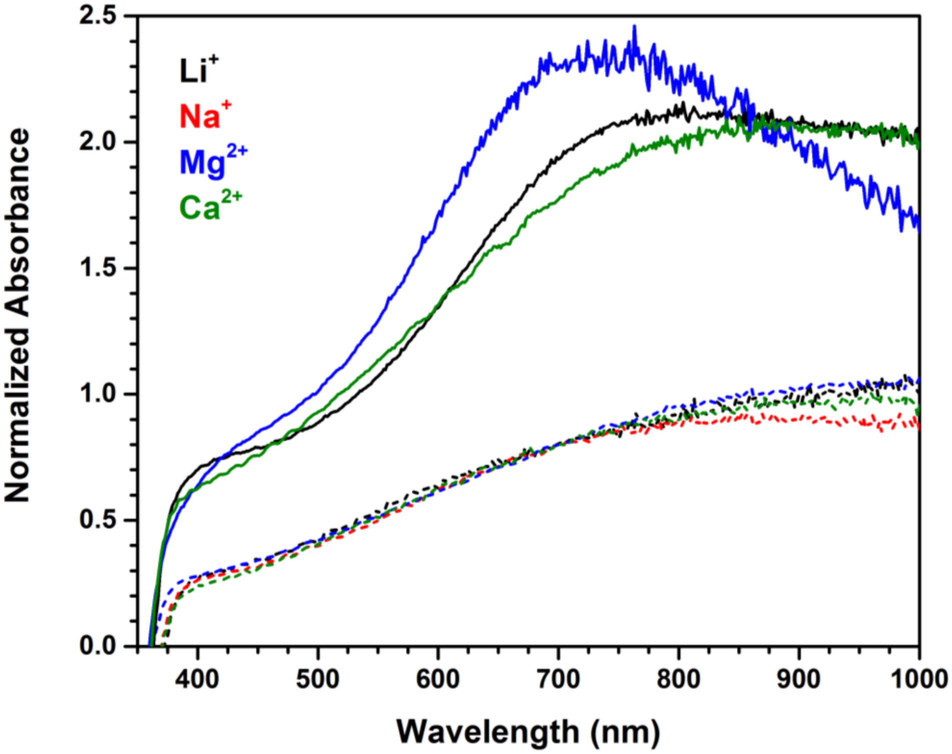

Figure 3.8. Absorbance spectra of un-sensitized TiO_2 thin films immersed in 100 mM metal perchlorate acetonitrile solutions with relatively small negative applied bias, > -1.2V, (dashed lines) and under strongly reducing conditions (solid lines).

Table 3.1. Photophysical and electrochemical properties of $Ru(dtb)_2(dcb)/TiO_2$ in 100 mM metal perchlorate acetonitrile solutions.

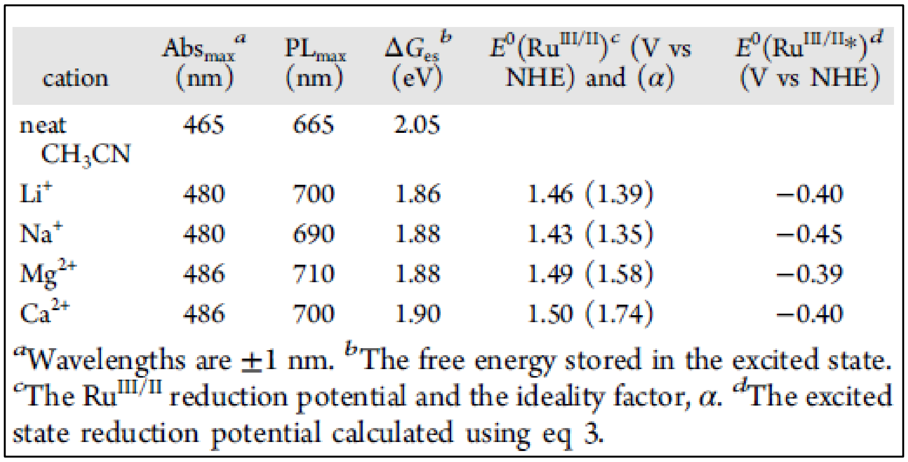

cation	Abs_{max}[a] (nm)	PL_{max} (nm)	ΔG_{es}[b] (eV)	$E^0(Ru^{III/II})$[c] (V vs NHE) and (α)	$E^0(Ru^{III/II*})$[d] (V vs NHE)
neat CH_3CN	465	665	2.05		
Li^+	480	700	1.86	1.46 (1.39)	−0.40
Na^+	480	690	1.88	1.43 (1.35)	−0.45
Mg^{2+}	486	710	1.88	1.49 (1.58)	−0.39
Ca^{2+}	486	700	1.90	1.50 (1.74)	−0.40

[a] Wavelengths are ±1 nm. [b] The free energy stored in the excited state. [c] The $Ru^{III/II}$ reduction potential and the ideality factor, α. [d] The excited state reduction potential calculated using eq 3.

$$x = \frac{1}{1 + 10\exp\left(\frac{E_{app} - E^0}{a \times 59\ mV}\right)} \tag{3.3}$$

where x is the fraction of molecules in each oxidation state, E_{app} is the applied potential, and α is the ideality factor. Knowledge of $E^o(\mathrm{Ru^{III/II}})$ allowed for the estimation of the reducing power of the excited state which was calculated through a free energy cycle using Equation (3.4):

$$E^0\left(\mathrm{Ru^{III/II*}}\right) = E^0\left(\mathrm{Ru^{III/II}}\right) - \Delta G_{ES} \tag{3.4}$$

where ΔG_{ES} is the Gibbs free energy stored in the MLCT excited state determined by a tangent line extrapolation back to zero intensity on the high energy side of the PL spectrum. The formal reduction potentials and ideality factors are summarized in Table 3.1.

Application of a forward (negative) bias resulted in reduction of TiO_2 that was monitored by the characteristic broad absorption features from 400 to 900 nm attributed to $TiO_2(e^-)$s. Concomitant with the $TiO_2(e^-)$ absorption, the MLCT absorption band blue-shifted. Both of these spectral features are evident in Figure 3.10 for a $Ru(dtb)_2(dcb)/TiO_2$ thin film in 100 mM $LiClO_4$ acetonitrile solution with an applied bias ranging from 150 to -750 mV vs. NHE. The normalized spectroelectrochemical absorption spectra are shown in Figure 3.10.A. and after subtraction of the contributions from $TiO_2(e^-)$s in Figure 3.10.B. Difference spectra of these same data are shown in Figure 3.10.C. and D.

The electric field experienced by the surface-bound sensitizers as a function of the applied potential bias was calculated using both peak-to-peak and first-derivative analysis methods and are compared in the insets of Figure 3.10.A. and B. For the peak-to-peak analysis, the electric field was calculated using Equation (3.5):

$$\Delta \upsilon = -\frac{|\Delta\vec{\mu}| \cdot |\vec{E}| \cdot \cos\theta}{100hc} \tag{3.5}$$

where h is Planck's constant, c is the speed of light in a vacuum, $\Delta \upsilon$ is the change in spectroscopic peak maximum (in wavenumbers), $\Delta\vec{\mu}$ is the change in dipole moment vector between the ground and excited state, $\vec{E}$ is the electric field vector, and θ is the angle between the latter two quantities. With the assumption of $\theta = 180^{\circ}$ and $\Delta\vec{\mu} = 4.75$ D,[19,46] the electric field can be calculated at each applied bias. Similarly, the first-derivative analysis was performed using Equation (3.6):

$$\Delta A = -\frac{dA}{d\nu}\frac{\Delta\vec{\mu}\vec{E}}{h} \tag{3.6}$$

where ΔA is the difference spectrum, or delta absorbance, and $\frac{dA}{d\nu}$ is the first derivative of the absorbance spectrum (in wavenumbers).[18] The electric field calculated using both the peak-to-peak analysis and the first-derivative analysis were in good agreement, as seen in the insets of Figure 3.10.A. and B.

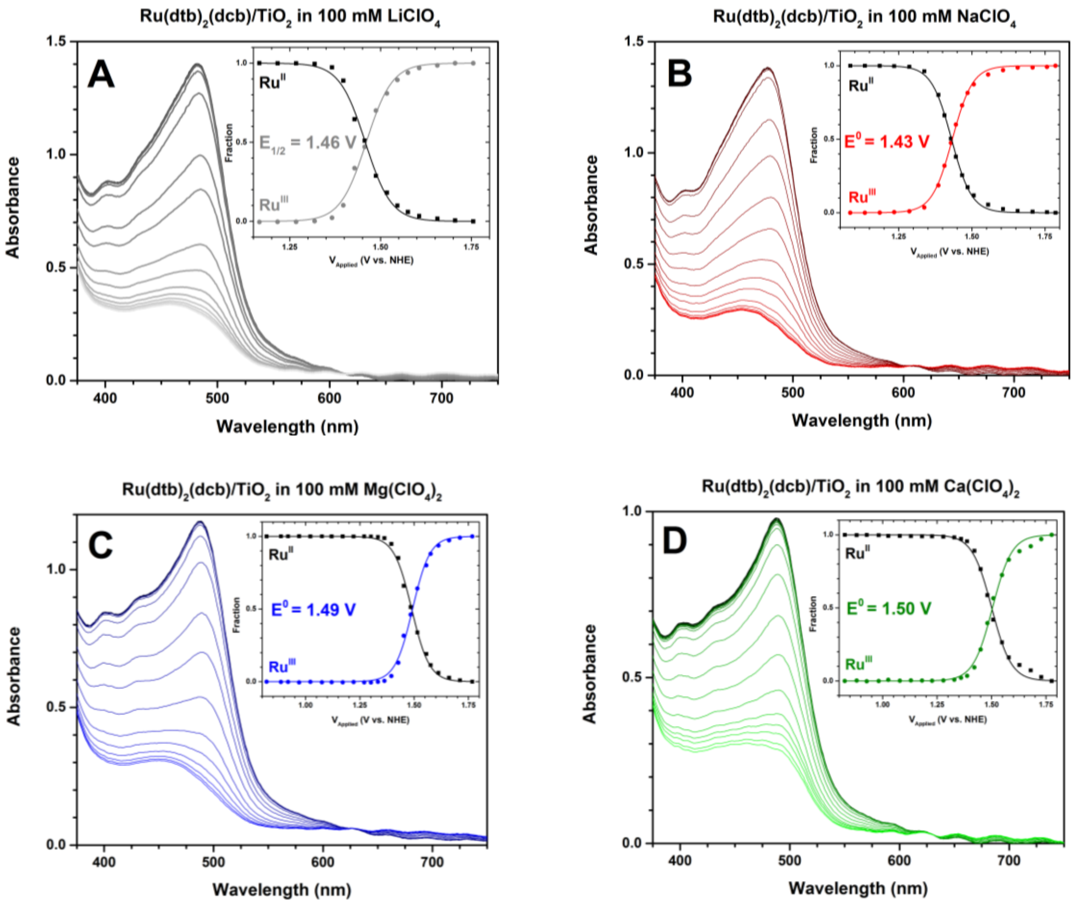

Figure 3.9. Spectroelectrochemical absorbance spectra of $Ru(dtb)_2(dcb)/TiO_2$ oxidation obtained in 100 mM electrolytes containing (A) Li^+, (B) Na^+, (C) Mg^{2+}, or (D) Ca^{2+}. Insets depict sigmoidal fits to the fraction of Ru^{II} (black squares) or Ru^{III} (colored circles) present where $E_{1/2}$ is given by the equilibrium potential where the fraction of both Ru^{II} and Ru^{III} were equal.

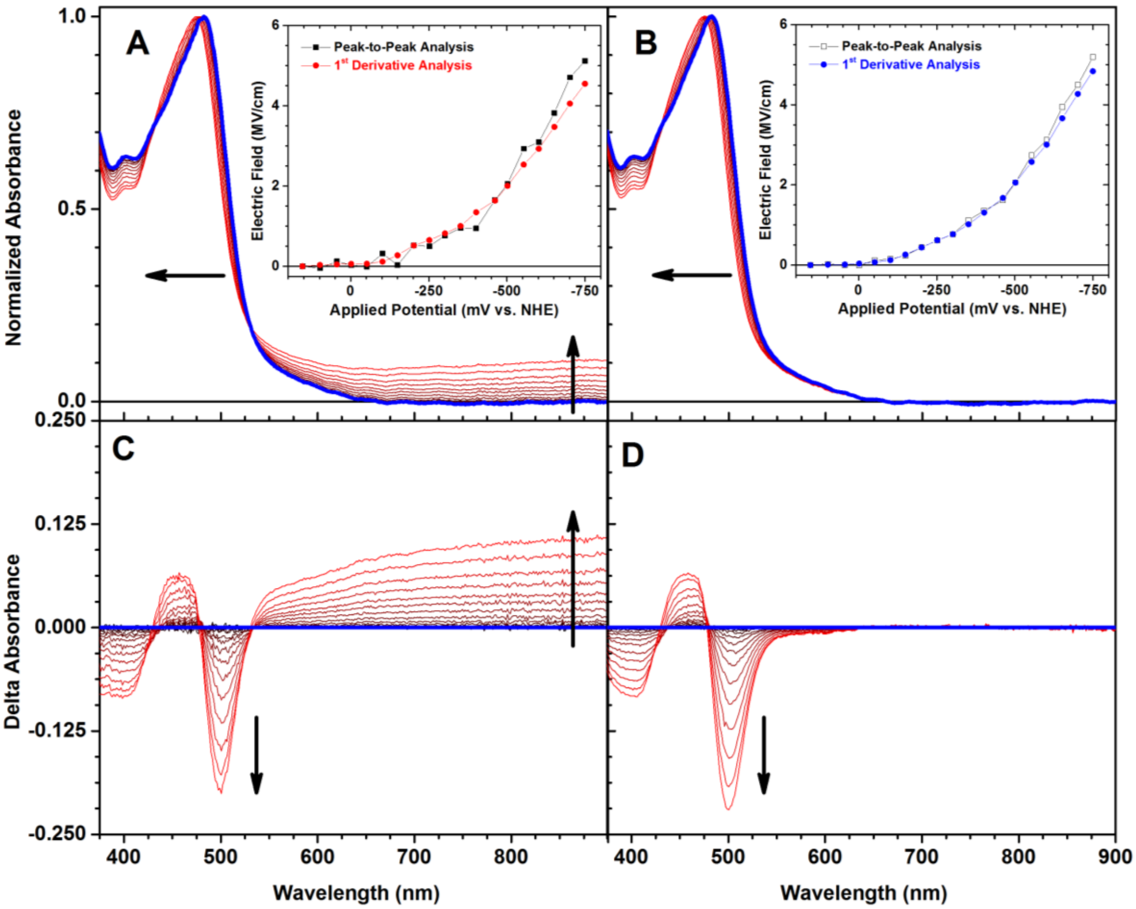

Figure 3.10. Spectra of a potentiostatically controlled Ru(dtb)$_2$(dcb)/TiO$_2$ film in 100 mM LiClO$_4$ acetonitrile solution (A); and after subtraction of the long-wavelength TiO$_2$(e$^-$) absorption (B). The difference spectra for the data shown in A and B are given in C and D, respectively. The insets in A and B indicate the electric field strength calculated by two different analyses. The spectra in dark blue were recorded at +150 mV and spectra recorded at more negative potentials (up to -750 mV) are indicated in red. The arrows indicate the direction of change with increased negative applied potential.

The electric field experienced by the surface-bound sensitizers was calculated using the electron corrected spectra and the first-derivative method for all four cations and is shown in Figure 3.11 as a function of the applied potential (A) and the estimated electron concentration per TiO_2 nanoparticle (B). The latter was calculated by converting the applied potential to the number of $TiO_2(e^-)$s per 15 nm diameter particle through the measured absorbance and Beer's law using the measured extinction coefficient and the effective optical path length for a 10 μm thick film of 50% porosity.[62] For example, in 100 mM metal perchlorate solution where ε = 930 cm^{-1}, an absorbance of 0.010 would correspond to 16 $TiO_2(e^-)$s/particle with Equation (3.7):

$$Abs = \varepsilon \times l \times c(TiO_2(e^-)) = 930\ (M^{-1}cm^{-1}) \times 14.14 \times 10^{-4}\ (cm) \times 50\% \times \frac{(TiO_2(e^-))}{{}^4\!/_3\pi\left(7.5\times10^{-9}\ (m)\right)^3 \times N_A \times 10^3 (L\, m^{-3})} \tag{3.7}$$

The relative injection yields were measured by comparative actinometry 100 ns after pulsed 532 nm light excitation of $Ru(dtb)_2(dcb)/TiO_2$ in 100 mM metal perchlorate acetonitrile solutions.[22] The yields were within experimental error unity for Li^+, Mg^{2+}, and Ca^{2+} and found to be 0.95 for Na^+.

Pulsed light excitation into the MLCT absorption band of $Ru(dtb)_2(dcb)/TiO_2$ thin films immersed in 100 mM metal perchlorate solutions with 250 mM of tetrabutylammonium iodide, present to regenerate the sensitizer, generated long-lived charge separated states, comprised of $TiO_2(e^-)$s and triiodide.

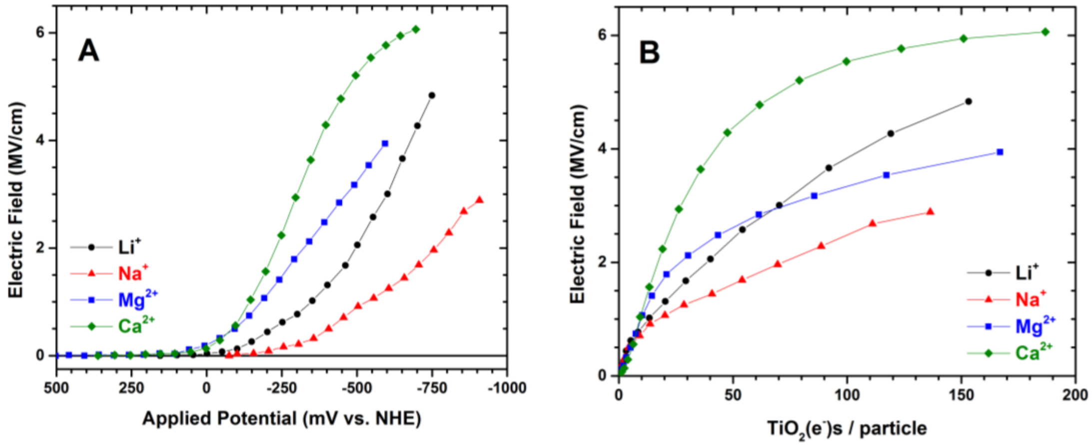

Figure 3.11. Electric field experienced by $Ru(dtb)_2(dcb)/TiO_2$ in acetonitrile solutions containing 100 mM Li^+, Na^+, Mg^{2+}, or Ca^{2+} as a function of: (A) the applied potential and (B) the number of $TiO_2(e^-)$s on a per particle basis.

Representative transient absorption spectra shown in Figure 3.12 were obtained 2.5 μs after laser excitation, a delay time chosen to ensure that all sensitizers had been regenerated and all iodide oxidation chemistry was complete. The transient absorption spectra exhibit: (1) small absorption features from 400 – 425 nm, attributed to formation of triiodide; (2) a first-derivative shaped feature centered around 485 nm, attributed to the $TiO_2(e^-)$-induced Stark effect; and (3) absorption from 600 – 750 nm, attributed to $TiO_2(e^-)$s. Care was taken to adjust the incident irradiance such that the long wavelength absorption measured 2.5 μs after the laser excitation was the same under all conditions, such that the number of $TiO_2(e^-)$s was constant. The transient absorption spectra were modeled with first-derivatives of the ground-state absorption spectra, shown in Figure 3.13, and the electric fields calculated using Equation (3.6) are collected in Table 3.2.

Single-wavelength absorption changes monitored at wavelengths characteristic for $TiO_2(e^-)$s and the Stark effect were quantified over seven orders of magnitude, from 100 ns to 1 s, shown in Figure 3.14. The observed kinetics were non-exponential, but well-modeled by the Kohlrausch-Williams-Watts (KWW) stretched exponential function, Equation (3.8):

$$I(t) = I_0 \exp[(-kt)^{\beta}] \tag{3.8}$$

where I_0 is the initial amplitude, k is a characteristic rate constant, and β is inversely proportional to the width of an underlying Lévy distribution of rate constants, $0 < \beta < 1$.[17,63] The data were fit with β fixed to a value of 0.2 and the abstracted rate constants were $k_{Li+, Na+} = 5 \times 10^4\ s^{-1}$ and $k_{Mg2+, Ca2+} = 5 \times 10^2\ s^{-1}$.

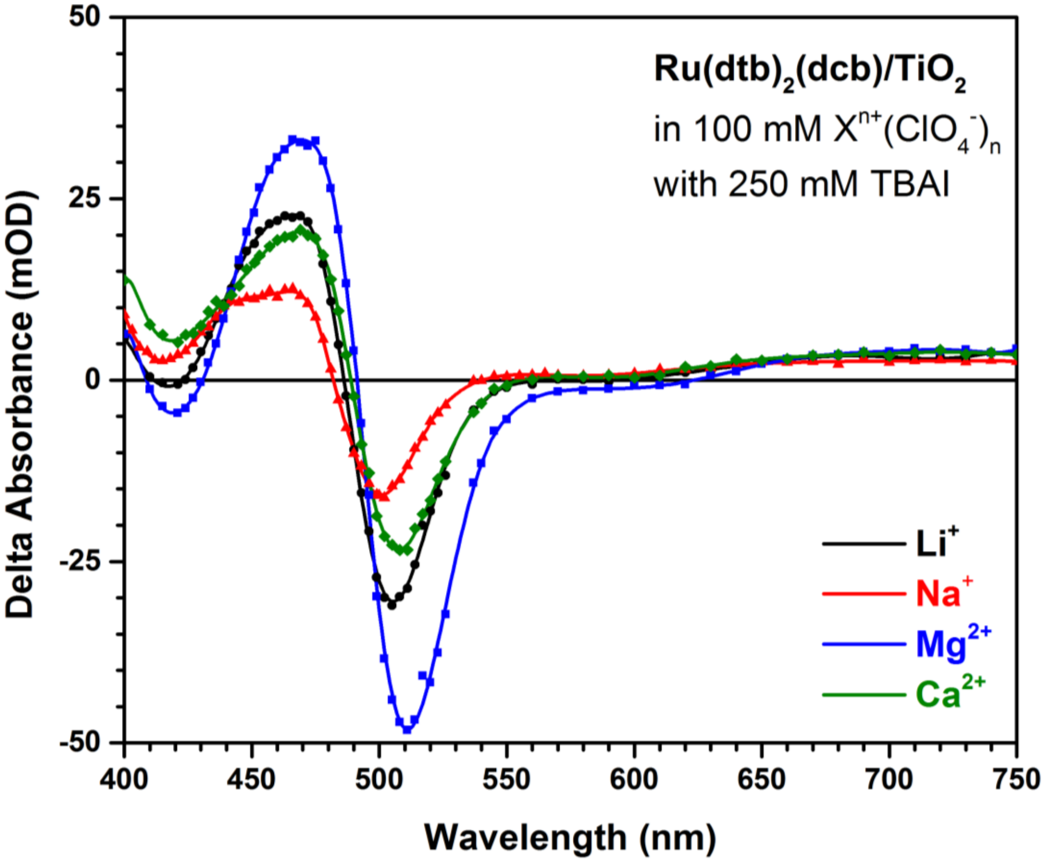

Figure 3.12. Transient absorption spectra obtained 2.5 μs after pulsed 532 nm excitation of Ru(dtb)$_2$(dcb)/TiO$_2$ in acetonitrile electrolyte solutions containing 100 mM of the indicated perchlorate salts and 250 mM tetra-*n*-butylammonium iodide.

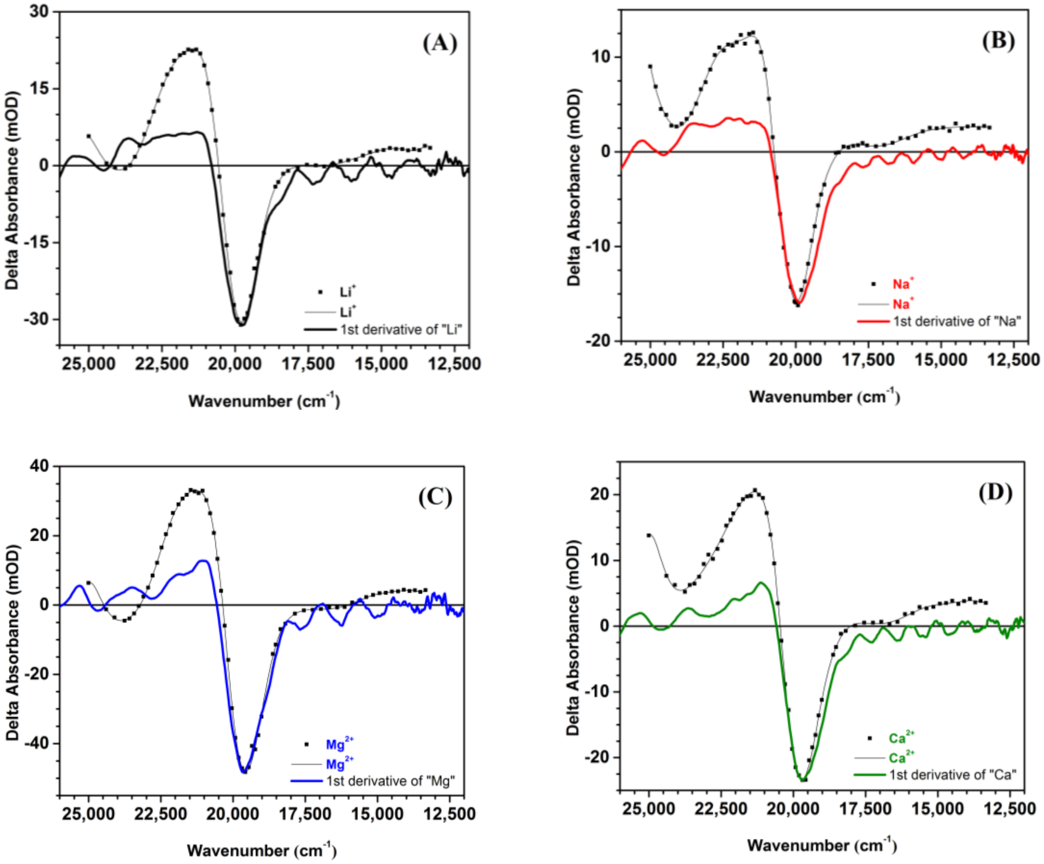

Figure 3.13. Transient absorption spectra of Ru(dtb)$_2$(dcb)/TiO$_2$ obtained 2.5 μs after 532 nm laser excitation immersed in 0.25 M TBAI with 0.1 M of A) LiClO$_4$, B) NaClO$_4$, C) Mg(ClO$_4$)$_2$, and D) Ca(ClO$_4$)$_2$. Overlaid are the corresponding, scaled first-derivatives of the ground-state absorption spectra.

Table 3.2. Ionic Radii, Spectral Shifts, and Electric Field Strength for Ru(dtb)$_2$(dcb)/TiO$_2$

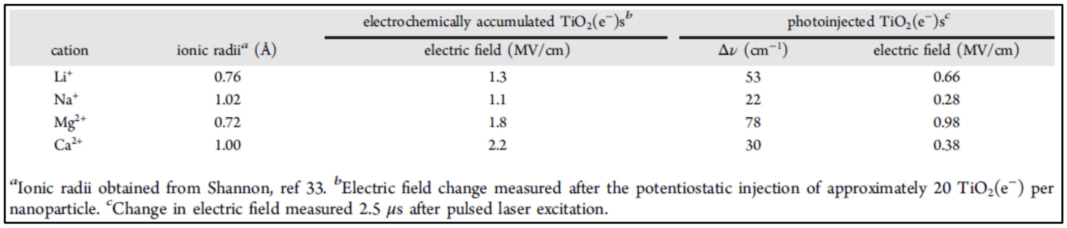

		electrochemically accumulated TiO$_2$(e$^-$)s[b]	photoinjected TiO$_2$(e$^-$)s[c]	
cation	ionic radii[a] (Å)	electric field (MV/cm)	$\Delta\nu$ (cm^{-1})	electric field (MV/cm)
Li$^+$	0.76	1.3	53	0.66
Na$^+$	1.02	1.1	22	0.28
Mg^{2+}	0.72	1.8	78	0.98
Ca^{2+}	1.00	2.2	30	0.38

[a] Ionic radii obtained from Shannon, ref 33. [b] Electric field change measured after the potentiostatic injection of approximately 20 TiO$_2$(e$^-$) per nanoparticle. [c] Change in electric field measured 2.5 μs after pulsed laser excitation.

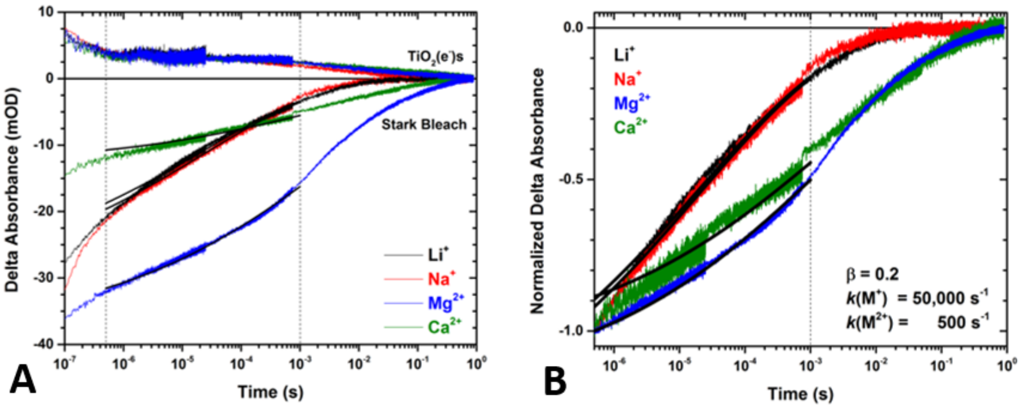

Figure 3.14. Single-wavelength transient absorption kinetic data of $Ru(dtb)_2(dcb)/TiO_2$ in acetonitrile electrolyte solutions containing 100 mM of the indicated perchlorate salts with 250 mM tetra-*n*-butylammonium iodide measured at 750 nm, primarily $TiO_2(e^-)$s, and ~500-510 nm, the maximum of the Stark effect bleach (A). The normalized kinetics for the Stark effect bleach are shown in (B). Overlaid in black are fits to the KWW function over the time period indicated by the dashed lines where the $TiO_2(e^-)$ concentration remained constant.

3.4 Discussion

The nature of the cations present in 100 mM acetonitrile electrolytes surrounding a Ru(dtb)$_2$(dcb)/TiO$_2$ sensitized thin film were varied to test whether they had an influence on the surface electric field and the dynamics of interfacial charge screening. This was indeed realized and both the kinetics and the electric field were found to be acutely sensitive to the nature of the cation. As is often found to be the case in studies of sensitized materials, the alteration of this one cation variable influenced many properties of the sensitized material including the absorption and photoluminescence spectra, ground state reduction potentials, and the excited state injection yields. The origin(s) of these spectral changes are described first followed by a description of the electric field strengths and charge screening behavior.

3.4.1 Cation Dependent Spectroelectrochemical Properties.

The adsorption of ions on semiconductor surfaces is known to have a strong influence on the valence and conduction band edge positions. A well-documented example for metal oxide semiconductors in aqueous solution is the 59 mV shift of the band edges that accompanies a factor of ten change in the proton concentration.[58,64-65] The surface adsorption of alkali and alkaline earth metal cations can have similar effects and are hence sometimes referred to as ‘potential determining ions’.[66-69] In general, cation adsorption shifts the band edge positions positive on an electrochemical scale away from the vacuum level. High efficiency dye-sensitized solar cells (DSSCs) utilize anatase TiO$_2$ in non-aqueous solvents, very often CH$_3$CN, where dramatic energetic shifts have been reported.

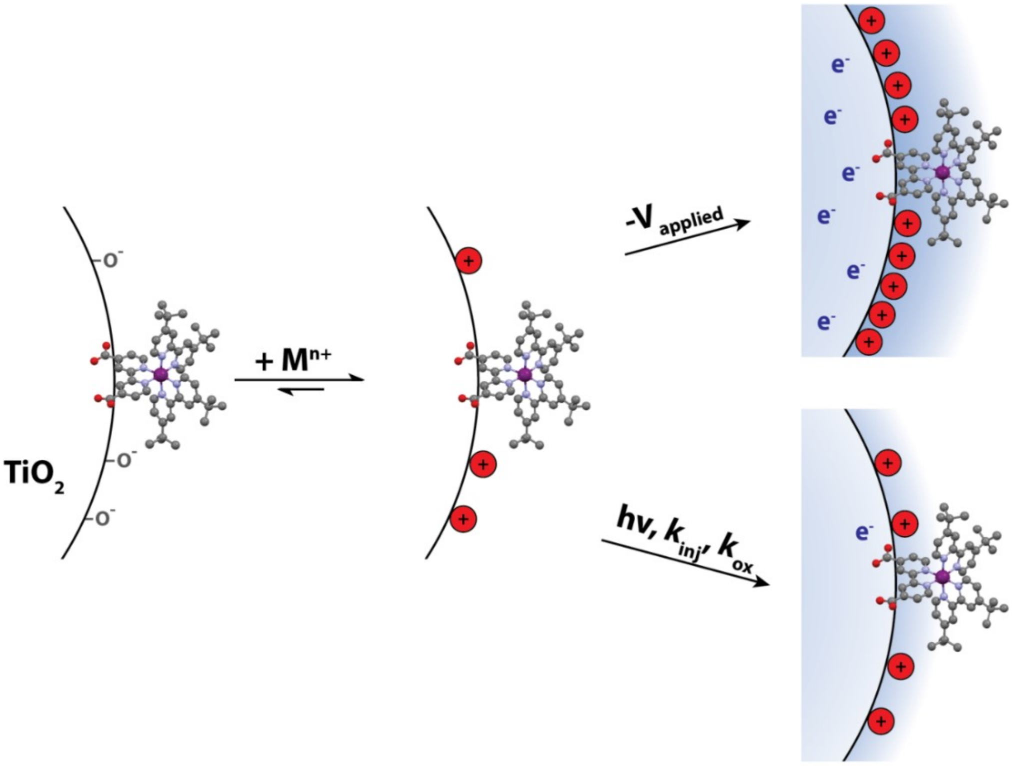

Figure 3.15. Graphical depiction of the key experimental differences discussed.

For example, the conduction band edge position has been reported to be -2.1 V vs. SCE in 1.0 M $TBAClO_4$, where the tetrabutylammonium (TBA) cation was reasonably asserted to interact only weakly with the TiO_2 surface, and shifted 1.1 V positive when Lewis acidic Li^+ cations were present.[66] Similar shifts have been reported in other non-aqueous solutions.[67,70] The cation concentration dependence of these shifts is often non-linear and generally one needs to determine the values experimentally under conditions most relevant to the DSSC.

Spectro-electrochemistry has been widely utilized to characterize the acceptor states of the mesoporous anatase TiO_2 thin films used in DSSCs.[6,61,71] Reduction of TiO_2 results in a black coloration as well as a blue shift of the fundamental absorption. For a given cation, the measured spectra were normalizable over the potential range that was investigated, 0.0 to -1.0 V vs. NHE, Figure 3.5. The extinction coefficients were calculated from the measured absorption spectra and the amount of change present in the film as was determined by the charge extraction technique of un-sensitized TiO_2.[59-61] The value measured at 700 nm of $\varepsilon = 930 \pm 50\ M^{-1}\ cm^{-1}$ were within experimental error the same and in good agreement with previously published values, Figure 3.7.[61,70,72]

While the coloration associated with TiO_2 reduction is well known, an assignment of the underlying electronic transition(s) is not. The blue shift of the fundamental absorption has been attributed to both an electric field[16,73-74] and a band – filling, i.e. a Burstein-Moss shift, effect.[70-71,75] There is no consensus on which is correct. Under moderate reduction potentials, the long wavelength absorption displays no clear peak out to 1100 nm. The lack of a maximum and the high extinction coefficient are inconsistent with assignment as a ligand field ($t_{2g} \rightarrow e_g^*$) transition, like that seen in Ti(III) compounds such as $Ti(H_2O)_6^{3+}$, λ_{max} = 475 nm and ε = 5 M^{-1} cm^{-1}.[76] This implies that the long wavelength TiO_2 absorption has some intervalence $Ti^{IV/III}$ character and/or results from electronic transitions that are not easily reconciled on a molecular level. All the unsolvated cations under study are small enough to intercalate into the (101) anatase TiO_2 lattice where they could inductively interact with Ti centers throughout the nanocrystallite.[66,70,77-81] Under strongly reducing conditions, new absorption features arise that were clearly dependent on the nature of the cation present, Figure 3.8. The spectra measured in a Li^+ electrolyte were consistent with the known spectrum of the fully intercalated $Li_{0.5}TiO_2$ phase.[70,82] Strong reduction in the presence of the other cations may also lead to intercalated phases, however this was not studied in as much detail as such conditions were found to irreversibly change the TiO_2 material as evidenced by significant hysteresis in absorption vs. applied potential scans.

Application of a sufficiently positive potential to a $Ru(dtb)_2(dcb)/TiO_2$ thin film resulted in absorption changes consistent with oxidation of Ru(II) to Ru(III). The electrochemistry itself was non-Nernstian and the equilibrium potential where the concentrations of the two redox states were equal was taken as an estimate of the formal $E^o(Ru^{III/II})$ reduction potential. The formal reduction potentials were about 50 mV more positive with the dicationic Mg^{2+} and Ca^{2+} relative to the Na^+ and Li^+, i.e. $E^o(Ru^{III/II})$ = 1.50 V vs. $E^o(Ru^{III/II})$ = 1.45, Figure 3.9. More significant were the deviations from Nernstian behavior, where a factor of ten change in concentration required 80 mV for Li^+ and 103 mV for Ca^{2+}, Table 1.

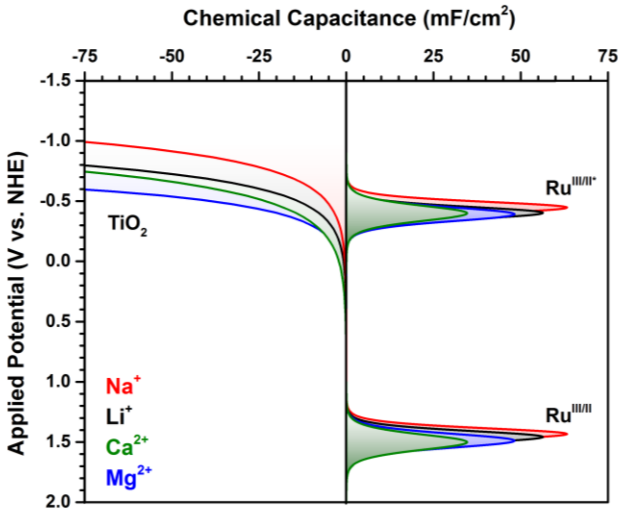

Figure 3.16. Density of acceptor states obtained from spectroelectrochemistry for sensitized TiO_2 compared with the ground- and excited-state Ru$^{III/II}$ reduction potentials in 100 mM metal perchlorate acetonitrile electrolytes.

Previous studies of non-Nernstian redox chemistry of molecules anchored to TiO_2 concluded that the non-idealities resulted from surface electric fields.[83-84] Since cation adsorption does significantly change the electric field as measured spectroscopically (see below) the results presented in this chapter are in agreement with this conclusion.

The spectro-electrochemical data was utilized to construct a density of states diagram using a previously described method[83,85-86] for $Ru(dtb)_2(dcb)/TiO_2$ in the different electrolytes, Figure 3.16. The density of TiO_2 acceptor states was found to increase exponentially as the Fermi-level was raised toward the vacuum level, behavior that is consistent with many other reports.[12,85] The cation dependency is clearly seen at any potential of interest. For example at -0.5 V, a potential that corresponds with the excited state reduction potential, the density increases in the order $Na^+ < Li^+ < Ca^{2+} < Mg^{2+}$, a trend that was clear at all potentials where a measureable concentration of $TiO_2(e^-)$s were present. The chemical capacitance distributions for the $Ru^{III/II}$ redox chemistry are not Gaussian and reflect the non-Nernstian redox chemistry described above. The magnitudes of the chemical capacitances were proportional to the surface coverage and the different values given in Figure 3.16 were not significant and likely result from the unknown extinction coefficients of the surface anchored compounds. The reduction potential of the thermally equilibrated excited states, $E^o(Ru^{III/II*})$, were calculated through a thermochemical cycle and the distribution was assumed to be the same as the ground state.

The free energy stored in the thermally equilibrated excited state $E^o(Ru^{III/II*})$ was abstracted from the steady state photoluminescence spectra. It was found that the presence of 100 mM of these cations in the electrolyte that surrounded a $Ru(dtb)_2(dcb)/TiO_2$ thin film, resulted in a bathochromic (red) shift of both the absorption and the photoluminescence (PL) spectra of magnitude $Na^+ < Li^+ < Ca^{2+} < Mg^{2+}$, Figure 3.4. The absorption data is discussed in more detail in the following section. The PL spectral shifts were accompanied by a dramatic quenching of PL intensity. The decrease in intensity is reasonably attributed to quenching by the TiO_2 acceptor states. Indeed, the interfacial density of states shown in Figure 3.16 indicates that excited state injection should be favorable for $Ru(dtb)_2(dcb)/TiO_2$ under all conditions. However, PL is an indirect probe of electron transfer and the radiative and non-radiative rate constants for excited state relaxation may also be influenced by cation adsorption. Indeed, it has been shown that the PL spectra of $Ru(dtb)_2(dcb)/TiO_2$ was sensitive to the excitation irradiance and blue shifted as the number of incident photons was increased, behavior attributed to a local electric field.[46] If the PL quenching were solely due to excited state injection *and* injection did not occur in neat acetonitrile, then the PL data would be consistent with injection yields of 0.95 for Na^+ and essentially unity for the other cations. The values measured by comparative actinometry 100 ns after laser excitation were indeed found to be unity for all the cations except Na^+, indicating that excited state electron transfer to TiO_2 was indeed the main excited state relaxation pathway. The injection yields were consistent with previous studies that showed a correlation between injection yields and the charge-to-size ratio.[69] The previous work was done at only 2 mM concentrations where the studies reported in this chapter were performed under concentrations where the influence of the cation had reached its maximum value.

3.4.2 Electric Fields and Screening.

Abstraction of the electric field strength from the absorption data was accomplished by an analysis briefly described in the Results Section and in previous publications.[17-18,46,51]

In brief, the magnitude of the absorption shift that accompanied a change in the electric field experienced by the surface anchored Ru compounds, was quantified by both first-derivative and peak-to-peak analyses and found to give the same values within experimental error. The first-derivative change indicates that the field was collinear with the dipole moment change that was assumed to be $\Delta\vec{\mu}$ = 4.75 D under all conditions studied.[19,46] Previous studies have shown that the spectral shifts occur in the opposite direction when the dipole moment and electric field vectors are aligned antiparallel to each other.[18] Very recent work has shown that electroabsorption can be used to quantify the distance between the molecular chromophore and the TiO_2 surface.[87] The data reported in this chapter have enabled characterization of electric field changes that accompany cation adsorption, electrochemical reduction, and excited state injection and are discussed below.

The adsorption of ions to semiconductor surfaces is known and expected to generate local electric fields.[68,88-93] Previous studies have focused mainly on Li^+ cations that are most widely utilized in DSSCs. Adsorption isotherms provided an estimate of the room temperature equilibrium constant, $K = 15 – 80\ M^{-1}$.[17] Through the data presented in this chapter, it was discovered that closely related spectral shifts were observed with Na^+ and alkaline earth metal cations. The data support the widely held notion that prior to any surface treatments the sol-gel processed TiO_2 nanocrystallites present in the mesoporous TiO_2 thin films are negatively charged.[68] This negative charge is not attributed to injected electrons as there is no spectroscopic evidence for their presence and the spectral shifts were observed in air saturated solutions, conditions where the injected electrons are known to rapidly react. Instead the charge is attributed to specific functional groups, most likely deprotonated titanol groups, see Figure 3.15. Whatever the chemical nature might be, the significant bathochromic (red) shift of the MLCT absorption that accompanied cation exposure reflects both the screening of this charge from the sensitizer and the field that is generated by the cation adsorption itself. The magnitude was sensitive to the identity of the cation and followed the trend $Na^+ < Li^+ < Ca^{2+} < Mg^{2+}$. A key point though is that there is no a priori reason to expect that the surface charge due to cation adsorption is the same for each cation. This is important as the electric fields quantified after excited state injection or electrochemical reduction represent the change in the electric field from the initial condition of 100 mM cation concentration, as is shown in Figure 3.15.

Injection of electrons into a $Ru(dtb)_2(dcb)/TiO_2$ thin film resulted in a bathochromic shift of the MLCT absorption that was opposite in sign to that measured with cation adsorption. Measurements as a function of applied potential revealed a strong cation dependence, Figure 3.10. The potential dependent data was recast as the number of $TiO_2(e^-)$s per anatase nanocrystallite. While some experimental uncertainty was introduced by this conversion, the trends reported remain the same. The conversion was important for internal comparisons as the number of electrons present at any applied potential were found to be cation dependent. For all four cations studied, the magnitude of the electric field first increased linearly with the number of $TiO_2(e^-)$s and then more slowly with the number of $TiO_2(e^-)$s, Figure 3.11. The data suggests that the first electrons injected into TiO_2 reside near the interface and subsequent electrons reside further away from the surface where they have a smaller influence on the surface anchored compounds.

About 20 $TiO_2(e^-)$s are thought to reside in each nanocrystallite at the power point condition of optimized DSSCs,[7,13] so it is of interest to compare the field strengths reported by the sensitizer at this condition. The field strengths varied by about a factor of two and increased in the order: $Na^+ < Li^+ < Mg^{2+} < Ca^{2+}$, Table 3.2. Since the number of $TiO_2(e^-)$s was the same, the variations in field reflect the ability of the cations to screen the $TiO_2(e^-)$s charge from the surface anchored Ru compound. The largest diameter cation, Ca^{2+}, was the poorest at screening charge yet Na^+ was more effective that was the smaller Li^+. Interestingly, Mg^{2+} was found to screen the field more effectively than did Li^+ when the number of $TiO_2(e^-)$s per nanoparticle exceeded about 70. Hence the dication Mg^{2+} was more effective at charge screening when the number of $TiO_2(e^-)$s was large. As was described in the Introduction of this chapter, it is not clear whether electric fields and charge screening influence the efficiency of DSSCs; however for recombination to negatively charged acceptors like I_3^-, screening should be detrimental.[68,90]

Pulsed laser excitation enabled charge screening dynamics to be probed after excited state injection. Experimentally, it was found that this was most easily accomplished when iodide was present in the cell. Charge recombination to the oxidized iodide species was much slower than to the oxidized dye and the first derivative absorption signature associated with the Stark effect was much more easily observed spectroscopically after regeneration by iodide, Figure 3.12. The magnitudes of the field measured 2.5 μs after the laser excitation followed the trend $Na^+ < Ca^{2+} < Li^+ < Mg^{2+}$, Table 2. However, the amplitudes of the Stark effect were time dependent for each cation making comparisons difficult. Under such conditions, there exists a large time window between 500 ns and 1 ms, where the number of $TiO_2(e^-)$s was constant yet the spectral feature associated with the electric field decreased rapidly. Burdziński and coworkers have suggested that these dynamics reflect electron trapping at grain boundaries.[94] The strong cation dependence reported here indicates that this is not the sole source of the observed dynamics, as there is no *a priori* reason to believe that trapping at grain boundaries would also be cation dependent. It was found that the monovalent cations screened charge much more rapidly than did the dications, $k_{Li+,Na+} = 5.0 \times 10^4$ s^{-1} and $k_{Mg2+,\ Ca2+} = 5.0 \times 10^2$ s^{-1} (see Figure 3.14), presumably because the small number of electrons injected into TiO_2 resulted in spatially isolated anionic Ti(III) sites that were more easily screened by the monovalent cations. These rate constants indicate that charge screening of the field generated by excited state injection was not fully established before recombination to oxidized iodide occurred. A larger dynamic window for quantifying charge screening would hence be expected for mediators that underwent slower electron transfer with $TiO_2(e^-)$s.

3.5 Conclusion

Surface electric fields are generated when charged species adsorb onto or are injected into TiO_2 nanocrystallites interconnected in a mesoporous thin films commonly used in dye-sensitized solar cells. The MLCT absorption of $Ru(dtb)_2(dcb)^{2+}$ compounds anchored to the TiO_2 surface are sensitive probes of these electric fields. Exposure of a $Ru(dtb)_2(dcb)/TiO_2$ thin film immersed in acetonitrile to cations resulted in bathochromic (red) shifts of the MLCT absorption that followed the trend $Na^+ < Li^+ < Ca^{2+} < Mg^{2+}$. The magnitude of the field change with Na^+ was 6.9 MV/cm and that for Mg^{2+} was 11 MV/cm. Injection of electrons into TiO_2, from a potentiostat or an excited state, resulted in hypsochromic (blue) shifts. Pulsed laser excitation enabled the kinetics for charge screening at the interface to be quantified. On average, screening was about 100 times faster for the alkali cations relative to the alkaline earths. This behavior was attributed to excited state injection yielding localized Ti(III) states that were more easily screened by ions with a single positive charge.

3.6 Appendix

Photo-induced electron transfer reactions at dye-sensitized TiO_2 interfaces generate electric fields.[95] At semiconductor-electrolyte interfaces, ions and solvent molecules respond to this photo-generated field by movement from their equilibrium (dark) configurations. Such interfacial reorganization decreases the magnitude of the electric field experienced by the surface anchored dye molecules, in a poorly defined process often referred to generically as 'screening'.[17,39,46] The ability of semiconductor-electrolyte interfaces to reorganize and screen charges under different illumination levels may underlie the higher efficiency of photoelectrochemical cells relative to solid state photovoltaics under weak or intermittent sunlight. Unfortunately, very little mechanistic charge screening data exists, particularly for the dynamics of the process.[17,39,46] The first comparative kinetic data for charge screening at dye-sensitized TiO_2 interfaces in different electrolytes is presented here. The presence of Lewis acidic Li^+ or Mg^{2+} ions in the electrolyte was found to have a significant influence on charge screening.

Quantification of the kinetics for photo-induced charge screening was enabled by the recent discovery that the electric field generated by electrons injected into TiO_2 significantly influences the absorption spectra of surface anchored dye molecules.[17-18] This discovery was initially met with some skepticism as the electric field was expected to be screened by the high permittivity of TiO_2 and the high ionic strength of acetonitrile electrolytes. Nevertheless, electron transfer induced spectral changes have now been observed in at least seven different labs[18,39,43-44,96-101] and have a sound theoretical basis.[102-103] The induced absorption changes were similar to that observed in electro-absorption spectroscopy and were therefore termed a "Stark Effect".[19,104] However, the special orientation of the field generated at the semiconductor interface results in spectral changes that are quantitatively different than that observed in traditional Stark spectroscopy. Due to the approximately normal orientation of the molecular dipole difference relative to the semiconductor electric field, uni-directional shifts of the absorption spectra were observed that gave rise to first-derivative spectral changes rather than the second-derivative spectra that are generally observed in traditional Stark spectroscopies.[24,46] A pictorial representation of these spectral changes observed at TiO_2 interfaces is shown in Figure 3.17.

In the course of studying the Stark effect, it was found that the magnitude of the intensity change was particularly large for the compound $Ru(dtb)_2(dcb)^{2+}$, where dtb is 4,4'-(*tert*-butyl)$_2$-2,2'-bipyridine and dcb is 4,4'-$(CO_2H)_2$-2,2'-bipyridine, shown in Figure 3.17.[17,46] Presumably the tertiary butyl groups enforce a normal orientation of the compound relative to the TiO_2 surface and the tris-bipyridyl octahedral geometry about the ruthenium center gives rise to a large dipole moment change upon light absorption. Whatever the origin, the $Ru(dtb)_2(dcb)^{2+}$ compound anchored to TiO_2, abbreviated $Ru(dtb)_2(dcb)/TiO_2$ is ideal for characterization of interfacial screening.[17,46] Such data is presented in this Appendix with two specific electrolytes both containing 0.25 M tetrabutyl ammonium iodide (TBAI) yet one with 0.1 M Li^+ ions and the other with 0.1 M Mg^{2+} ions. The nature of the Lewis acidic cation was found to have a significant influence on charge screening dynamics and the density of TiO_2 acceptor states.

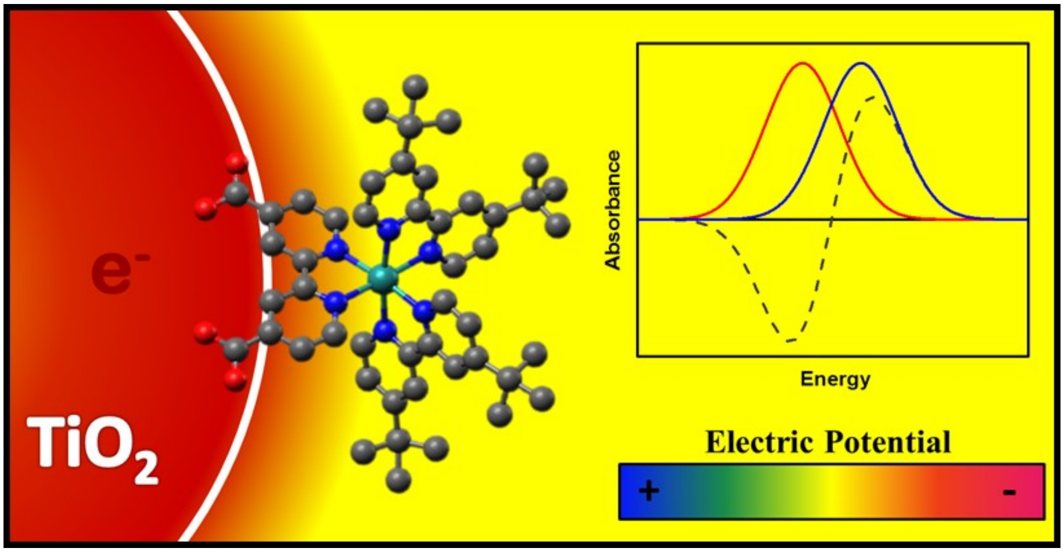

Figure 3.17. A Ru(dtb)$_2$(dcb)/TiO$_2$ interface with an injected electron, e$^-$, that generates an electric field that shifts the absorption spectrum (blue) of the ruthenium compound to higher energy compared to that without the field (red). The spectral shift appears as a first-derivative when measured as a difference spectrum (dotted lines).

Shown in Figure 3.18 is the absorption spectrum of a Ru(dtb)$_2$(dcb)/TiO$_2$ thin film immersed in neat acetonitrile and 0.1 M LiClO$_4$ or 0.1 M Mg(ClO$_4$)$_2$ acetonitrile solutions. A significant red shift in the metal-to-ligand charge-transfer (MLCT) absorption was observed in the electrolyte solutions as well as a small decrease in the maximum absorption intensity. The decrease in the absorptivity at ~ 450 nm was offset by an increased absorption at ~ 400 nm such that the oscillator strength of the MLCT absorption, integrated from 370 to 700 nm, was essentially insensitive to the nature of the cation. The red shift in the MLCT absorption has previously been noted for Li$^+$,[17,39,46] and is consistent with cation adsorption to negatively charged TiO$_2$. These Lewis acidic cations likely form adducts with the oxide oxygen atoms, as has been seen crystallographically for related Ti(IV) materials,[105] that screens the surface electric field and hence a perturbation of the MLCT absorption. As was previously described, the magnitude of the spectral shift reports directly on the change in the field experienced by the surface anchored ruthenium compound.[46] Assuming a dipole moment change of 4.75 D[19] and a collinear alignment of the dipole moment change and the electric field, the Mg^{2+} ions were found to screen the charge more effectively than did Li$^+$, $\Delta E = 10.7$ MV/cm *vs.* $\Delta E = 7.52$ MV/cm. The Mg^{2+} and Li$^+$ ionic radii are approximately the same so Mg^{2+} has a lower size-to-charge ratio and more effective screening would hence be expected.[106]

Both Li$^+$ and Mg^{2+} are known to be 'potential determining ions' for TiO$_2$ and result in significant changes in the energetic position of the valence and conduction band edges.[66-69] The influence of these cations on the acceptor states of TiO$_2$ was quantified here by spectro-electrochemistry. Unsensitized TiO$_2$ thin films immersed in the indicated electrolytes were reduced electrochemically, Figure 3.19. The characteristic blue-black color of reduced TiO_2, abbreviated $TiO_2(e^-)$, was observed at sufficiently negative bias.[107-108] The potential onset for coloration was found to be more positive, i.e. further from the vacuum level, when Mg^{2+} cations were present relative to Li^+. This behavior is qualitatively consistent with a previous report that the TiO_2 conduction band edge was 200 mV more negative in acetonitrile electrolytes of 0.1 M $LiClO_4$ (-0.65 V versus NHE) relative to 0.1 M $Mg(ClO_4)_2$ (-0.45 V).[66] What had apparently gone unnoticed was the shift in the fundamental valence-to-conduction band absorption of TiO_2 as the film was reduced in these two electrolytes. As the films were reduced in either electrolyte solution, the fundamental absorption shifted to higher energy with loss of isosbestic points that appeared as a bleach when an unreduced TiO_2 thin film was used as the reference, Figure 3.19. However, the magnitude of the bleach, relative to the $TiO_2(e^-)$ absorption at longer wavelengths, was significantly larger for the Li^+ containing electrolyte than for the Mg^{2+} containing electrolyte, approximately 3:1 versus 1:1.

The origin of the blue shift that accompanies reduction of anatase TiO_2 nanocrystallites, as well as other semiconductor nanoparticles, was originally attributed to a Burstein-Moss shift (i.e. conduction band filling),[70-71,75,109] but was more recently recognized to be a Stark effect.[16,73-74,110] The more significant change in the fundamental absorption implies that Mg^{2+} screens the electric field more efficiently than Li^+. It should be emphasized that this effect is quite different from the celebrated Franz-Keldysh effect for bulk semiconductor materials where a strong electric field induces a band gap decrease without any redox chemistry.[111-112]

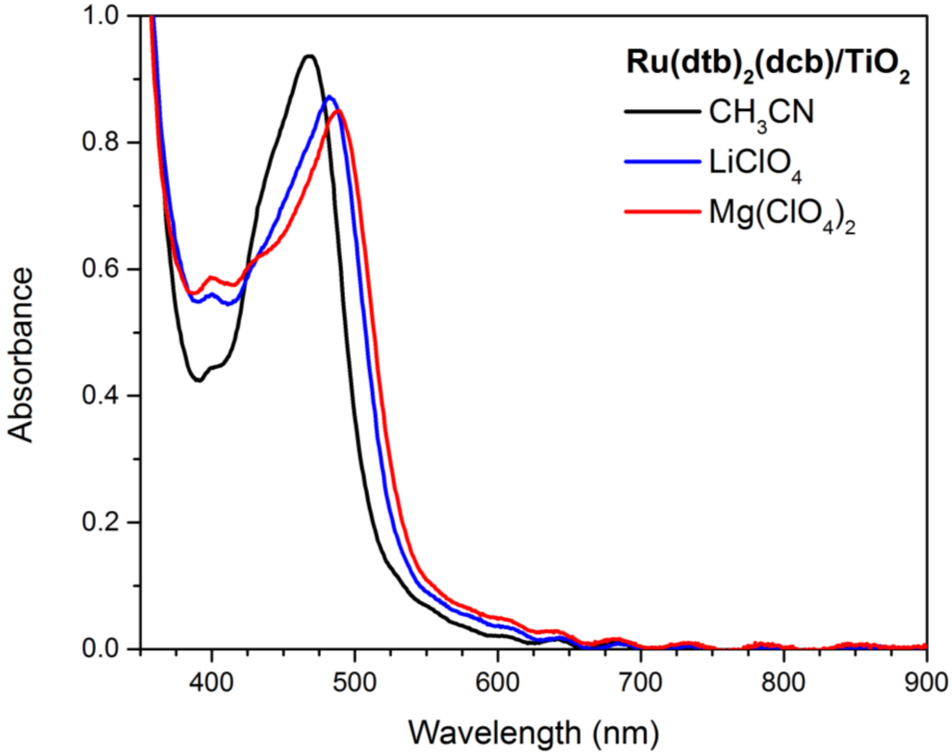

Figure 3.18. Ground state ultraviolet–visible absorbance spectra of a Ru(dtb)$_2$(dcb)/TiO$_2$ thin film immersed in acetonitrile in the absence (black) or presence of 100 mM LiClO$_4$ (blue) or Mg(ClO$_4$)$_2$ (red).

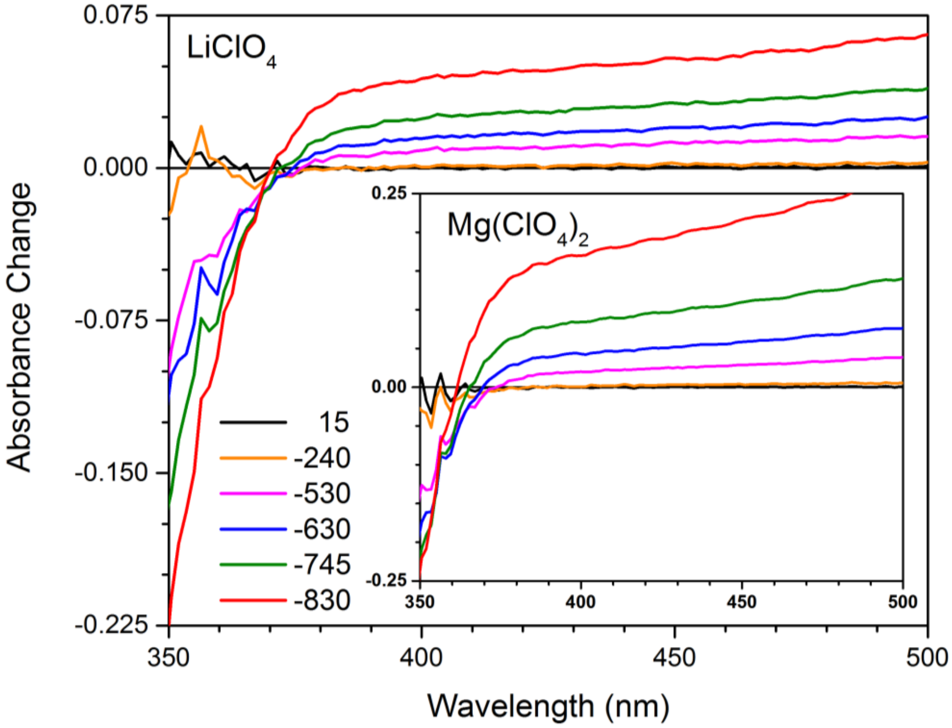

Figure 3.19. Spectroelectrochemistry of unsensitized TiO_2 thin films anchored to FTO glass in acetonitrile electrolytes of 0.1 M $LiClO_4$ (main) and $Mg(ClO_4)_2$ (inset) at the indicated applied biases (mV vs. NHE): 15, black; -240, orange; -530, magenta; -630, blue; -745, green; and -830, red.

Nanosecond transient absorption spectroscopy was used to study $Ru(dtb)_2(dcb)/TiO_2$ thin films immersed in acetonitrile solutions containing 0.25 M TBAI and either 0.1 M $LiClO_4$ or $Mg(ClO_4)_2$. Great care was taken to ensure that the ground state absorption and the incident irradiance were the same in the two electrolytes. Shown in Figure 3.20 are representative spectra recorded 2.5 μs after laser excitation, a delay time selected to ensure that all the iodide redox chemistry was complete and that the sensitizers were fully regenerated.[113] Hence only the injected electrons, tri-iodide, and ground state sensitizers were observed.

The large first-derivative looking feature centered ~ 490 nm has previously been observed and is a signature of the Stark effect. The electrons injected into TiO_2 generate an electric field that significantly blue shifts the MLCT absorption of the ruthenium compounds anchored to the surface. The magnitude of the absorption changes associated with the Stark effect were significantly more intense when Mg^{2+} electrolytes were employed, behavior attributed to the faster Li^+ screening as is described below.

Shown in Figure 3.21 are single wavelength absorption changes monitored at 750 nm and the maximum bleach associated with the Stark effect. For observation times less than 0.5 microseconds, di-iodide disproportionation chemistry was found;[113] while for times greater than 1 ms, recombination of the injected electrons with the redox mediator was observed. At intermediate times, the amplitude of the Stark effect decreased while the $TiO_2(e^-)$ concentration and hence the electric field were constant, behavior attributed to "screening" of the field by interfacial ionic reorganization. Kinetic data for this screening are shown as the bleach between the dashed vertical lines in the figure.

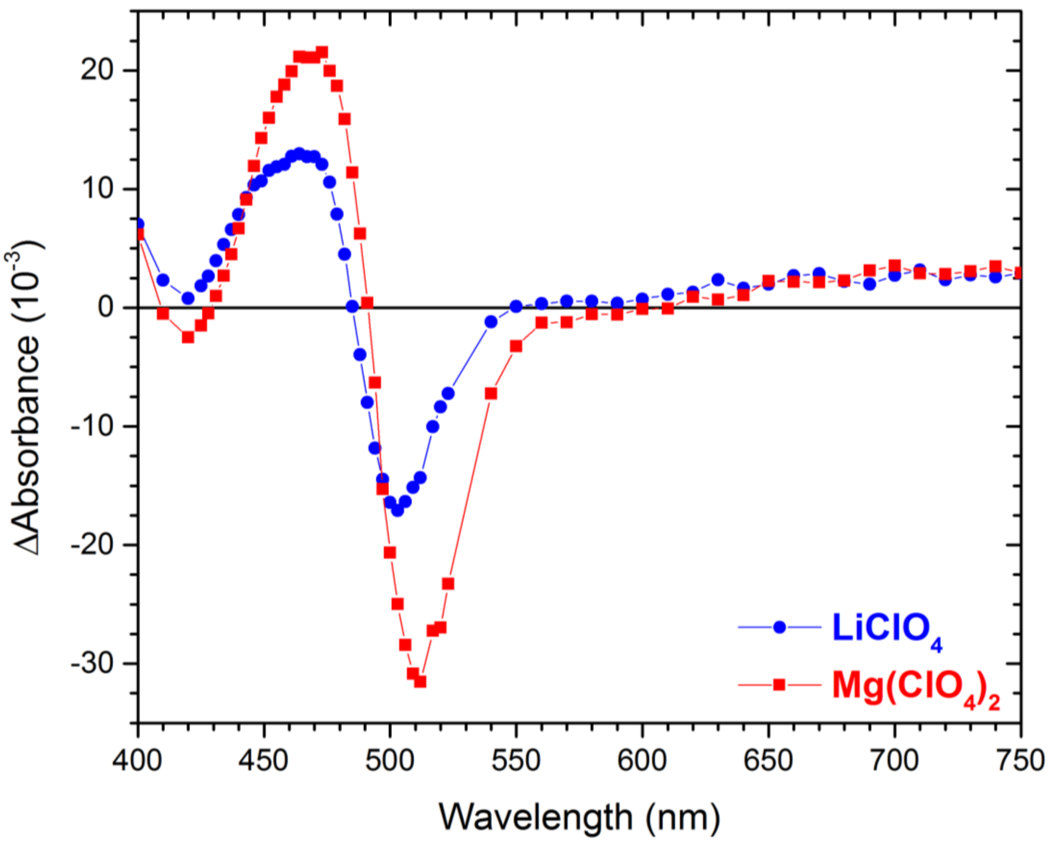

Figure 3.20. Transient absorption spectra of a Ru(dtb)$_2$(dcb)/TiO$_2$ thin film obtained 2.5 μs after pulsed 532 nm excitation in acetonitrile electrolyte containing 0.25 M TBAI and either 0.1 M LiClO$_4$ (blue) or Mg(ClO$_4$)$_2$ (red).

The screening kinetics were non-exponential and were well described by the Kohlrausch−Williams−Watts (KWW) model, Equation (3.9).[17,114]

$$I(t) = I_o \exp[-(kt)^{\beta}] \tag{3.9}$$

Here β is inversely related to the width of an underlying Lévy distribution of rate constants, $0 < \beta < 1$, and k is a characteristic rate constant. In kinetic analysis, the value of β was fixed to be 0.2, and the rate constants abstracted were $k_{Li+} = 5.3 \times 10^4$ s^{-1} and $k_{Mg2+} = 4.7 \times 10^2$ s^{-1}. Based on this kinetic analysis, the rate constants for charge screening were about 100 fold slower for Mg^{2+} ions than for Li^+ ions. To ensure that the rate constants were insensitive to the number of injected electrons, the incident irradiance was varied over a factor of six and the normalized data were unchanged. The figure inset shows kinetic data as a function of irradiance measured in the Mg^{2+} containing electrolyte with overlaid fits, $k_{Mg2+} = 4.7 \times 10^2$ s^{-1} and $\beta = 0.2$.

The smaller rate constants for charge screening by Mg^{2+} relative to Li^+ was unexpected based on the (dark) equilibrium spectroscopic data, Figure 3.18 and Figure 3.19, which showed that the divalent cation gave rise to smaller spectral shifts in the fundamental TiO_2 absorption and larger spectral shifts in the MLCT absorption attributed to more effective charge screening. A plausible explanation for the disparity in rate constants is that electron injection into TiO_2 yields one injected electron and this charge was neutralized by adsorption and/or intercalation of a single cation, not a dicationic ion. Indeed Lyon and Hupp have shown that a 1:1 stoichiometry exists between Li^+ and H^+ cations and electrochemically generated $TiO_2(e^-)$s.[115]

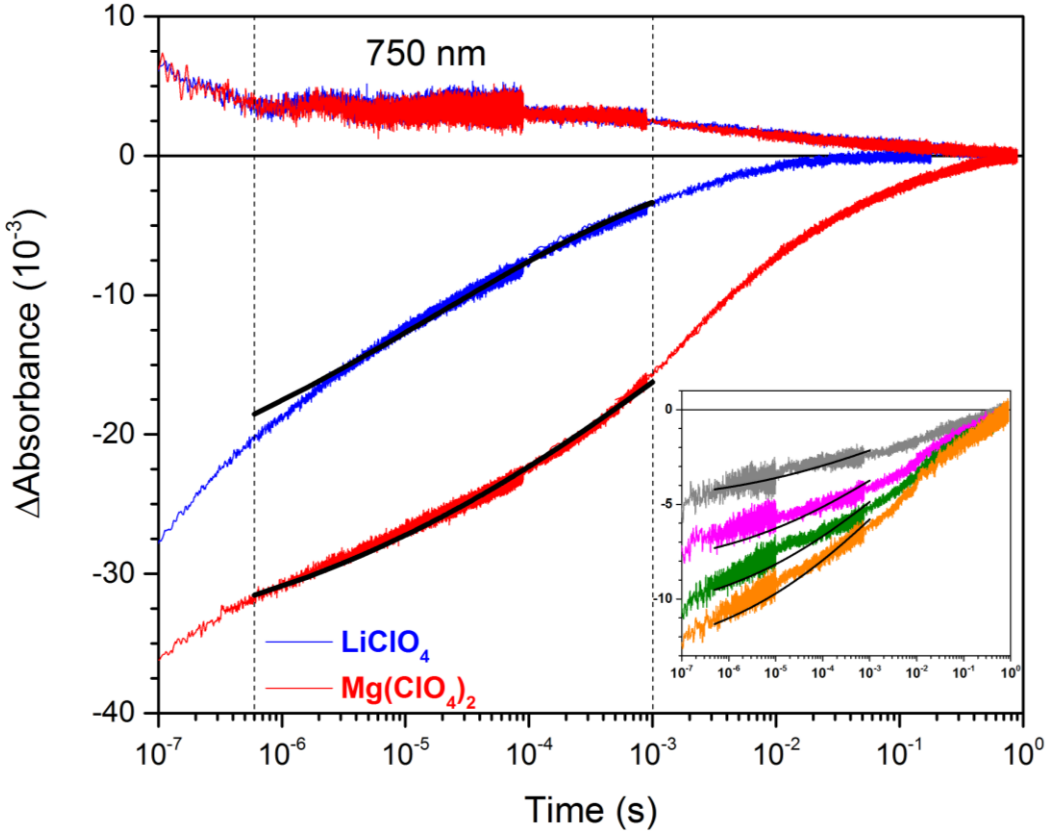

Figure 3.21. Absorption change measured after pulsed 532 nm excitation of a Ru(dtb)$_2$(dcb)/TiO$_2$ thin film immersed in 0.1 M LiClO$_4$ (blue) or Mg(ClO$_4$)$_2$ (red) acetonitrile. The dotted vertical lines bracket time periods where the TiO$_2$(e$^-$) concentration was constant yet the bleach amplitude associated with the Stark effect was decreasing, behavior attributed to charge screening. The inset depicts the charge screening kinetics in the presence of Mg(ClO$_4$)$_2$ as a function of laser fluence increasing from top to bottom: 0.2 (grey), 1.2 (magenta), 2.3 (green), to 3.5 (orange) mJ/pulse. Overlaid in black on some data are best fits to the KWW function.

In contrast, surface adsorption of a divalent cation would generate a net positive change on the surface and hence requires either a second injected electron or a charge-balancing anion that could account for the smaller rate constant measured experimentally.

The strong cation dependence for the loss of absorption associated with the Stark effect while the $TiO_2(e^-)$ concentration was fixed is fully consistent with a screening mechanism. This data does not support an alternative mechanism by Burdziński and coworkers that these dynamics reflect electron trapping at grain boundaries as there is no *a priori* reason that such trapping would be sensitive to the cation identity.[97] Furthermore, Snaith and coworkers' data in solid state dye sensitized solar cells, where the addition of Li^+ resulted in slower recombination and hence a longer lived absorption transient, are fully consistent with an underlying Stark effect.[116]

In summary, cation adsorption to sensitized TiO_2 nanocrystallites in acetonitrile solution resulted in a bathochromic shift of the sensitizer steady state absorption spectra consistent with a Stark effect and charge screening. The Mg^{2+} ions were found to screen charge, $\Delta E = 10.7$ MV/cm, more effectively than did Li^+, $\Delta E = 7.52$ MV/cm. Pulsed laser excitation of the sensitized materials led to excited state injection and generation of an electric field that was of comparable magnitude for the two electrolytes. The Li^+ containing electrolyte was found to screen this photogenerated field far more rapidly than did Mg^{2+}, $k_{Li+} = 5.3 \times 10^4$ s^{-1} and $k_{Mg2+} = 4.7 \times 10^2$ s^{-1}. The factor of 100 change in rate constant induced by altering the cation present in the electrolyte was most consistent with charge screening and far less consistent with a model where the injected electrons were trapped at grain boundaries. The data described herein show that Stark spectroscopy can be used to directly quantify charge screening at illuminated semiconductor interfaces and that such dynamics can be highly dependent on the nature of the electrolyte.

3.7 References

(1) O’Donnell, R. M.; Ardo, S.; Meyer, G. J. *The Journal of Physical Chemistry Letters* **2013,** *4*, 2817-2821.

(2) O’Donnell, R. M.; Sampaio, R. N.; Barr, T. J.; Meyer, G. J. *J. Phys. Chem. C* **2014,** *118*, 16976-16986.

(3) Gao, Y. *Acc. Chem. Res.* **1999,** *32*, 247-255.

(4) Clarke, T. M.; Durrant, J. R. *Chem. Rev.* **2010,** *110*, 6736-6767.

(5) Bisquert, J.; Garcia-Belmonte, G. *J. Phys. Chem. Lett.* **2011,** *2*, 1950-1964.

(6) Ardo, S.; Meyer, G. J. *Chem. Soc. Rev.* **2009,** *38*, 115-164.

(7) Hagfeldt, A.; Boschloo, G.; Sun, L.; Kloo, L.; Pettersson, H. *Chem. Rev.* **2010,** *110*, 6595-6663.

(8) Song, W.; Chen, Z.; Glasson, C. R. K.; Hanson, K.; Luo, H.; Norris, M. R.; Ashford, D. L.; Concepcion, J. J.; Brennaman, M. K.; Meyer, T. J. *ChemPhysChem* **2012,** *13*, 2882-2890.

(9) O'Regan, B.; Grätzel, M. *Nature* **1991,** *353*, 737-740.

(10) Kamat, P. V. *J. Phys. Chem. C* **2007,** *111*, 2834-2860.

(11) Kamat, P. V. *J. Phys. Chem. Lett.* **2013,** *4*, 908-918.

(12) Albery, W. J.; Bartlett, P. N. *J. Electrochem. Soc.* **1984,** *131*, 315-325.

(13) O’Regan, B. C.; Durrant, J. R. *Acc. Chem. Res.* **2009,** *42*, 1799-1808.

(14) *CRC Handbook of Chemistry and Physics, 91st ed.* CRC Press: Boca Raton, 2010.

(15) Cahen, D.; Hodes, G.; Grätzel, M.; Guillemoles, J. F.; Riess, I. *J. Phys. Chem. B* **2000,** *104*, 2053-2059.

(16) Zaban, A.; Meier, A.; Gregg, B. A. *J. Phys. Chem. B* **1997,** *101*, 7985-7990.

(17) Ardo, S.; Sun, Y.; Staniszewski, A.; Castellano, F. N.; Meyer, G. J. *J. Am. Chem. Soc.* **2010,** *132*, 6696-6709.

(18) Cappel, U. B.; Feldt, S. M.; Schöneboom, J.; Hagfeldt, A.; Boschloo, G. *J. Am. Chem. Soc.* **2010,** *132*, 9096-9101.

(19) Oh, D. H.; Boxer, S. G. *J. Am. Chem. Soc.* **1989,** *111*, 1130-1131.

(20) Vance, F. W.; Hupp, J. T. *J. Am. Chem. Soc.* **1999,** *121*, 4047-4053.

(21) Karki, L.; Hupp, J. T. *Inorg. Chem.* **1997,** *36*, 3318-3321.

(22) Hug, S. J.; Boxer, S. G. *Inorg. Chim. Acta* **1996,** *242*, 323-327.

(23) Bublitz, G. U.; Boxer, S. G. *Annu. Rev. Phys. Chem.* **1997,** *48*, 213-242.

(24) Boxer, S. G. *J. Phys. Chem. B* **2009,** *113*, 2972-2983.

(25) Middendorf, T. R.; Mazzola, L. T.; Lao, K.; Steffen, M. A.; Boxer, S. G. *Biochim. Biophys. Acta* **1993,** *1143*, 223-234.

(26) Lao, K.; Moore, L. J.; Zhou, H.; Boxer, S. G. *J. Phys. Chem.* **1995,** *99*, 496-500.

(27) Vance, F. W.; Williams, R. D.; Hupp, J. T. *Int. Rev. Phys. Chem.* **1998,** *17*, 307-329.

(28) Brunschwig, B. S.; Creutz, C.; Sutin, N. *Coord. Chem. Rev.* **1998,** *177*, 61-79.

(29) Liptay, W. *Angew. Chem., Int. Ed. Engl.* **1969,** *8*, 177-188.

(30) Reimers, J. R.; Hush, N. S. *J. Phys. Chem.* **1991,** *95*, 9773-9781.

(31) Karki, L.; Hupp, J. T. *Inorg. Chem.* **1997,** *36*, 3318-3321.

(32) Vance, F. W.; Hupp, J. T. *Journal of the American Chemical Society* **1999,** *121*, 4047-4053.

(33) Walters, K. A.; Gaal, D. A.; Hupp, J. T. *J. Phys. Chem. B* **2002,** *106*, 5139-5142.

(34) Khoudiakov, M.; Parise, A. R.; Brunschwig, B. S. *J. Am. Chem. Soc.* **2003,** *125*, 4637-4642.

(35) Harris, J. A.; Trotter, K.; Brunschwig, B. S. *J. Phys. Chem. B* **2007,** *111*, 6695-6702.

(36) Nawrocka, A.; Zdyb, A.; Krawczyk, S. *Chem. Phys. Lett.* **2009,** *475*, 272-276.

(37) Zdyb, A.; Krawczyk, S. *Appl. Surf. Sci.* **2010,** *256*, 4854-4858.

(38) Farnum, B. H.; Morseth, Z. A.; Lapides, A. M.; Rieth, A. J.; Hoertz, P. G.; Brennaman, M. K.; Papanikolas, J. M.; Meyer, T. J. *J. Am. Chem. Soc.* **2014,** *136*, 2208-2211.

(39) Song, W.; Luo, H.; Hanson, K.; Concepcion, J. J.; Brennaman, M. K.; Meyer, T. J. *Energy Environ. Sci.* **2013,** *6*, 1240-1248.

(40) Howard, I. A.; Meister, M.; Baumeier, B.; Wonneberger, H.; Pschirer, N.; Sens, R.; Bruder, I.; Li, C.; Müllen, K.; Andrienko, D.; Laquai, F. *Adv. Energy Mater.* **2014,** *4*, n/a-n/a.

(41) Berhe, S. A.; Gobeze, H. B.; Pokharel, S. D.; Park, E.; Youngblood, W. J. *ACS Appl. Mater. Interfaces* **2014,** *6*, 10696-10705.

(42) Meister, M.; Baumeier, B.; Pschirer, N.; Sens, R.; Bruder, I.; Laquai, F.; Andrienko, D.; Howard, I. A. *J. Phys. Chem. C* **2013,** *117*, 9171-9177.

(43) Oum, K.; Lohse, P. W.; Flender, O.; Klein, J. R.; Scholz, M.; Lenzer, T.; Du, J.; Oekermann, T. *Phys. Chem. Chem. Phys.* **2012,** *14*, 15429-15437.

(44) Oum, K.; Lohse, P. W.; Klein, J. R.; Flender, O.; Scholz, M.; Hagfeldt, A.; Boschloo, G.; Lenzer, T. *Phys. Chem. Chem. Phys.* **2013,** *15*, 3906-3916.

(45) Oum, K.; Flender, O.; Lohse, P. W.; Scholz, M.; Hagfeldt, A.; Boschloo, G.; Lenzer, T. *Phys. Chem. Chem. Phys.* **2014,** *16*, 8019-8029.

(46) Ardo, S.; Sun, Y.; Castellano, F. N.; Meyer, G. J. *J. Phys. Chem. B* **2010,** *114*, 14596-14604.

(47) Gregg, B. A. *Coord. Chem. Rev.* **2004,** *248*, 1215-1224.

(48) Schwarzburg, K.; Willig, F. *J. Phys. Chem. B* **1999,** *103*, 5743-5746.

(49) Kytin, V.; Dittrich, T.; Bisquert, J.; Lebedev, E. A.; Koch, F. *Phys. Rev. B* **2003,** *68*, 195308.

(50) Brus, L. *Phys. Rev. B* **1996,** *53*, 4649-4656.

(51) O'Donnell, R. M.; Ardo, S.; Meyer, G. J. *J. Phys. Chem. Lett.* **2013,** *4*, 2817-2821.

(52) Heimer, T. A.; D'Arcangelis, S. T.; Farzad, F.; Stipkala, J. M.; Meyer, G. J. *Inorg. Chem.* **1996,** *35*, 5319-5324.

(53) Trammell, S. A.; Meyer, T. J. *J. Phys. Chem. B* **1998,** *103*, 104-107.

(54) Argazzi, R.; Bignozzi, C. A.; Heimer, T. A.; Castellano, F. N.; Meyer, G. J. *Inorg. Chem.* **1994,** *33*, 5741-5749.

(55) Johansson, P. G.; Rowley, J. G.; Taheri, A.; Meyer, G. J.; Singh, S. P.; Islam, A.; Han, L. *Langmuir* **2011,** *27*, 14522-14531.

(56) Bergeron, B. V.; Kelly, C. A.; Meyer, G. J. *Langmuir* **2003,** *19*, 8389-8394.

(57) Pavlishchuk, V. V.; Addison, A. W. *Inorg. Chim. Acta* **2000,** *298*, 97-102.

(58) Rothenberger, G.; Fitzmaurice, D.; Grätzel, M. *J. Phys. Chem.* **1992,** *96*, 5983-5986.

(59) Duffy, N. W.; Peter, L. M.; Rajapakse, R. M. G.; Wijayantha, K. G. U. *Electrochem. Commun.* **2000,** *2*, 658-662.

(60) O'Regan, B. C.; Walley, K.; Juozapavicius, M.; Anderson, A.; Matar, F.; Ghaddar, T.; Zakeeruddin, S. M.; Klein, C. d.; Durrant, J. R. *J. Am. Chem. Soc.* **2009,** *131*, 3541-3548.

(61) Berger, T.; Anta, J. A.; Morales-Flórez, V. *J. Phys. Chem. C* **2012,** *116*, 11444-11455.

(62) Robson, K. C. D.; Hu, K.; Meyer, G. J.; Berlinguette, C. P. *J. Am. Chem. Soc.* **2013,** *135*, 1961-1971.

(63) Jonscher, A. K. *Nature* **1977,** *267*, 673-679.

(64) Bolts, J. M.; Wrighton, M. S. *J. Phys. Chem.* **1976,** *80*, 2641-2645.

(65) Lyon, L. A.; Hupp, J. T. *J. Phys. Chem. B* **1999,** *103*, 4623-4628.

(66) Redmond, G.; Fitzmaurice, D. *J. Phys. Chem.* **1993,** *97*, 1426-1430.

(67) Enright, B.; Redmond, G.; Fitzmaurice, D. *J. Phys. Chem.* **1994,** *98*, 6195-6200.

(68) Pelet, S.; Moser, J.-E.; Grätzel, M. *J. Phys. Chem. B* **2000,** *104*, 1791-1795.

(69) Kelly, C. A.; Farzad, F.; Thompson, D. W.; Stipkala, J. M.; Meyer, G. J. *Langmuir* **1999,** *15*, 7047-7054.

(70) Boschloo, G.; Fitzmaurice, D. *J. Phys. Chem. B* **1999,** *103*, 7860-7868.

(71) O'Regan, B.; Grätzel, M.; Fitzmaurice, D. *Chem. Phys. Lett.* **1991,** *183*, 89-93.

(72) Kay, A.; Humphry-Baker, R.; Grätzel, M. *J. Phys. Chem.* **1994,** *98*, 952-959.

(73) Norris, D. J.; Sacra, A.; Murray, C. B.; Bawendi, M. G. *Phys. Rev. Lett.* **1994,** *72*, 2612-2615.

(74) Szczepankiewicz, S. H.; Moss, J. A.; Hoffmann, M. R. *J. Phys. Chem. B* **2002,** *106*, 7654-7658.

(75) Burstein, E. *Phys. Rev.* **1954,** *93*, 632-633.

(76) Drago, R. S. *Physical Methods for Chemists, 2nd. Ed.* Saunders College Publishing: Philadelphia, 1992.

(77) Shannon, R. *Acta Crystallogr., Sect. A* **1976,** *32*, 751-767.

(78) Södergren, S.; Siegbahn, H.; Rensmo, H.; Lindström, H.; Hagfeldt, A.; Lindquist, S.-E. *J. Phys. Chem. B* **1997,** *101*, 3087-3090.

(79) Wagemaker, M.; Lützenkirchen-Hecht, D.; van Well, A. A.; Frahm, R. *J. Phys. Chem. B* **2004,** *108*, 12456-12464.

(80) Olson, C. L.; Nelson, J.; Islam, M. S. *J. Phys. Chem. B* **2006,** *110*, 9995-10001.

(81) Hengerer, R.; Kavan, L.; Krtil, P.; Grätzel, M. *J. Electrochem. Soc.* **2000,** *147*, 1467-1472.

(82) Krol, R. V. d.; Meulenkamp, E. A.; Goossens, A.; Schoonman, J. *MRS Online Proceedings Library* **1998,** *536*, 337-340.

(83) Ardo, S.; Achey, D.; Morris, A. J.; Abrahamsson, M.; Meyer, G. J. *J. Am. Chem. Soc.* **2011,** *133*, 16572-16580.

(84) Hu, K.; Robson, K. C. D.; Johansson, P. G.; Berlinguette, C. P.; Meyer, G. J. *J. Am. Chem. Soc.* **2012,** *134*, 8352-8355.

(85) Bisquert, J.; Fabregat-Santiago, F.; Mora-Seró, I.; Garcia-Belmonte, G.; Barea, E. M.; Palomares, E. *Inorg. Chim. Acta* **2008,** *361*, 684-698.

(86) Chidsey, C. E. D.; Murray, R. W. *J. Phys. Chem.* **1986,** *90*, 1479-1484.

(87) Johansson, P. G.; Kopecky, A.; Galoppini, E.; Meyer, G. J. *J. Am. Chem. Soc.* **2013,** *135*, 8331-8341.

(88) Kislenko, S. A.; Amirov, R. H.; Samoylov, I. S. *J. Phys. Chem. C* **2013,** *117*, 10589-10596.

(89) Wang, H.; He, J.; Boschloo, G.; Lindström, H.; Hagfeldt, A.; Lindquist, S.-E. *J. Phys. Chem. B* **2001,** *105*, 2529-2533.

(90) Wang, H.; Bell, J.; Desilvestro, J.; Bertoz, M.; Evans, G. *J. Phys. Chem. C* **2007,** *111*, 15125-15131.

(91) Wang, H.; Peter, L. M. *J. Phys. Chem. C* **2012,** *116*, 10468-10475.

(92) Fredin, K.; Nissfolk, J.; Boschloo, G.; Hagfeldt, A. *J. Electroanal. Chem.* **2007,** *609*, 55-60.

(93) Zhang, C.; Huang, Y.; Chen, S.; Tian, H.; Mo, L. e.; Hu, L.; Huo, Z.; Kong, F.; Ma, Y.; Dai, S. *J. Phys. Chem. C* **2012,** *116*, 19807-19813.

(94) Burdzinski, G.; Karolczak, J.; Ziolek, M. *Phys. Chem. Chem. Phys.* **2013,** *15*, 3889-3896.

(95) Hagfeldt, A.; Cappel, U. B.; Boschloo, G.; Sun, L.; Kloo, L.; Pettersson, H.; Gibson, E. A., Dye-Sensitized Photoelectrochemical Cells. In *Practical Handbook of Photovoltaics (Second Edition)*, Academic Press: Boston, 2012; pp 479-542.

(96) Cappel, U. B.; Smeigh, A. L.; Plogmaker, S.; Johansson, E. M. J.; Rensmo, H.; Hammarström, L.; Hagfeldt, A.; Boschloo, G. *J. Phys. Chem. C* **2011,** *115*, 4345-4358.

(97) Burdziński, G.; Karolczak, J.; Ziółek, M. *Phys. Chem. Chem. Phys.* **2013,** *15*, 3889.

(98) Krawczyk, S.; Zdyb, A. *J. Phys. Chem. C* **2011,** *115*, 22328-22335.

(99) Cappel, U. B. Characterisation of Organic Dyes for Solid State Dye-Sensitized Solar Cells. Ph.D. Dissertation, Uppsala University, Uppsala, Sweden, 2011.

(100) Meister, M.; Baumeier, B.; Pschirer, N.; Sens, R.; Bruder, I.; Laquai, F.; Andrienko, D.; Howard, I. A. *J. Phys. Chem. C* **2013**, 9171-9177.

(101) Bairu, S. G.; Mghanga, E.; Hasan, J.; Kola, S.; Rao, V. J.; Bhanuprakash, K.; Giribabu, L.; Wiederrecht, G. P.; da Silva, R.; Rego, L. G. C.; Ramakrishna, G. *J. Phys. Chem. C* **2013,** *117*, 4824-4835.

(102) Pastore, M.; Angelis, F. D. *J. Phys. Chem. Lett.* **2011,** *2*, 1261-1267.

(103) Waskasi, M. M.; Hashemianzadeh, S. M.; Sarhangi, O. M. *Comp. Theor. Chem.* **2011,** *978*, 33-40.

(104) Stark, J. *Nature* **1913,** *92*, 401.

(105) Hampden-Smith, M. J.; Williams, D. S.; Rheingold, A. L. *Inorg. Chem.* **1990,** *29*, 4076-4081.

(106) Shannon, R. D. *Acta Crystallogr., Sect. A: Found. Crystallogr.* **1976,** *32*, 751-767.

(107) Haque, S. A.; Tachibana, Y.; Willis, R. L.; Moser, J. E.; Grätzel, M.; Klug, D. R.; Durrant, J. R. *J. Phys. Chem. B* **1999,** *104*, 538-547.

(108) Rothenberger, G.; Fitzmaurice, D.; Graetzel, M. *J. Phys. Chem.* **1992,** *96*, 5983-5986.

(109) Colvin, V. L.; Alivisatos, A. P. *J. Chem. Phys.* **1992,** *97*, 730-433.

(110) Lawless, D.; Luangdilok, C.; Cook, A. R.; Meisel, D. In *Dynamic Electric Field Effects in Small Semiconductor Particles*, Proceedings of the Symposium on Nanostructured Materials in Electrochemistry, Reno, Nevada, May 21st - 26th, 1995; Searson, P. C.; Meyer, G. J., Eds. The Electrochemical Society: Reno, Nevada, 1995; p 61.

(111) Keldysh, L. V. *Sov. Phys. JETP* **1965,** *20*, 1307-1314.

(112) Pankove, J. I. *Optical Processes in Semiconductors*. Dover Publications: New York, 1975.

(113) Rowley, J. G.; Farnum, B. H.; Ardo, S.; Meyer, G. J. *J. Phys. Chem. Lett.* **2010,** *1*, 3132-3140.

(114) Jonscher, A. K. *Nature* **1977,** *267*, 673-679.

(115) Lyon, L. A.; Hupp, J. T. *J. Phys. Chem. C* **1999,** *103*, 4623-4628.

(116) Snaith, H. J.; Petrozza, A.; Ito, S.; Miura, H.; Grätzel, M. *Adv. Funct. Mater.* **2009,** *19*, 1810-1818.

Chapter 4. Electric Fields Control $TiO_2(e^-) + I_3^- \rightarrow$ Charge Recombination in Dye-Sensitized Solar Cells

In part a compilation of one publication.[1]

This work was collaborative in conjunction with Renato N. Sampaio[†‡] *and*
Timothy J. Barr[†]
[†]*Johns Hopkins University, Baltimore, Maryland*
[‡]*Federal University of Uberlândia, Uberlândia, Brazil*

4.1 Introduction

Electrons injected into the mesoporous TiO_2 nanocrystalline (anatase) thin films commonly used in dye-sensitized solar cells (DSSCs) generate an electric field that significantly perturbs the absorption spectra of the dye molecules anchored to its surface. The electro-absorption signature, similar to that observed in Stark spectroscopy, and the >1 MV/cm electric field magnitude were only recently discovered and a full appreciation of how the presence of this field might be exploited for practical applications remains uncertain.[2-3] The electro-absorption signature appears as a first-derivative of the ground state absorption that has proven to be a valuable experimental tool for the characterization of dye-sensitized TiO_2 interfaces.[4-8] Indeed, insight into the relative orientation of the molecular dipole as well as the dye-semiconductor distance has been revealed through systematic studies with different dye molecules.[3,9] In addition, pulsed laser excitation has permitted the dynamics for charge screening by the electrolyte to be quantified on microsecond and longer time scales.[10-12] Yet in spite of these advances in fundamental science, there is no clear indication that these electric fields have any practical relevance to the light-driven electron transfer reactions that promote or inhibit electrical power generation in DSSCs. One would reasonably anticipate that the surface electric field would repel anions like tri-iodide and hence inhibit the unwanted charge recombination reaction with electrons injected into TiO_2. However, there was been no compelling evidence that the anionic nature of these redox mediators is at all relevant to operational DSSCs prior to the results presented in this chapter.

4.2 Results and Discussion

Mesoporous TiO_2 thin films were sensitized to visible light by $[Ru(dtb)_2(dcb)](PF_6)_2$, where dtb is 4,4′-(*tert*-butyl)$_2$-2,2′-bipyridine and dcb is 2,2’-bipyridine-4,4’-dicarboxylic acid, abbreviated $Ru(dtb)_2(dcb)/TiO_2$. Figure 4.1 shows the visible absorption spectra of a $Ru(dtb)_2(dcb)/TiO_2$ thin film immersed in neat acetonitrile and in acetonitrile solutions that contain 100 mM iodide with Li^+, Na^+, Mg^{2+}, or Ca^{2+} cations. The extinction coefficients were calculated relative to $Ru(dtb)_2(dcb)/TiO_2$ in CH_3CN which was assumed to have the same value as the $[Ru(dtb)_2(dcb)](PF_6)_2$ dissolved in CH_3CN. A significant red shift in the metal-to-ligand charge-transfer (MLCT) absorption was observed in the electrolyte solutions relative to neat CH_3CN as well as a small decrease in the maximum absorption intensity. The magnitude of the red shift increased in the order $Na^+ < Li^+ < Mg^{2+} \approx Ca^{2+}$. This data with the iodide salts are in excellent agreement with that previously reported for the perchlorate salts which is consistent with the proposal that adsorption of these Lewis acidic cations to TiO_2 induces the spectral shifts with negligible contributions from the anions.[11]

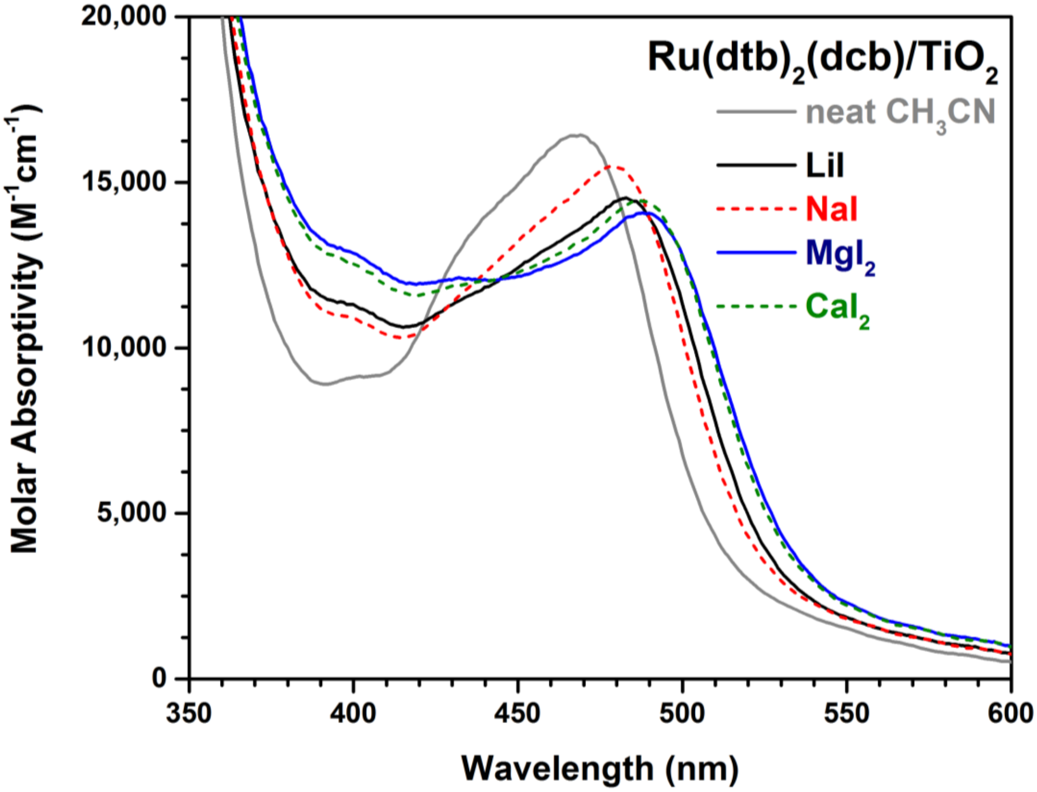

Figure 4.1. Visible absorbance spectra of a $Ru(dtb)_2(dcb)/TiO_2$ thin film immersed in acetonitrile in the absence (grey) or presence of 100 mM LiI (black), 100 mM NaI (red), 50 mM MgI_2 (blue) and 50 mM CaI_2 (green).

Partial electrochemical reduction of the sensitized TiO_2 thin films in a standard three-electrode cell, results in a blue-shift of the MLCT absorption as has been previously described.[2,11] Figure 4.2.A. shows such data as difference spectra where the absorption spectra of the reduced film are subtracted from the initial spectrum under conditions where about 20 electrons were present in each TiO_2 nanocrystallite.

Pulsed laser excitation of the $Ru(dtb)_2(dcb)/TiO_2$ thin films immersed in the iodide acetonitrile electrolytes gave rise to significant absorption changes that were monitored on nanosecond and longer time scales. Light absorption by the Ru sensitizer resulted in rapid excited state injection and sensitizer regeneration through iodide oxidation that were complete within a microsecond. The oxidation of iodide to tri-iodide in DSSCs is known to occur through disproportionation of an $I_2^{\cdot -}$ intermediate. Disproportionation within the mesopores of TiO_2 occurs with the same rate constant as in fluid solution, $k = 3 \times 10^9$ $M^{-1}s^{-1}$.[13] Hence only the injected electrons and tri-iodide were expected to appreciably absorb light in the visible region on time scales greater than a microsecond. Shown in Figure 4.2.B. are representative spectra recorded 2.5 μs after laser excitation of the $Ru(dtb)_2(dcb)/TiO_2$ in acetonitrile electrolytes that represented the extremes that were observed, 100 mM NaI or 50 mM CaI_2. The characteristic absorption of I_3^- at ~ 360 nm and the weak absorption of the injected electrons at 600 nm were evident.[14]

The large first-derivative feature between ~450 and 550 nm arises from a unidirectional shift of the ground state absorption spectra induced by the injected electrons. In other words, the electrons injected into TiO_2 generate an electric field that significantly blue shifts the MLCT absorption of the ruthenium compounds anchored to the surface.[2] The magnitude of the intensity change as well as the spectral shift were significantly more pronounced when Ca^{2+} containing electrolytes were employed, behavior attributed to less effective screening of the electric field from the sensitizer. The field strengths were found to follow the order: $Na^+ < Li^+ < Mg^{2+} < Ca^{2+}$.[11] The electric field strength reported by the Ru sensitizers was 1.1 MV/cm for Na^+ and 2.2 MV/cm for Ca^{2+} with the magnitude of the electric fields calculated using previously reported methods and assumptions.[2,11,15-16] Since the same number of TiO_2 electrons was held constant, the different field strengths were attributed to the ability of the cations to screen the field from the surface anchored sensitizers.

Shown in Figure 4.3. are absorption changes monitored at 375 nm. This observation wavelength was chosen as the I_3^- anion absorbs strongly there and it represents an isosbestic point between $I_2^{\cdot -}$ and I_3^-.[13] As a result, the concentration of I_3^- can be uniquely probed at this wavelength. The non-exponential kinetics were well described by the Kohlrausch−Williams−Watts (KWW) model, Equation (4.1)

$$I(t) = I_0 exp\left[-(kt)^{\beta}\right] \tag{4.1}$$

Here β is inversely related to the width of an underlying Lévy distribution of rate constants, $0 < \beta < 1$, and *k* is a characteristic rate constant. In kinetic analysis, the value of β was fixed to be 0.45 and *k* was allowed to float. An ‘average’ rate constant was calculated as the first moment of this distribution using Equation (4.2), data given in Table 4.1.

$$k_{KWW} = \frac{k\beta}{\Gamma\left(\frac{1}{\beta}\right)} \tag{4.2}$$

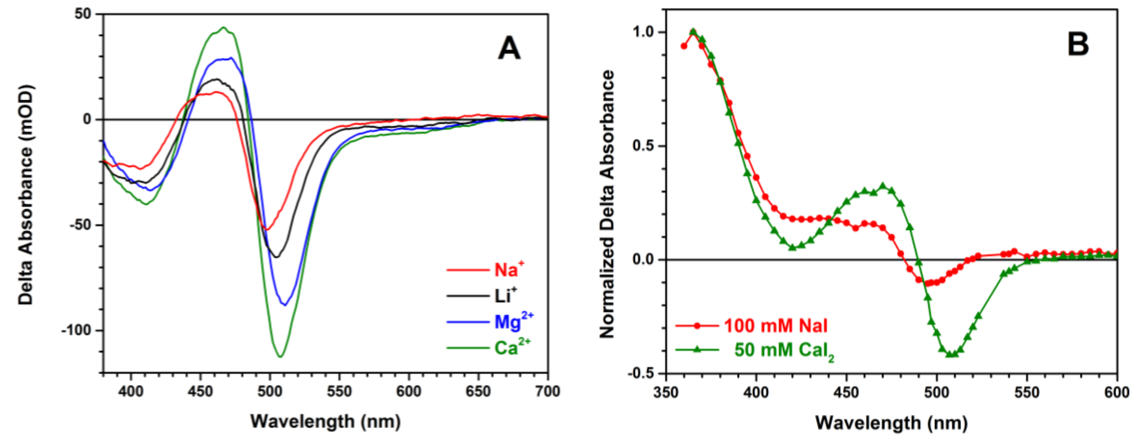

Figure 4.2. Absorbance change of Ru(dtb)$_2$(dcb)/TiO$_2$ thin films measured: A) under conditions of approximately 20 TiO$_2$(e$^-$)s per TiO$_2$ nanoparticle electrochemically generated in 100 mM solutions of NaClO$_4$ (red), LiClO$_4$ (black), Mg(ClO$_4$)$_2$ (blue) and Ca(ClO$_4$)$_2$ (green) and B) 2.5 μs after pulsed 532 nm light excitation in 100 mM NaI (red, circles) and 50 mM CaI$_2$ (green, triangles) acetonitrile solutions.

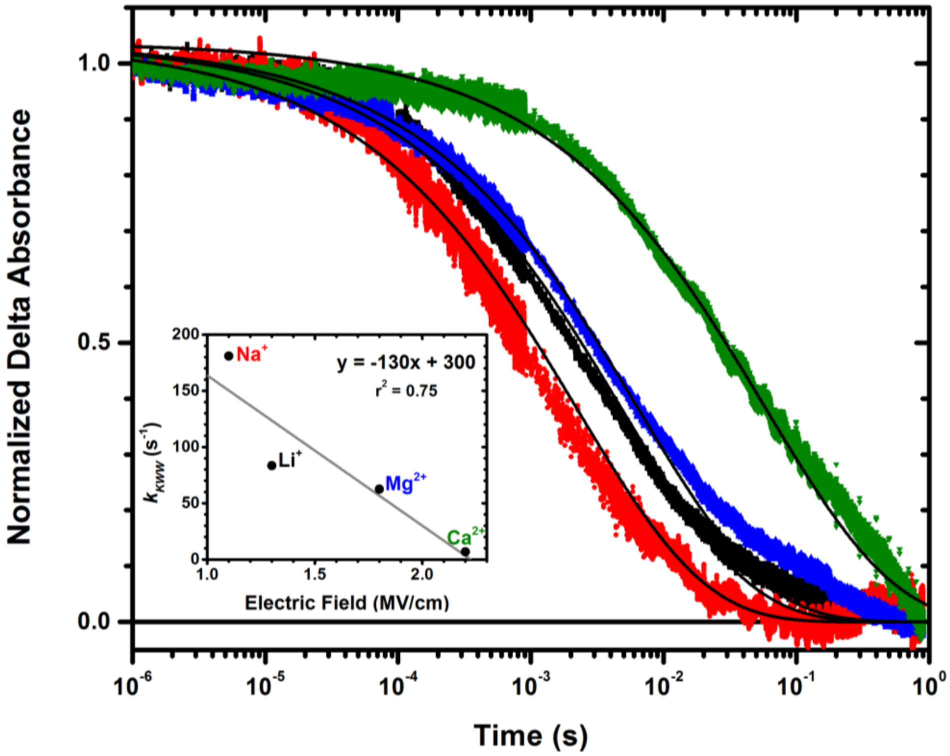

Figure 4.3. Absorption changes that correspond to $TiO_2(e^-) + I_3^-$ → charge recombination measured in 100 mM $LiClO_4$ (black), $NaClO_4$ (red), $Mg(ClO_4)_2$ (blue) and mM $Ca(ClO_4)_2$ (green) acetonitrile solutions with 250 mM TBAI. Overlaid on the data are fits to the KWW function with $\beta = 0.45$. The inset shows a plot of the recombination rate constant versus the electric field.

Table 4.1. $TiO_2(e^-) + I_3^-$ → Charge Recombination with the Indicated Cations

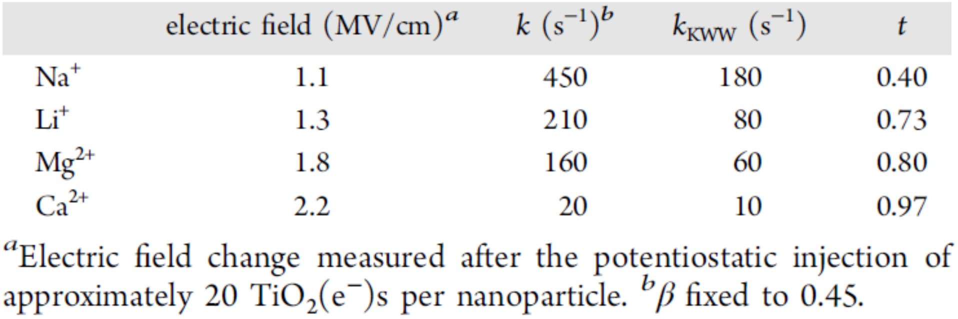

	electric field (MV/cm)[a]	k (s^{-1})[b]	k_{KWW} (s^{-1})	t
Na^+	1.1	450	180	0.40
Li^+	1.3	210	80	0.73
Mg^{2+}	1.8	160	60	0.80
Ca^{2+}	2.2	20	10	0.97

[a] Electric field change measured after the potentiostatic injection of approximately 20 $TiO_2(e^-)$s per nanoparticle. [b] β fixed to 0.45.

The inset of Figure 4.3. is a plot of the recombination rate constant versus the electric field. This and the raw experimental data clearly show a marked electric field dependence for the unwanted $TiO_2(e^-) + I_3^- \rightarrow$ charge recombination rate constant. This correlation provides compelling evidence that *the larger the electric field - the slower the unwanted charge recombination reaction with* I_3^-. Recall that I_3^- is generated within the mesopores after the disproportionation of two $I_2^{\cdot -}$ ions. Mass transfer of I_3^- by both diffusion and migration to the TiO_2 surface must then occur before recombination is possible. Extrapolation of the best fit line to zero electric field provides an estimate of the diffusional contributions to the recombination reaction that occurs in the absence of an electric field, $k = 300\ s^{-1}$. Since rate constants are proportional to current, the total current at zero field is the diffusional current, $i_0 = i_d$. The rate constants decrease when electrons are injected into TiO_2, because the anionic charge of the I_3^- is repelled by the field generated by the $TiO_2(e^-)$s. Hence, the total current decreases in the presence of the field due to migration of I_3^- away from the TiO_2 interface, $i = i_d - i_m$. The ratio of the average rate constant measured in the presence of the field to that in the absence has some analogy to transference coefficients, $t = i/i_0$, that have been quantified in electrochemical cells.[17] Here t represents the fractional ability of the electric field to block the unwanted $TiO_2(e^-) + I_3^- \rightarrow$ charge recombination reaction. The t values are given in Table 4.1. One way to visualize the repulsive nature of the electric field on the negatively charged I_3^- is by calculating the concentration profile of I_3^- at the interface compared to the bulk concentration using the Gouy-Chapman Model, Equation (4.3):

$$\frac{[I_3^-]_{Interface}}{[I_3^-]_{Bulk}} = \tanh^2\left[\frac{1}{2}\left(\frac{x}{\lambda} - \ln\left(\tanh\left(-\frac{\theta_0}{2}\right)\right)\right)\right] \tag{4.3}$$

where $\theta_0 = \frac{zF\phi_0}{2RT}$ and ϕ_0 is the potential drop across the interface due to the electric field. The potential drops were calculated for the four cations studied using electric field values reported previously and a distance of either 5 or 10 Å based off of the crystal structure of $[Ru(dtb)_2(dcbH_2)]^{2+}$, Figure 4.4; for instance $\phi_0(Li^+) = 1.1\ \frac{MV}{cm} \times 5\text{Å} = 55\ mV$.[1,17] Triiodide concentration profiles as a function of distance from the electrode interface are shown in Figure 4.5 resulting from the interfacial electric fields generated in the presence of the four Lewis acidic cations.

It should be pointed out that other iodine species may also accept electrons in DSSCs. Indeed there exists compelling evidence that molecular iodine I_2, is reduced by $TiO_2(e^-)$s. As tri-iodide and molecular iodine are in equilibrium, Equation (4.4), both are always present in solution.[18] However, under the current experimental conditions, iodide was the only species present before laser excitation and the concentrations of I_3^- generated with light was on the order of 10 μM rendering the equilibrium concentration of I_2 negligibly small. Hence, the present study has effectively stacked the deck to ensure that recombination occurs predominantly to tri-iodide. This differs from an operational dye-sensitized solar cell where a mixture of 0.5 M LiI and 0.05 M I_2 in an acetonitrile solution is typically utilized.

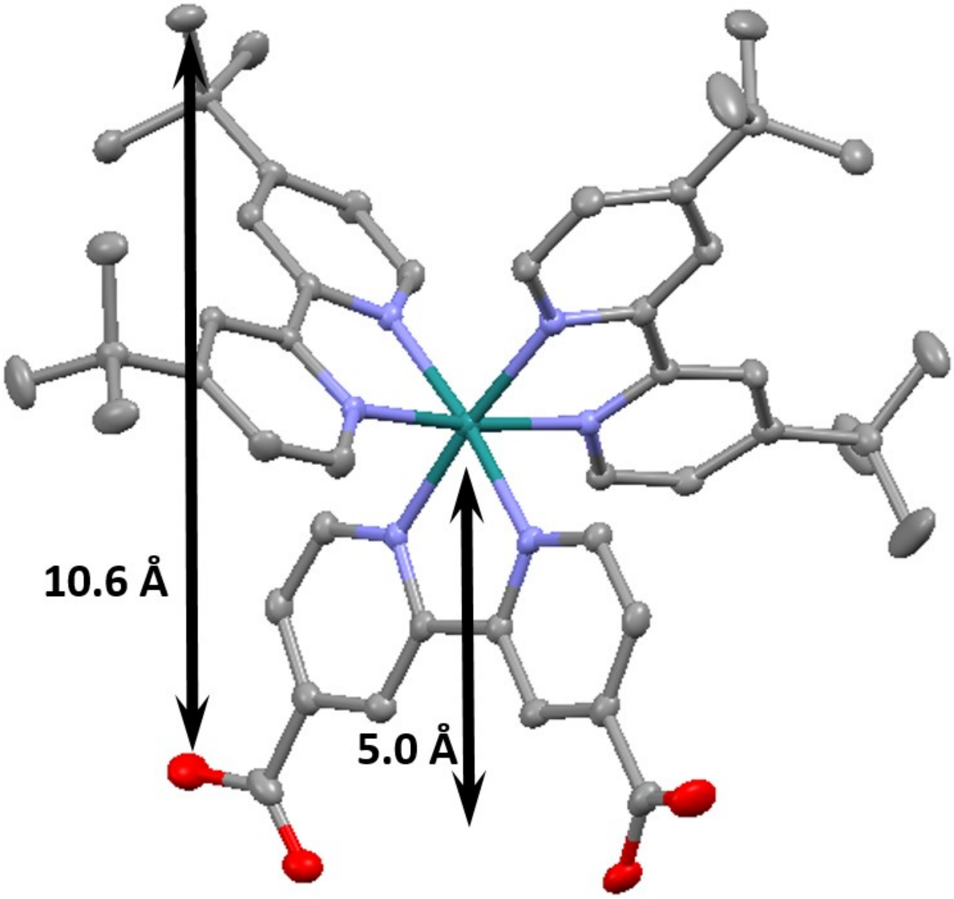

Figure 4.4. Crystal structure of $[Ru(dtb)_2(dcbH_2)]^{2+}$ with measured distances indicated.

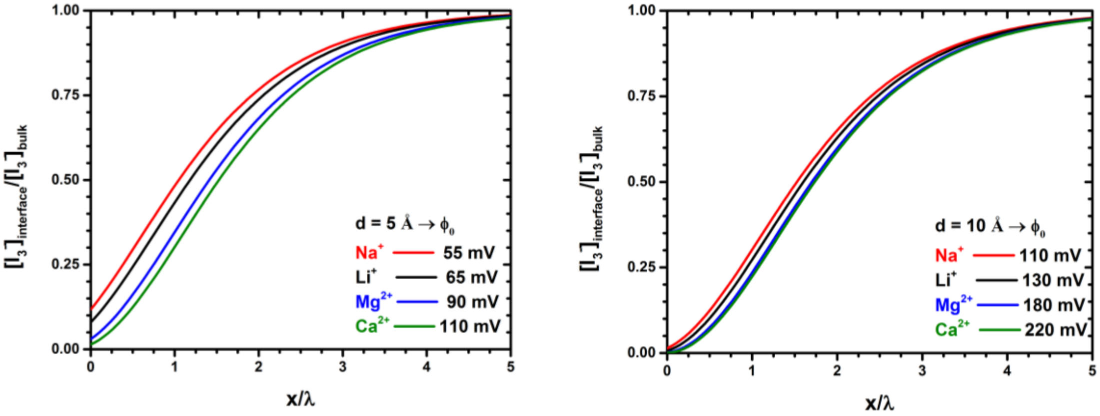

Figure 4.5. Concentration profiles of triiodide as a function of distance from the TiO_2 interface resulting from the electric field in the presence of the Lewis acidic cations modeled with a 5 Å (left) or 10 Å (right) potential drop at the interface.

The equilibrium constant for Reaction (4.4) has been estimated to be $K_{eq} = 10^6$ indicates that equilibrium concentrations are 0.45 M I^-, 0.05 M I_3^-, and 2 μM I_2.[14]

$$I_2 + I^- \rightleftharpoons I_3^- \tag{4.4}$$

It should also be emphasized that changing the cations in the electrolytes of DSSCs influences many parameters including the transport of the injected electrons,[19-21] dye regeneration,[22] and the energy levels of the TiO_2 acceptor states.[11,23-24] Nevertheless, the implications of the results presented herein to DSSCs are clear and significant. Akin to enlarging the space-charge layer thickness in single semiconductor solar cells, increasing the Debye length for charge screening supports more spatially separated and longer-lived $TiO_2(e^-)$, I_3^- donor-acceptor pairs. Hence screening of the electric field by these alkali and alkaline earth cations in the electrolyte is detrimental to the solar conversion efficiency. This is particularly important at the power point and open circuit conditions where the number of electrons is large and the $TiO_2(e^-)$s may be capable of accessing the two-electron reduction of I_3^-, $E^0(I_3^-/3I^-) = 0.35$ V, which is much more favorable than the one-electron reduction potential, $E^0(I_3^-/I_2^{\cdot -},I^-) = -0.35$ V vs. NHE.[14] Interestingly, complete screening of the electric field should instead be beneficial for the cationic Co(III/II) redox mediators, i.e.$[Co(bpy)_3]^{3+/2+}$, employed in champion DSSCs;[25] since migration will enhance the mass transfer of Co(III) to the interface where recombination with injected electrons occurs.

4.3 References

(1) O'Donnell, R. M.; Sampaio, R. N.; Barr, T. J.; Meyer, G. J. *J. Phys. Chem. C* **2014,** *118*, 16976-16986.

(2) Ardo, S.; Sun, Y.; Staniszewski, A.; Castellano, F. N.; Meyer, G. J. *J. Am. Chem. Soc.* **2010,** *132*, 6696-6709.

(3) Cappel, U. B.; Feldt, S. M.; Schöneboom, J.; Hagfeldt, A.; Boschloo, G. *J. Am. Chem. Soc.* **2010,** *132*, 9096-9101.

(4) Burdzinski, G.; Karolczak, J.; Ziolek, M. *Phys. Chem. Chem. Phys.* **2013,** *15*, 3889-3896.

(5) Farnum, B. H.; Morseth, Z. A.; Lapides, A. M.; Rieth, A. J.; Hoertz, P. G.; Brennaman, M. K.; Papanikolas, J. M.; Meyer, T. J. *J. Am. Chem. Soc.* **2014,** *136*, 2208-2211.

(6) Bairu, S. G.; Mghanga, E.; Hasan, J.; Kola, S.; Rao, V. J.; Bhanuprakash, K.; Giribabu, L.; Wiederrecht, G. P.; da Silva, R.; Rego, L. G. C.; Ramakrishna, G. *J. Phys. Chem. C* **2013,** *117*, 4824-4835.

(7) Meister, M.; Baumeier, B.; Pschirer, N.; Sens, R.; Bruder, I.; Laquai, F.; Andrienko, D.; Howard, I. A. *The Journal of Physical Chemistry C* **2013,** *117*, 9171-9177.

(8) Oum, K.; Flender, O.; Lohse, P. W.; Scholz, M.; Hagfeldt, A.; Boschloo, G.; Lenzer, T. *Phys. Chem. Chem. Phys.* **2014,** *16*, 8019-8029.

(9) Johansson, P. G.; Kopecky, A.; Galoppini, E.; Meyer, G. J. *J. Am. Chem. Soc.* **2013,** *135*, 8331-8341.

(10) O'Donnell, R. M.; Ardo, S.; Meyer, G. J. *J. Phys. Chem. Lett.* **2013,** *4*, 2817-2821.

(11) O'Donnell, R. M.; Sampaio, R. N.; Barr, T. J.; Meyer, G. J. *J. Phys. Chem. C* **2014**.

(12) Song, W.; Luo, H.; Hanson, K.; Concepcion, J. J.; Brennaman, M. K.; Meyer, T. J. *Energy Environ. Sci.* **2013,** *6*, 1240-1248.

(13) Rowley, J. G.; Meyer, G. J. *J. Phys. Chem. C* **2011,** *115*, 6156-6161.

(14) Rowley, J. G.; Farnum, B. H.; Ardo, S.; Meyer, G. J. *J. Phys. Chem. Lett.* **2010,** *1*, 3132-3140.

(15) Oh, D. H.; Boxer, S. G. *J. Am. Chem. Soc.* **1989,** *111*, 1130-1131.

(16) Ardo, S.; Sun, Y.; Castellano, F. N.; Meyer, G. J. *J. Phys. Chem. B* **2010,** *114*, 14596-14604.

(17) Bard, A. J.; Faulkner, L. R. *Electrochemical Methods: Fundamentals and Applications*. 2nd ed.; John Wiley & Sons: Hoboken, NJ, 2001; p 66-68, 137-143.

(18) Richards, C. E.; Anderson, A. Y.; Martiniani, S.; Law, C.; O'Regan, B. C. *J. Phys. Chem. Lett.* **2012,** *3*, 1980-1984.

(19) Kambe, S.; Nakade, S.; Kitamura, T.; Wada, Y.; Yanagida, S. *J. Phys. Chem. B* **2002,** *106*, 2967-2972.

(20) Wang, H.; Bell, J.; Desilvestro, J.; Bertoz, M.; Evans, G. *J. Phys. Chem. C* **2007,** *111*, 15125-15131.

(21) Wang, H.; Peter, L. M. *J. Phys. Chem. C* **2012,** *116*, 10468-10475.

(22) Pelet, S.; Moser, J.-E.; Grätzel, M. *J. Phys. Chem. B* **2000,** *104*, 1791-1795.

(23) Kelly, C. A.; Farzad, F.; Thompson, D. W.; Stipkala, J. M.; Meyer, G. J. *Langmuir* **1999,** *15*, 7047-7054.

(24) Redmond, G.; Fitzmaurice, D. *J. Phys. Chem.* **1993,** *97*, 1426-1430.

(25) Mathew, S.; Yella, A.; Gao, P.; Humphry-Baker, R.; CurchodBasile, F. E.; Ashari-Astani, N.; Tavernelli, I.; Rothlisberger, U.; NazeeruddinMd, K.; Grätzel, M. *Nat. Chem.* **2014,** *6*, 242-247.

Chapter 5. Reversal of the Excited State Acid-Base Behavior of Ruthenium Polypyridyl Compounds Containing Carboxylic Acids Through Ancillary Ligand Modification

5.1 Introduction

Compounds with protonatable functional groups can exhibit excited state acid-base behavior that differs significantly from that of their ground state. The increased basicity or acidity in the excited state is commonly attributed to a redistribution of electron density.[1-2] Organic molecules and transition metal compounds that possess these properties have been exploited for use as pH sensors.[3-9] They have also been used to study proton coupled electron transfer (PCET) reactions which are of biological relevance and significant for understanding processes important to solar energy conversion such as water oxidation.[10-11]

The square scheme in Figure 5.1 depicts the different states accessible to compounds that undergo acid-base chemistry starting with the ground-state equilibrium, K_a, between the acidic, H-A, and basic, B, forms. Light excitation of the acid form can generate an excited state, H-A*, that relaxes back to the ground state via radiative and non-radiative decay pathways, k_A. Under appropriate conditions, H-A* can convert into the deprotonated form, B*, based on the excited state acid-base equilibrium dictated by the deprotonation, k_{AB}, and protonation, k_{BA}, rates of the excited states.[1,8]

Several research groups have reported excited state acid-base chemistry of ruthenium polypyridyl compounds following the first report in 1977 by Wrighton and coworkers on $[Ru(bpy)_2(dcbH_2)]^{2+}$, where bpy is 2,2’-bipyridine and dcb is 2,2’-bipyridine-4,4’-dicarboxylic acid.[12] The majority of ruthenium compounds generate excited states with increased basicity compared to their ground states, particularly for compounds containing polypyridine ligands derivatized with carboxylic acids[13-17] or pendant amines.[18-20] In contrast, ruthenium polypyridine compounds that exhibit increased acidity in the excited state are relatively rare and contain hydroxy groups[21] or cyanide ligands.[22]

In this chapter, the excited state acid-base properties of two ruthenium polypyridyl compounds containing carboxylic acid derivatized bipyridine ligands will be presented. The compound $[Ru^{II}(btfmb)_2(dcbH_2)]^{2+}$, where btfmb is 4,4’-bis(trifluoromethyl)-2,2’-bipyridine, differs from $[Ru^{II}(dtb)_2(dcbH_2)]^{2+}$, where dtb is 4,4’-di-*tert*-butyl-2,2’-bipyridine, in that its ancillary ligand, btfmb, contains electron-withdrawing trifluoromethyl groups compared to the electron-donating tert-butyl groups of the dtb ligand, Figure 5.2. The presented research indicates that this ligand modification ultimately affects the location of the electron in the excited state. These changes in the electron density of the excited state result in a reversal of the excited state acid-base properties between the two compounds.

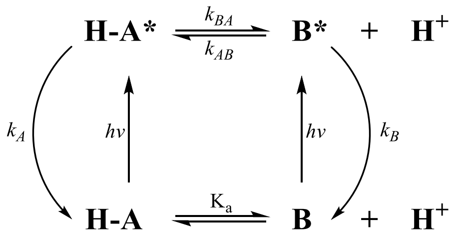

Figure 5.1. Square scheme for ground and excited-state acid-base chemistry of a compound.

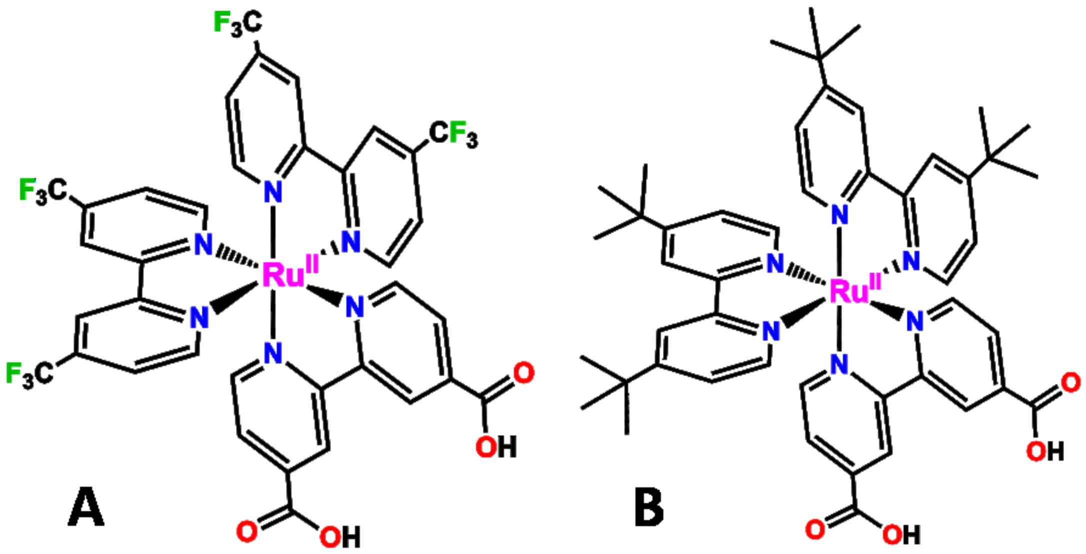

Figure 5.2. Chemical structures of $[Ru^{II}(btfmb)_2(dcbH_2)]^{2+}$, A, and $[Ru^{II}(dtb)_2(dcbH_2)]^{2+}$, B.

5.2 Experimental

5.2.1 Materials

All chemicals were reagent grade or better unless otherwise specified and were used without further purification. The following reagents were used as received from the following commercial suppliers: acetonitrile (Burdick & Jackson, spectrophotometric grade); deionized water; diethyl ether (Fisher); ethanol (Fisher); N,N-dimethylformamide (Fisher); perchloric acid ($HClO_4$; Aldrich 99.999% trace metals analysis); *n*-tetrabutylammonium hydroxide (TBAOH; Sigma-Aldrich, 1.0 M in methanol); triethylamine (Fluka, 99.5%); silver nitrate (Sigma-Aldrich, 99%); $[Ru(bpy)_3]Cl_2{\cdot}6H_2O$ (Aldrich, 99.95%); argon gas (Airgas, >99.998%); and nitrogen gas (Airgas, 99.999%).

5.2.2 Preparations.

4,4’-bis(trifluoromethyl)-2,2’-bipyridine (btfmb), 4,4’-diethylester-2,2’-bipyridine (deeb), [Ru(*p*-cymene)(deeb)Cl]Cl, and $[Ru(dtb)_2(dcbH_2)](PF_6)_2$ were synthesized according to literature procedures.[23-27]

$[Ru(btfmb)_2(deeb)](NO_3)_2$. [Ru(*p*-cymene)(deeb)Cl]Cl (192 mg, 0.32 mmol), btfmb (187 mg, 0.64 mmol) and 2.2 equivalents of silver nitrate (120 mg, 0.71 mmol) were refluxed in 20 mL of ethanol under argon atmosphere in the dark for 18 hours in a 50 mL round bottom flask. After the reaction mixture cooled to room temperature, the mixture was filtered under vacuum and the filtrate was collected. The filtrate was evaporated to dryness under reduced pressure and further dried in a vacuum oven at 100°C for 1 hour to afford 308 mg of red powder. Yield = 88%. ^1H NMR (CD_3CN, 400 MHz): δ 9.08 (s, 2H), 8.97 (s, 4H), 8.00 (d, 2H, $J = 5.9$ Hz), 7.95 (d, 2H, $J = 5.9$ Hz), 7.91 (d, 2H, $J = 5.8$ Hz), 7.85 (d, 2H, *J* = 6.0 Hz), 7.73 (d, 2H, *J* = 6.0 Hz), 7.69 (d, 2H, *J* = 6.0 Hz), 4.47 (q, 4H, *J* = 14.2, 7.1 Hz), 1.41 (t, 6H, *J* = 14.2, 7.1 Hz),

[Ru(btfmb)$_2$(dcbH$_2$)](NO$_3$)$_2$. A solution containing [Ru(btfmb)$_2$(deeb)](NO$_3$)$_2$ (72 mg, 0.065 mmol), 1 mL of water, 1 mL of triethylamine, and 3 mL of N,N-dimethylformamide was refluxed under argon atmosphere for 18 hours in a 10 mL round bottom flask. After cooling to room temperature, the solvent volume was reduced under reduced pressure. The reaction mixture was transferred to a 100 mL round bottom flask and 70 mL of diethyl ether was added to precipitate the product. The orange precipitate was collected on a fine frit, washed with cold diethyl ether (3 x 15 mL) and dried at 100°C in a vacuum oven for 2 hours to afford 42 mg of orange powder. Yield = 61%. ^{1}H NMR (D$_2$O, 400 MHz): δ 8.99 (s, 4H), 8.97 (s, 2H), 8.08 (d, 2H, *J* = 5.8 Hz), 8.05 (d, 2H, *J* = 5.9 Hz), 7.84 (d, 2H, *J* = 5.8 Hz), 7.77 (m, 6H).

5.2.3 Spectroscopy.

NMR. ^{1}H-NMR spectra were recorded using a Bruker Avance^{III} 400 MHz spectrometer and referenced to the residual solvent peaks.

UV-Visible Absorption. Steady-state UV-visible (vis) absorption spectra were obtained on a Varian Cary 50 or an Agilent Cary 60 spectrophotometer at room temperature in 1.0 cm path length quartz cuvettes. The solutions were deaerated with argon gas for a minimum of 30 minutes prior to photoluminescence and transient absorption studies, unless specified.

Photoluminescence. Steady-state photoluminescence spectra were obtained with an ISS K2 spectrophotometer equipped with a 75 W Xe arc lamp for the excitation source. PL spectra were obtained at room temperature with PL detected at a right angle to the excitation beam. Quantum yields were measured versus $[Ru(bpy)_3^{2+}]Cl_2$ in water as the standard ($\Phi_{PL} = 0.042$) using the optically dilute method.[28] Nanosecond time-resolved PL data were acquired at a right angle to excitation with pulsed 450 nm laser light from a N_2 dye laser (Photon Technologies International, GL301, Coumarin 450 (Exciton)). Transient data were digitized on a computer-interfaced oscilloscope (LeCroy LT322) with 5 ns time resolution. Typically, 300 laser shots were averaged for each kinetic trace.

pH Titrations. pH dependent absorption and PL spectra were obtained open to atmosphere with the pH monitored *in situ* using an Oakton pH 11 meter (Cole Parmer).

Transient Absorption. Nanosecond transient absorption measurements were obtained with an apparatus similar to that which has been previously described in the literature.[29] Briefly, samples were excited by a Q-switched, pulsed Nd:YAG laser (Quantel U.S.A. (BigSky) Brilliant B; 5-6 ns full width at half-maximum (fwhm), 1 Hz, ~10 mm in diameter) tuned to 532 nm with the appropriate nonlinear optics. The excitation fluence was measured by a thermopile power meter (Molectron) and was typically 3 – 5 mJ/pulse. A 150 W Xe arc lamp served as the probe beam and was aligned orthogonal to the laser excitation light. The lamp was pulsed with 100 V for detection at sub-100 μs time scales. Detection was achieved with a monochromator (SPEX 1702/04) optically coupled to an R928 photomultiplier tube (Hamamatsu). Appropriate glass filters were positioned between the probe lamp/sample and the sample/detection monochromator. Transient data was acquired with a computer-interfaced digital oscilloscope (LeCroy 9450, Dual 330 MHz) with an overall instrument response time of ~10 ns. Typically, 30 laser pulses were averaged at each observation wavelength over the range 340 – 750 nm at 10 nm intervals.

Full spectra were generated by averaging 2 – 10 points on either side of the desired time value to reduce noise in the raw data.

5.2.4 Data Fitting.

Kinetic data fitting and Arrhenius analyses were performed in Origin 9.0 with least-squares error minimization accomplished using the Levenberg-Marquardt iteration method. Excited state lifetimes, τ, were fit to single exponential decay kinetics over at least three half-lives, Equation (2.1):

$$I(t) = I_0 exp\left(\frac{-t}{\tau}\right) \tag{5.1}$$

5.3 Results

The neutral compound $[Ru^{II}(btfmb)_2(dcb^{2-})]^0$ exhibited a broad metal-to-ligand charge transfer (MLCT) absorption band centered around 460 nm and a ligand-centered transition at 296 nm when dissolved in water with pH greater than 5.0. Titration of the solution with $HClO_4$ led to an increase in intensity of the MLCT absorption band that also sharpened, see Figure 5.3.A. The neutral $[Ru^{II}(dtb)_2(dcb^{2-})]^0$ compound, where dtb is 4,4’-di-*tert*-butyl-2,2’-bipyridine, exhibited similar UV-Vis absorption characteristics when dissolved in water with pH greater than 5.5. A broad MLCT absorption band centered at 455 nm and a ligand-centered transition at 287 nm were observed. Contrary to the behavior observed for the btfmb compound, when $HClO_4$ was added to the dtb compound in aqueous solution, the MLCT absorption band split into two distinct bands with maxima at 430 and 480 nm and decreased in intensity, shown in Figure 5.3.B.

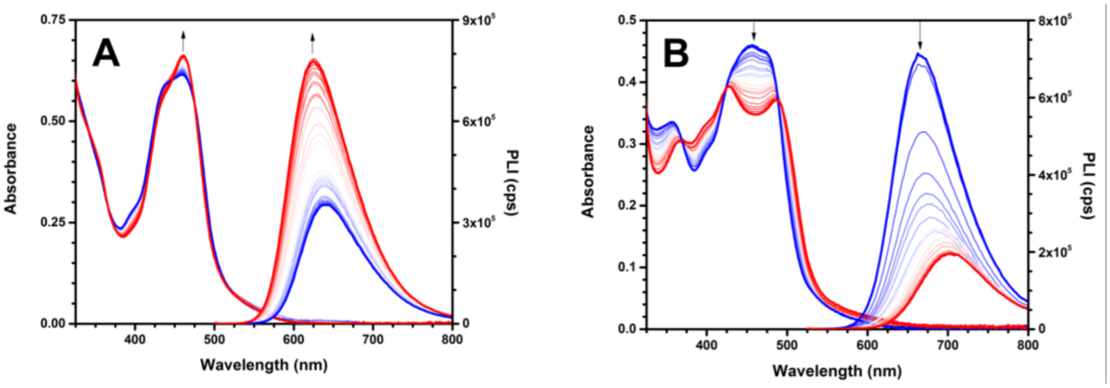

Figure 5.3. UV-visible absorption and photoluminescence spectra of [Ru^{II}(btfmb)$_2$(dcb)], A, and [Ru^{II}(dtb)$_2$(dcb)], B, in aqueous solution titrated from the deprotonated carboxylate, -COO$^-$ (blue), to the carboxylic acid, -COOH (red), forms of the compounds. Arrows indicate direction of intensity changes with decreasing pH.

Excitation into the MLCT absorption band resulted in room temperature photoluminescence (PL) for both the btfmb and dtb compounds. Under basic conditions, $[\mathrm{Ru^{II}(btfmb)_2(dcb^{2-})}]^{0*}$, exhibited a photoluminescence band at 640 nm which blue-shifted to 625 nm in acidic solution; an energy increase of approximately 380 $\mathrm{cm^{-1}}$. Photoluminescence from $[\mathrm{Ru^{II}(dtb)_2(dcb^{2-})}]^{0*}$ dissolved in basic aqueous solution maximized at 665 nm and red-shifted to 700 nm under acidic conditions; an approximately 750 $\mathrm{cm^{-1}}$ shift in energy, shown in Figure 5.3. Photoluminescence quantum yields ranging from 0.003 to 0.033 were quantified by the optically dilute method using $\mathrm{[Ru(bpy)_3]Cl_2}$ in water as a reference and are collected in Table 5.1 along with other photophysical parameters.[28] Pulsed light excitation of the compounds in aqueous solutions yielded MLCT excited states that decayed to the ground state by a first-order kinetic model. The MLCT excited state lifetimes ranged from τ = 140 to 690 ns for deaerated solutions of the $[\mathrm{Ru^{II}(btfmb)_2(dcb)}]$ and $[\mathrm{Ru^{II}(dtb)_2(dcb)}]$ compounds. Knowledge of the photoluminescence quantum yields, Φ_{PL}, and excited state lifetimes allowed for calculation of the radiative, k_r, and non-radiative, k_{nr}, decay rate constants using Equations (5.2) and (5.3), respectively.

$$k_r = \frac{\Phi_{PL}}{\tau} \tag{5.2}$$

$$k_{nr} = \frac{1}{\tau} - k_r \tag{5.3}$$

The PL quantum yields and natural logarithm of the non-radiative decay rates for the compounds were plotted versus their photoluminescence maxima and found to obey a linear trend, shown in Figure 5.4. The ground-state pK_a's of $[\mathrm{Ru^{II}(btfmb)_2(dcbH_2)}]^{2+}$ and $[\mathrm{Ru^{II}(dtb)_2(dcbH_2)}]^{2+}$ were determined by monitoring the relative absorption intensity change at 460 or 455 nm, respectively, as a function of pH. The absorbance intensity for both compounds was pH independent above pH 5 and below pH 2. The normalized absorption data for both compounds fit well to a single sigmoidal model which exhibited an inflection point, pH$_\mathrm{i}$, at pH 2.9, as indicated in Figure 5.5. Thus, the ground state pK_a values for $[\mathrm{Ru^{II}(btfmb)_2(dcbH_2)}]^{2+}$ and $[\mathrm{Ru^{II}(dtb)_2(dcbH_2)}]^{2+}$ are both equal to 2.9.

The excited state p$K_a{}^*$'s for luminescent compounds can be determined using several methods. The Förster method uses a thermodynamic cycle to calculate p$K_a{}^*$:

$$\mathrm{p}K_a{}^* = \mathrm{p}K_a + \left(\frac{2.303R}{T}\right)(\upsilon_B - \upsilon_{HB}) \tag{5.4}$$

where R is the gas constant, T is temperature, and v is the absorbance or photoluminescence maximum in wavenumbers (cm^{-1}) for the deprotonated (v_B) and protonated (v_{HB}) forms. Using the Förster method, excited state p$K_a{}^*$'s were estimated directly from ground-state absorption data and yields p$K_a{}^*$ = 3.1 and 5.4 for $[\mathrm{Ru^{II}(btfmb)_2(dcbH_2)}]^{2+*}$ and $[\mathrm{Ru^{II}(dtb)_2(dcbH_2)}]^{2+*}$, respectively. Use of the photoluminescence maxima results in p$K_a{}^*$'s of 4.4 and 2.1 for the btfmb and dtb compounds, respectively. Alternatively, if both the protonated and deprotonated forms of a compound are luminescent, Equation (5.5) can be used to determine p$K_a{}^*$ values using a kinetic analysis based on Figure 5.1:

Table 5.1. Photophysical parameters of $[Ru^{II}(btfmb)_2(dcbH_2)]^{2+}$ and $[Ru^{II}(dtb)_2(dcbH_2)]^{2+}$ in aqueous solution.

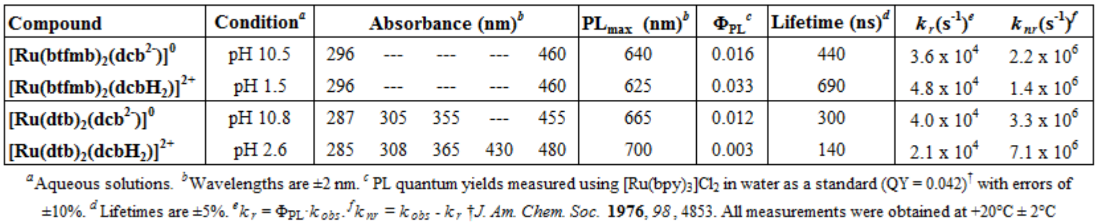

Compound	**Condition**[a]	**Absorbance (nm)**[b]					**PL_{max} (nm)**[b]	**Φ_{PL}**[c]	**Lifetime (ns)**[d]	**k_r(s^{-1})**[e]	**k_{nr}(s^{-1})**[f]
$[Ru(btfmb)_2(dcb^{2-})]^0$	pH 10.5	296	---	---	---	460	640	0.016	440	3.6×10^4	2.2×10^6
$[Ru(btfmb)_2(dcbH_2)]^{2+}$	pH 1.5	296	---	---	---	460	625	0.033	690	4.8×10^4	1.4×10^6
$[Ru(dtb)_2(dcb^{2-})]^0$	pH 10.8	287	305	355	---	455	665	0.012	300	4.0×10^4	3.3×10^6
$[Ru(dtb)_2(dcbH_2)]^{2+}$	pH 2.6	285	308	365	430	480	700	0.003	140	2.1×10^4	7.1×10^6

[a] Aqueous solutions. [b] Wavelengths are ±2 nm. [c] PL quantum yields measured using $[Ru(bpy)_3]Cl_2$ in water as a standard (QY = 0.042)† with errors of ±10%. [d] Lifetimes are ±5%. [e] $k_r = \Phi_{PL} \cdot k_{obs}$. [f] $k_{nr} = k_{obs} - k_r$ †*J. Am. Chem. Soc.* **1976**, *98*, 4853. All measurements were obtained at +20°C ± 2°C

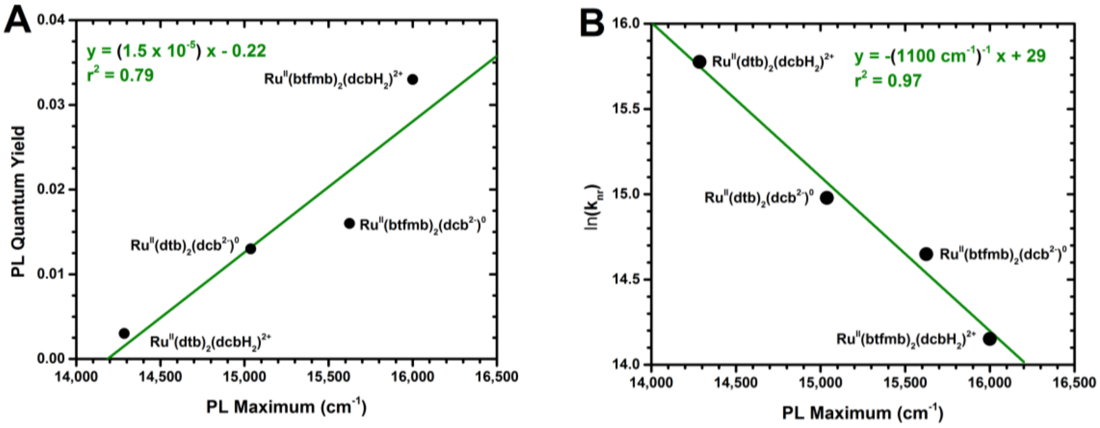

Figure 5.4. Photoluminescence (PL) quantum yields, A, and the natural logarithm of the non-radiative decay rate (k_{nr}), B, vs. PL maxima for the compounds in aqueous solutions. Linear best fits to the data are shown as green lines.

$$\mathrm{p}K_a{}^* = \mathrm{pH}_i{}^* + \log\left(\frac{\tau_{HB}}{\tau_B}\right) \tag{5.5}$$

that requires the photoluminescence lifetimes of the protonated (τ_{HB}) and deprotonated forms (τ_{B}). The photoluminescence titration curve inflection points, $\mathrm{pH_i}^*$, for $[\mathrm{Ru^{II}(btfmb)_2(dcbH_2)}]^{2+*}$ and $[\mathrm{Ru^{II}(dtb)_2(dcbH_2)}]^{2+*}$ were determined to be 1.8 and 4.1, respectively, from the data shown in Figure 5.5. Use of the kinetic analysis method yielded $pK_a{}^*$'s of 2.0 and 3.8 for $[\mathrm{Ru^{II}(btfmb)_2(dcbH_2)}]^{2+*}$ and $[\mathrm{Ru^{II}(dtb)_2(dcbH_2)}]^{2+*}$, respectively. The variation in the estimated $\mathrm{p}K_a{}^*$ values determined using the different methods will be examined in the Discussion section.

Transient absorption spectra of $[\mathrm{Ru^{II}(btfmb)_2(dcbH_2)}]^{2+*}$ and $[\mathrm{Ru^{II}(dtb)_2(dcbH_2)}]^{2+*}$ were obtained under both basic and acidic conditions in aqueous solutions using pulsed 532 nm laser excitation. The difference spectra shown in Figure 5.6 were normalized for comparative purposes to the transient absorption features observed below 400 nm, which were attributed to ligand-centered $\pi^* - \pi^*$ transitions. Both the fully protonated and deprotonated forms of $[\mathrm{Ru^{II}(btfmb)_2(dcbH_2)}]^{2+*}$ exhibited sharp transient absorption features that maximized at 370 nm and transient bleach features at 460 nm associated with depletion of $[\mathrm{Ru^{II}(btfmb)_2(dcbH_2)}]^{2+}$. In contrast to the btfmb compound, the transient absorption feature for the fully deprotonated $[\mathrm{Ru^{II}(dtb)_2(dcb^{2-})}]^{0*}$ blue-shifted from 380 nm to 350 nm upon protonation to $[\mathrm{Ru^{II}(dtb)_2(dcbH_2)}]^{2+*}$. The transient bleach minimum was 450 nm for both forms of $[\mathrm{Ru^{II}(dtb)_2(dcbH_2)}]^{2+*}$, although the bleach was broader for the protonated form compared to the deprotonated form, consistent with the ground state absorption spectra. Transient photoluminescence spectral features, not shown, were in good agreement with the steady-state photoluminescence spectra shown in Figure 5.3.

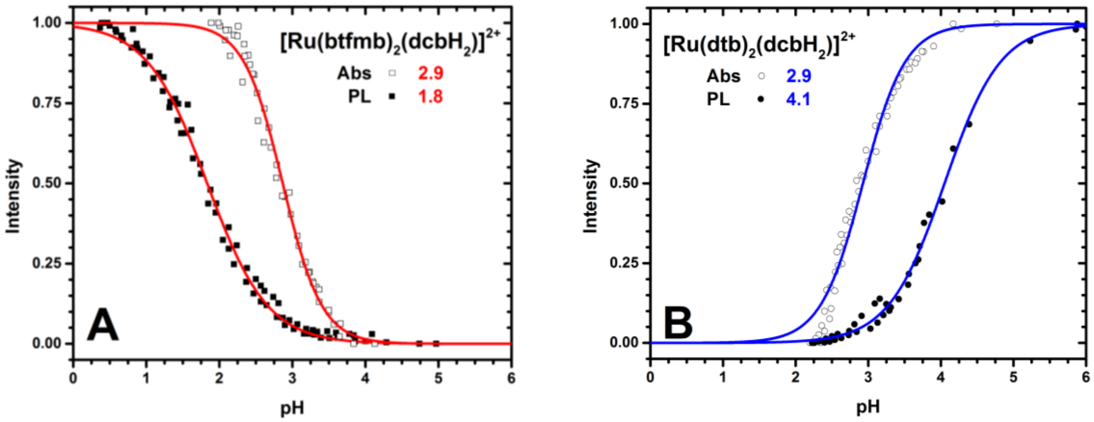

Figure 5.5. Spectrophotometric titration curves of $[Ru^{II}(btfmb)_2(dcbH_2)]^{2+}$ (squares) and $[Ru^{II}(dtb)_2(dcbH_2)]^{2+}$ (circles) showing the relative absorbance (open symbols) and photoluminescence (closed symbols) intensity changes as a function of pH. Overlaid on the data are sigmoidal fits (solid blue and red lines) with inflection points noted in the figure legend.

Table 5.2. Ground- and excited state pK_a values determined using methods described in the text.

Compound	**pK_a**	**$\nu_{B, abs}$ (cm^{-1})**	**$\nu_{HB, abs}$ (cm^{-1})**	**pK_a* (Forster, abs)**	**$\nu_{B, PL}$ (cm^{-1})**	**$\nu_{HB, PL}$ (cm^{-1})**	**pK_a* (Forster, PL)**	**pK_a* (Lifetime)**
$[Ru^{II}(btfmb)_2(dcbH_2)]^{2+}$	2.9	21,800	21,700	3.1	15,600	16,000	2.1	2.0
$[Ru^{II}(dtb)_2(dcbH_2)]^{2+}$	2.9	22,000	20,800	5.4	15,000	14,300	4.4	3.8

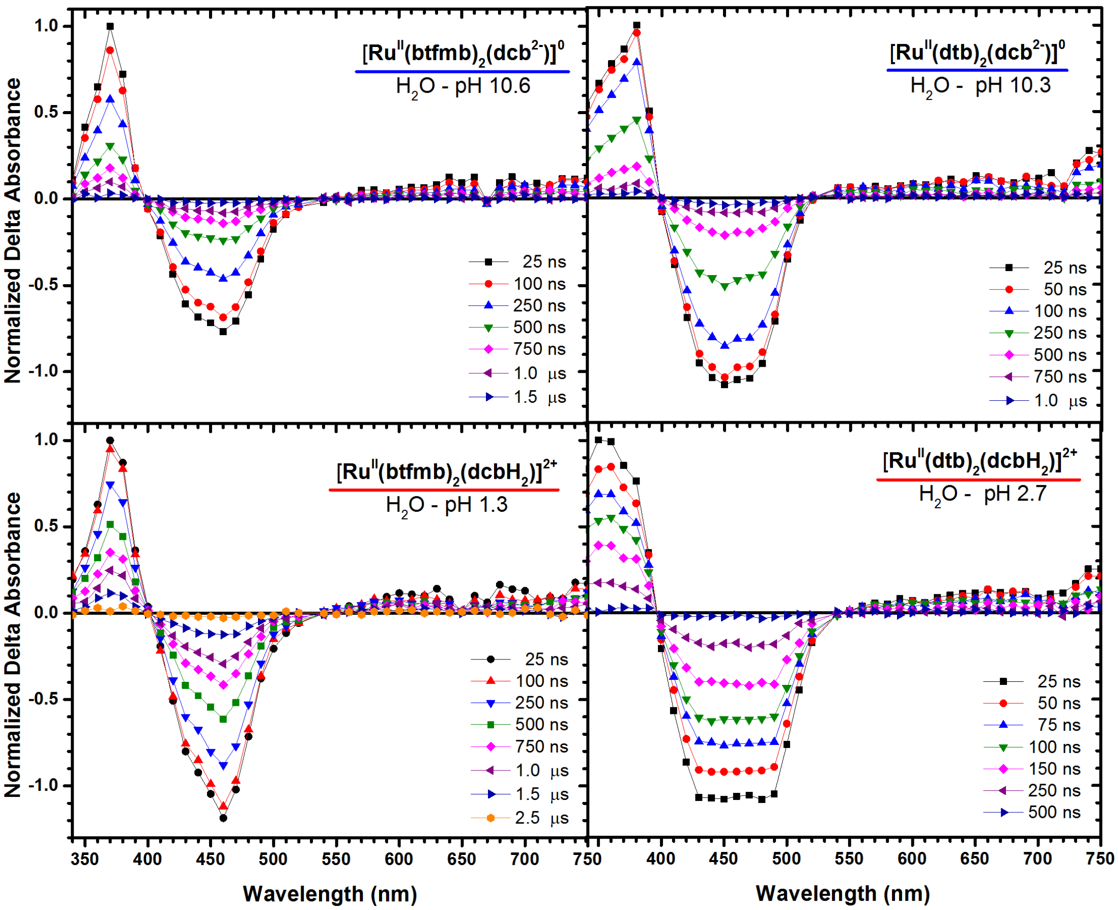

Figure 5.6. Transient absorption spectra [Ru^{II}(btfmb)$_2$(dcbH$_2$)]$^{2+}$ (left) and [Ru^{II}(dtb)$_2$(dcbH$_2$)]$^{2+}$ (right) in basic (top) and acidic (bottom) aqueous conditions.

Clean isosbestic points were observed for the full spectra around 400 and 530 nm for all compounds studied. The transient absorption and photoluminescence spectra were normalizable with respect to time at the pH's indicated in Figure 5.6, behavior consistent with generation of a single excited state that relaxed back to the initial ground state. The first-order excited state relaxation kinetics were observation wavelength independent and in excellent agreement with the excited state lifetimes determined from the time-resolved photoluminescence data.

Difference curves that highlight the pH range where excited state acid-base chemistry differs from that of the ground state, Figure 5.7, were generated by subtracting the sigmoidal fit of the spectrophotometric absorption data from that of the photoluminescence data fit, Figure 5.5. The maximum of the curve indicates the pH where the largest magnitude of protonation change will occur between the ground and excited state for each compound. Transient photoluminescence spectra of $[Ru^{II}(btfmb)_2(dcbH_2)]^{2+*}$ and $[Ru^{II}(dtb)_2(dcbH_2)]^{2+*}$ were measured at pH's close to the pH of predicted maximum protonation state change. Normalized photoluminescence spectra of the fully protonated and deprotonated forms of both the btfmb and dtb compounds are shown 25 ns after pulsed laser excitation, Figure 5.8. The normalized photoluminescence spectra of $[Ru^{II}(btfmb)_2(dcbH_2)]^{2+*}$ in pH 2.3 water showed minimal change over all time delays which was in stark contrast to $[Ru^{II}(dtb)_2(dcbH_2)]^{2+*}$ in pH 3.5 water which exhibited significant red-shifts of the spectra with increasing time delay, Figure 5.8.

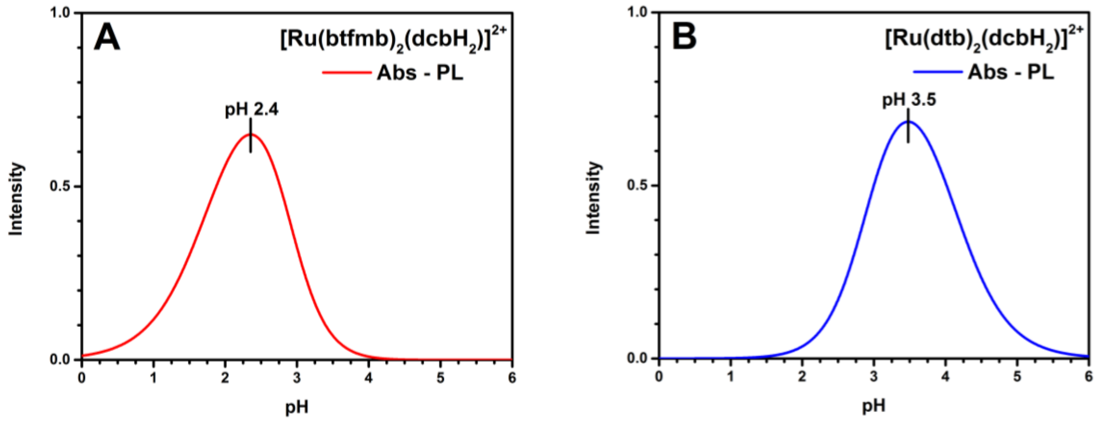

Figure 5.7. Difference curves between the sigmoidal fits to the spectrophotometric absorption (Abs) and photoluminescence (PL) titration data given in Figure 5.5 for [Ru^{II}(btfmb)$_2$(dcbH$_2$)]$^{2+}$, A, and [Ru^{II}(dtb)$_2$(dcbH$_2$)]$^{2+}$, B. The maximum intensity of the curves indicate the pH where the maximum protonation state changes will occur between the ground and excited states of the compounds.

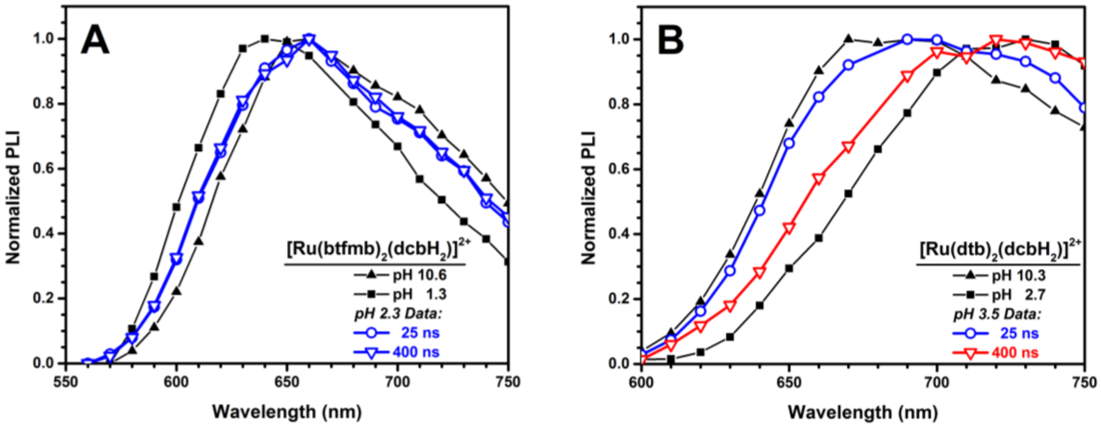

Figure 5.8. Transient photoluminescence spectra obtained in aqueous solutions of [Ru^{II}(btfmb)$_2$(dcbH$_2$)]$^{2+}$, A, and [Ru^{II}(dtb)$_2$(dcbH$_2$)]$^{2+}$, B. Spectra of the fully deprotonated or protonated forms obtained 25 ns after laser excitation are given for reference under basic (black, up triangles) or acidic (black, squares) conditions. Photoluminescence spectra obtained near the pH of maximum excited state protonation state changes are indicated by the colored lines obtained 25 ns (open circles) or 400 ns (open down triangles) after pulsed light excitation for [Ru^{II}(btfmb)$_2$(dcbH$_2$)]$^{2+}$ and [Ru^{II}(dtb)$_2$(dcbH$_2$)]$^{2+}$ at pH 2.3 or 3.5, respectively.

5.4 Discussion

The photophysical characteristics of two ruthenium compounds containing carboxylic acid derivatized bipyridine ligands with different ancillary ligands were quantified. Special attention was paid to the acid-base chemistry of the ground and excited states of the compounds. The compounds $[Ru^{II}(btfmb)_2(dcbH_2)]^{2+}$ and $[Ru^{II}(dtb)_2(dcbH_2)]^{2+}$ exhibited room temperature photoluminescence from excitation into MLCT absorption bands in the visible region. The photoluminescence titration data of $[Ru^{II}(btfmb)_2(dcbH_2)]^{2+}$ presents the first instance of a ruthenium compound with carboxylic acid functionality that exhibits a hypsochromic (blue) shift with decreasing pH. The observed linear correlation between the photoluminescence quantum yields and the natural logarithm of the non-radiative decay rate as a function of the photoluminescence maximum, in wavenumbers, indicates that the compounds studied in this chapter follow the Jortner energy gap law.[30-31] The slope of $-(1{,}100\ \mathrm{cm}^{-1})^{-1}$ for the non-radiative decay rate versus photoluminescence maximum is identical to values previously reported for a series of ruthenium and osmium polypyridyl compounds.[32-33]

Only single inflection points were observed in the spectrophotometric titration curves of both compounds (either absorbance or photoluminescence) were observed when two were expected. We suspect that the two pK_a values are so close that they could not be experimentally resolved as such behavior has been reported for many other ruthenium polypyridyl compounds containing carboxylic acid groups.[1,12-13,17] This suggests that the pK_a values reported for the ground and excited states represent an average of the two true values. However, it cannot be ruled out that the inflection point is only reporting on the first protonation step and that a second protonation step is spectroscopically silent over the pH range monitored.

The excited state acid-base behavior of these compounds can be exploited for use as pH probes in aqueous solution. Using a wavelength-ratiometric analysis of the peak photoluminescence maximum between the two protonation states, one can generate the ratiometric pH curves shown in Figure 5.9.[3,34] Use of these compounds as pH probes would allow for pH determination over a dynamic range of 3 pH units between pH 0.5 to 3.5 using the btfmb compound or between pH 2.0 to 5.0 using the dtb compound.

The ground state pK_a values for the btfmb and dtb compounds were measured using spectrophotometric titrations which yielded pK_a = 2.9 for both compounds. These pK_a's are consistent with previous reports which range from pK_a = 2.2 – 4.4 for related ruthenium compounds containing carboxylic acid derivatized bipyridines.[12-13,17]

The excited state pK_a^* values were determined using several methods established in the literature. The simplest, so-called Förster method only requires knowledge of the absorbance maximum for the deprotonated and protonated forms of a compound along with the ground-state pK_a, Equation (5.4). This method is commonly used for organic compounds which emit from singlet excited states or for compounds that are non-luminescent. For comparison to other literature data of ruthenium compounds, pK_a* values were determined using this method and reported in Table 5.2. However, this method is technically inappropriate for ruthenium(II) polypyridyl compounds due to the formally triplet character of the lowest – lying MLCT excited state.

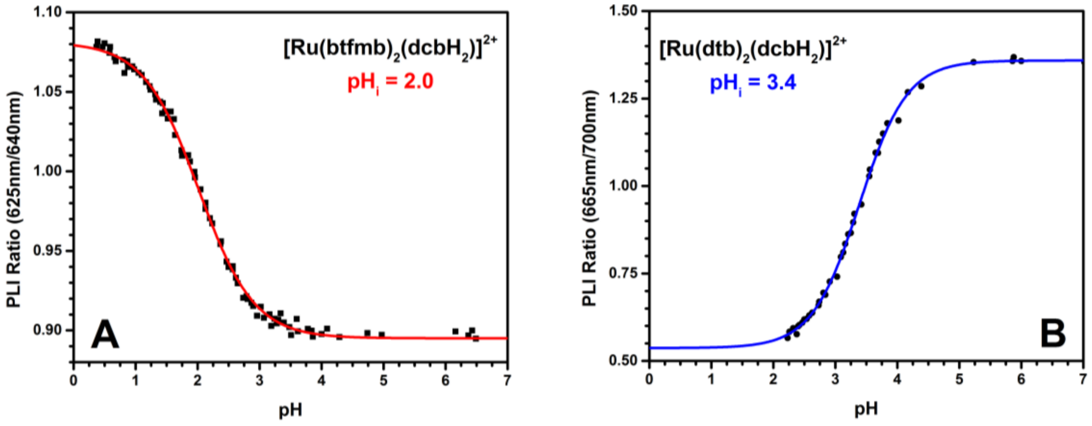

Figure 5.9. Wavelength-ratiometric curves as a function of pH for $[Ru^{II}(btfmb)_2(dcbH_2)]^{2+}$, A, and $[Ru^{II}(dtb)_2(dcbH_2)]^{2+}$, B, determined from their photoluminescence spectra.

Therefore, more accurate values can be obtained using the photoluminescence maxima and Equation (5.4), as they more adequately estimate $E_{0\text{-}0}$, which results in pK_a*'s of 4.4 and 2.1 for the btfmb and dtb compounds, respectively. The most robust method, Equation (5.5), makes use of a kinetic cycle based on the square scheme in Figure 5.1 and the excited state lifetimes for both protonation states of the compounds. Evaluation using the kinetic analysis results in pK_a*'s of 3.8 and 2.0 for $[Ru^{II}(btfmb)_2(dcbH_2)]^{2+*}$ and $[Ru^{II}(dtb)_2(dcbH_2)]^{2+*}$, respectively, which are in reasonable agreement with the values obtained from the Förster analysis using photoluminescence maxima. It is interesting to note that calculated pK_a* values occur at pH's similar to the inflection points of the wavelength ratiometric curves.

The pK_a*'s indicate a reversal in excited state acid base behavior between the two compounds based on ancillary ligand modification from electron-withdrawing trifluoromethyl groups to slightly electron-donating *tert*-butyl groups as the protonatable dcb ligand remains constant. This means that $[Ru^{II}(dtb)_2(dcbH_2)]^{2+*}$ is a stronger base, $\Delta pK_a = +0.9$, in the excited state that the ground state. This behavior has been reported for similar ruthenium polypyridyl compounds and was attributed to increased electron density at the carboxylate due to electron localization on the carboxylic acid derivatized ligand in the excited state. In stark contrast, $[Ru^{II}(btfmb)_2(dcbH_2)]^{2+*}$ is a stronger acid, $\Delta pK_a = -0.9$, in the excited state that the ground state. Behavior likely attributed to excited state electron localization on the btfmb ligand which renders the protonatable dcb ligand electron deficient as a result of back-donation to the formally Ru(III) metal center. This is the first report of a ruthenium compound containing a carboxylic acid group that exhibits stronger acidity in the excited state. All other carboxylic acid based compounds exhibit increased basicity in the excited state akin to that seen for $[\mathrm{Ru^{II}(dtb)_2(dcbH_2)}]^{2+*}$. While photoacidic ruthenium compounds have been reported, they generally contain pendant amines or hydroxyl groups which can undergo drastic resonance restructuring in the excited state.

Evidence for the difference in electron localization can be seen in the transient absorption spectra, Figure 5.6. In the case of the dtb compound, the fully protonated form, $[\mathrm{Ru^{II}(dtb)_2(dcbH_2)}]^{2+*}$, exhibits a ligand-centered transient absorption feature at 350 nm. This electronic transition shifts to lower energy, 380 nm, for the fully deprotonated form, $[\mathrm{Ru^{II}(dtb)_2(dcb^{2-})}]^{0*}$. This observation is fully consistent with the absorption feature being attributed to excited state electron localization on the dcb ligand with the electronic transition being affected by the protonation state of the ligand. In contrast, the fact that the transient absorption feature for both $[\mathrm{Ru^{II}(btfmb)_2(dcbH_2)}]^{2+*}$ and $[\mathrm{Ru^{II}(btfmb)_2(dcb^{2-})}]^{0*}$ maximizes at 370 nm is consistent with the idea that the electron localizes on the btfmb ligand which is not associated with acid-base chemistry. The transient features between 400 and 530 nm for the compounds studied can be accounted for purely by the bleach of the ground state absorption spectra.

In order to determine the pH range where excited state acid-base chemistry would occur, difference curves were generated by subtracting the sigmoidal fit to the spectrophotometric photoluminescence titration curve from that of the absorption curve for both compounds, Figure 5.6. The maximum of each curve indicated the pH where the largest protonation change should occur between the ground and excited states. For example, the $[\mathrm{Ru^{II}(btfmb)_2(dcbH_2)}]^{2+}$ form predominates in the ground state at pH 2.4, 85%, but after excitation to the MLCT state the compound loses two protons generating the $[\mathrm{Ru^{II}(btfmb)_2(dcb^{2-})}]^{0*}$ form, which constitutes 80% of the sample. Conversely, at pH

3.5 for the dtb compound, the ground state is comprised predominantly of the $[Ru^{II}(dtb)_2(dcb^{2-})]^{0*}$ form, 88%, which protonates in the excited state forming $[Ru^{II}(dtb)_2(dcbH_2)]^{2+}$, 80% of the sample.

Transient photoluminescence spectra were obtained at pH's near the values predicted for maximum change, Figure 5.8. Spectral modeling of the experimental spectra using reference spectra obtained of the fully protonated and deprotonated forms allowed for the fractional composition of the different protonation states to be determined as a function of time, Figure 5.10. For the btfmb compound in pH 2.3 water, the photoluminescence spectra most resembled the fully deprotonated $[Ru^{II}(btfmb)_2(dcb^{2-})]^{0*}$ state immediately after pulsed laser excitation of $[Ru^{II}(btfmb)_2(dcbH_2)]^{2+}$, which was consistent with increased acidity in the excited state. The ratio of the two forms remained relatively constant, 4:1 (dcb^{2-} : $dcbH_2$), over the duration of the experiment. The data could be fit to single exponential kinetics with a time constant of 10 ns. The dtb compound in pH 3.5 water exhibited drastic time-dependent changes in the fractional composition of the excited states. Following pulsed laser excitation, the initial $[Ru^{II}(btfmb)_2(dcb^{2-})]^0$ could be seen cleanly converting into the $[Ru^{II}(dtb)_2(dcbH_2)]^{2+}$ form with single exponential kinetics indicating a protonation rate of 2×10^7 s^{-1}. After 200 ns, the fractional composition reached a ratio of 1:9 (dcb^{2-} : $dcbH_2$), and remained constant for the rest of the experiment. This data represents the first transient observation of a ruthenium polypyridyl compound converting from one protonation state to another in the excited state.

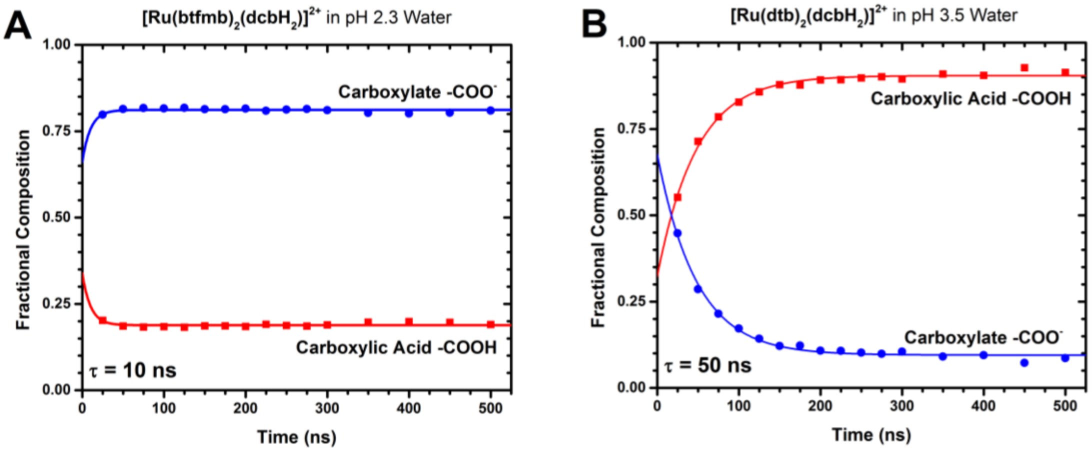

Figure 5.10. Fractional composition of the fully protonated (red) and deprotonated (blue) forms of $[Ru^{II}(btfmb)_2(dcbH_2)]^{2+}$, A, and $[Ru^{II}(dtb)_2(dcbH_2)]^{2+}$, B, in pH 2.3 or 3.5 water, respectively, as a function of time after pulsed 532 nm laser excitation.

5.5 Conclusions

The photophysical acid-base properties of two ruthenium polypyridyl compounds containing carboxylic acid derivatized bipyridine ligands are reported. The ground-state pK_a's for the compound were found to be identical, pK_a = 2.9, and consistent with related compounds. The photoluminescence properties and excited state pK_a's were found to be drastically influenced by the nature of the ancillary ligand not associated with the acid-base chemistry. The $[Ru^{II}(dtb)_2(dcbH_2)]^{2+}$ compound containing slightly electron-donating dtb ligands was characterized by enhanced basicity in the excited state with pK_a* = 3.8. Conversely, the compound with electron-withdrawing btfmb ligands, $[Ru^{II}(btfmb)_2(dcbH_2)]^{2+}$, exhibited increased acidity in the excited state with pK_a* = 2.0 and is the first instance of a carboxylic acid-based ruthenium photoacid. Due to the pH-dependent photoluminescence maxima for the fully deprotonated or protonated states, the two compounds studied could be used as wavelength ratiometric pH probes for pH determination from pH 0.5 to 5.0. Furthermore, the transient photoluminescence data presented in this chapter provide the first clear observation of a ruthenium polypyridyl compound converting from one protonation form, $[Ru^{II}(dtb)_2(dcb^{2-})]^{0*}$, to another, $[Ru^{II}(dtb)_2(dcbH_2)]^{2+*}$, in the excited state.

5.6 References

(1) Vos, J. G. *Polyhedron* **1992,** *11*, 2285-2299.

(2) Hicks, C.; Ye, G.; Levi, C.; Gonzales, M.; Rutenburg, I.; Fan, J.; Helmy, R.; Kassis, A.; Gafney, H. D. *Coord. Chem. Rev.* **2001,** *211*, 207-222.

(3) Murtaza, Z.; Chang, Q.; Rao, G.; Lin, H.; Lakowicz, J. R. *Anal. Biochem.* **1997,** *247*, 216-222.

(4) Laws, W. R.; Posner, G. H.; Brand, L. *Arch. Biochem. Biophys.* **1979,** *193*, 88-100.

(5) Bowie, L. J.; Irwin, R.; Loken, M.; DeLuca, M.; Brand, L. *Biochemistry* **1973,** *12*, 1852-1857.

(6) Loken, M. R.; Hayes, J. W.; Gohlke, J. R.; Brand, L. *Biochemistry* **1972,** *11*, 4779-4786.

(7) Greiner, G.; Maier, I. *J. Chem. Soc., Perkin Trans. 2* **2002**, 1005-1011.

(8) Ireland, J. F.; Wyatt, P. A. H., Acid-Base Properties of Electronically Excited States of Organic Molecules. In *Adv. Phys. Org. Chem.*, Gold, V., Ed. Academic Press: 1976; Vol. Volume 12, pp 131-221.

(9) Whitaker, J. E.; Haugland, R. P.; Prendergast, F. G. *Anal. Biochem.* **1991,** *194*, 330-344.

(10) Huynh, M. H. V.; Meyer, T. J. *Chem. Rev.* **2007,** *107*, 5004-5064.

(11) Wenger, O. S. *Acc. Chem. Res.* **2013,** *46*, 1517-1526.

(12) Giordano, P. J.; Bock, C. R.; Wrighton, M. S.; Interrante, L. V.; Williams, R. F. X. *J. Am. Chem. Soc.* **1977,** *99*, 3187-3189.

(13) Xie, P.-H.; Hou, Y.-J.; Zhang, B.-W.; Cao, Y.; Wu, F.; Tian, W.-J.; Shen, J.-C. *Dalton Trans.* **1999**, 4217-4221.

(14) Nazeeruddin, M. K.; Kalyanasundaram, K. *Inorg. Chem.* **1989,** *28*, 4251-4259.

(15) Lay, P. A.; Sasse, W. H. F. *Inorg. Chem.* **1984,** *23*, 4123-4125.

(16) Shimidzu, T.; Iyoda, T.; Izaki, K. *J. Phys. Chem.* **1985,** *89*, 642-645.

(17) Higgins, B.; DeGraff, B. A.; Demas, J. N. *Inorg. Chem.* **2005,** *44*, 6662-6669.

(18) Dixon, E. N.; Snow, M. Z.; Bon, J. L.; Whitehurst, A. M.; DeGraff, B. A.; Trindle, C.; Demas, J. N. *Inorg. Chem.* **2012,** *51*, 3355-3365.

(19) M. W. Cargill Thompson, A.; C. C. Smailes, M.; C. Jeffery, J.; D. Ward, M. *Dalton Trans.* **1997**, 737-744.

(20) Kirsch-De Mesmaeker, A.; Jacquet, L.; Nasielski, J. *Inorg. Chem.* **1988,** *27*, 4451-4458.

(21) Giordano, P. J.; Bock, C. R.; Wrighton, M. S. *J. Am. Chem. Soc.* **1978,** *100*, 6960-6965.

(22) Peterson, S. H.; Demas, J. N. *J. Am. Chem. Soc.* **1979,** *101*, 6571-6577.

(23) Furue, M.; Maruyama, K.; Oguni, T.; Naiki, M.; Kamachi, M. *Inorg. Chem.* **1992,** *31*, 3792-3795.

(24) Benson, E. E.; Grice, K. A.; Smieja, J. M.; Kubiak, C. P. *Polyhedron* **2013,** *58*, 229-234.

(25) Ardo, S.; Sun, Y.; Staniszewski, A.; Castellano, F. N.; Meyer, G. J. *J. Am. Chem. Soc.* **2010,** *132*, 6696-6709.

(26) Oki, A. R.; Morgan, R. J. *Synth. Commun.* **1995,** *25*, 4093-4097.

(27) Yu, Z.; Najafabadi, H. M.; Xu, Y.; Nonomura, K.; Sun, L.; Kloo, L. *Dalton Trans.* **2011,** *40*, 8361-8366.

(28) Van Houten, J.; Watts, R. J. *J. Am. Chem. Soc.* **1976,** *98*, 4853-4858.

(29) Argazzi, R.; Bignozzi, C. A.; Heimer, T. A.; Castellano, F. N.; Meyer, G. J. *Inorg. Chem.* **1994,** *33*, 5741-5749.

(30) Englman, R.; Jortner, J. *Mol. Phys.* **1970,** *18*, 145-164.

(31) Freed, K. F.; Jortner, J. *J. Chem. Phys.* **1970,** *52*, 6272-6291.

(32) Caspar, J. V.; Meyer, T. J. *J. Am. Chem. Soc.* **1983,** *105*, 5583-5590.

(33) Kober, E. M.; Caspar, J. V.; Lumpkin, R. S.; Meyer, T. J. *J. Phys. Chem.* **1986,** *90*, 3722-3734.

(34) Tormo, L.; Bustamante, N.; Colmenarejo, G.; Orellana, G. *Anal. Chem.* **2010,** *82*, 5195-5204.

Curriculum Vitae

Ryan M. O'Donnell

Born on January 19th, 1988 in Dayton, Ohio

EDUCATION

Johns Hopkins University – Baltimore, Maryland

Doctor of Philosophy in Chemistry obtained in November of 2014 (GPA of 3.75/4.00)
Master of Arts in Chemistry obtained in April of 2012

- 2012 National Science Foundation Graduate Research Opportunities Worldwide (NSF GROW) funding recipient. Traveled to Uppsala University (Uppsala, Sweden) to collaborate with Anders Hagfeldt and Gerrit Boschloo on electroabsorption spectroscopy experiments.
- 2011 National Science Foundation Graduate Research Fellow (NSF GRFP)

Ohio University – Athens, Ohio

Bachelor of Science in Chemistry completed in June of 2010 (GPA of 3.66/4.00)
Honors Tutorial College Chemistry Student
Mathematics Minor

- 2009 Jeanette G. Grasselli Brown Undergraduate Research Award
- 2008 Goldwater Scholar
- 2008 Department of Homeland Security Scholar
- 2009 & 2007 Recipient of Jesse Day Undergraduate Award

RESEARCH EXPERIENCE

Ph.D. Candidate and Graduate Research Assistant for Professor Gerald J. Meyer

September 2010 – November 2014

Projects: 1) Excited state relaxation pathways of ruthenium polypyridyl compounds relevant to dye-sensitized solar cells. 2) Electric fields and cation dependent charge screening in dye-sensitized titanium dioxide thin films. 3) Development of a ruthenium compound exhibiting increased acidity in the excited state.

Working knowledge of ultraviolet-visible light spectroscopy (UV-Vis), transient absorption spectroscopy, electrochemistry, spectroelectrochemistry, steady-state and time-resolved photoluminescence spectroscopy, cryostat equipment, inorganic synthesis, metal oxide thin films.

Software: Origin, LabView, ChemDraw, Microsoft Office, Mathematica, EndNote, Mercury, Gaussian

Undergraduate Research Assistant for Professor Jeffery J. Rack

June 2008 – July 2010

Project: Development of a photoactive electrode through incorporation of simultaneously photochromic/electrochromic complexes.

Working knowledge of electrochemistry, ultraviolet-visible light spectroscopy (UV-Vis), nuclear magnetic resonance spectroscopy (^{1}H-, ^{13}C-NMR, COSY), infrared spectroscopy, linkage isomerism, electrochemical methods, and general inorganic chemistry laboratory techniques.

Summer Internship at Lawrence Livermore National Laboratory (Mentor: **Dr. Nerine J. Cherepy)**
June 2009 – August 2009
Project: Detection of nitroaromatic explosives *via* Meisenheimer complexation.
Worked with UV-Vis spectroscopy, solution-based Meisenheimer chemistry, synthesized epoxy-amine polymers, and researched fluorescence quenching materials.

Undergraduate Research Assistant for Professor Peter de B. Harrington
April 2007 – June 2008
Projects: Detection of cocktail explosives and detection of illicit drugs in adulterated urine samples via ion mobility spectrometry.
Working knowledge of ion mobility spectrometry, gas chromatography-mass spectrometry, MATLAB software, solid phase extraction, and general analytical chemistry laboratory procedures.

PUBLICATIONS

6) Sampaio, R.N.; O'Donnell, R.M.; Meyer, G.J. Electric Field Control of $TiO_2(e^-) + I_3^- \rightarrow$ Charge Recombination Relevant to Dye Sensitized Solar Cells. *J. Phys. Chem. Lett.*, **2014**, *5*, 3265. (DOI: 10.1021/jz5016444)

5) O'Donnell, R.M.; Sampaio, R.N.; Barr, T.J.; Meyer, G.J. Electric Fields and Charge Screening in Dye Sensitized Mesoporous Nanocrystalline TiO_2 Thin Films. *Journal of Physical Chemistry C*, **2014**, *118*, 16976. (DOI: 10.1021/jp500493t)

4) O'Donnell, R.M.; Ardo, S.; Meyer, G.J. Charge-Screening Kinetics at Sensitized TiO_2 Interfaces. *Journal of Physical Chemistry Letters*, **2013**, *4*, 2817-2821. (DOI: 10.1021/jz4014689)

3) O'Donnell, R.M.; Johansson, P.J.; Abrahamsson, M.; Meyer, G.J. Excited-State Relaxation of Ruthenium Polypyridyl Compounds Relevant to Dye-Sensitized Solar Cells. *Inorganic Chemistry*, **2013**, *52*, 6839-6848. (DOI: 10.1021/ic302339a)

2) Lu, Y.; O'Donnell, R.M.; Harrington, P.B. Detection of Cocaine and its Metabolites in Urine Using Solid Phase Extraction – Ion Mobility Spectrometry with Alternating Least Squares. *Forensic Science International*. **2009**, *189*, 54-59. (DOI:10.1016/j.forsciint.2009.04.007)

1) O'Donnell, R.M.; Sun, X.; Harrington, P.B. Pharmaceutical Applications of Ion Mobility Spectrometry. *Trends in Analytical Chemistry.* **2008**, *27*, 44-53. (DOI:10.1016/j.trac.2007.10.014)

PRESENTATIONS (10: 5 Oral, 5 Poster)

Cation Dependent Charge-Screening Kinetics at Sensitized TiO_2 Interfaces. Ryan M. O'Donnell, Renato N. Sampaio, Timothy J. Barr, & Gerald J. Meyer. **Poster**. 23rd Winter Inter-American Photochemical Society Meeting, Sarasota, FL, January 2-5th, 2014.

Excited-State Relaxation of Ruthenium Polypyridyl Compounds Relevant to Dye-Sensitized Solar Cells. Ryan M. O'Donnell, Patrik G. Johansson, Maria Abrahamsson, & Gerald J. Meyer. **Oral**. 245th American Chemical Society National Meeting, New Orleans, LA, April 11th, 2013.

Homoleptic Ruthenium "Star" Compounds Containing Triazole Linkers for Use in Dye-Sensitized Solar Cells. Ryan M. O'Donnell, Keyur P. Chitre, Elena Galoppini, & Gerald J. Meyer. **Oral**. 245th American Chemical Society National Meeting, New Orleans, LA, April 10th, 2013.

Excited State Deactivation Pathways of Ruthenium Polypyridyl Compounds Relevant to Dye-Sensitized Solar Cells. Ryan M. O'Donnell, Patrik G. Johansson, Maria Abrahamsson, & Gerald J. Meyer. **Poster**, 22nd Winter Inter-American Photochemical Society Meeting, Sarasota, FL, January 2-5th, 2013.

Excited State Deactivation Pathways of Ruthenium Polypyridyl Compounds and Their Relevance to Dye-Sensitized Solar Cells. Ryan M. O'Donnell & Gerald J. Meyer. **Poster**, Electron Donor-Acceptor Interactions Gordon Research Conference, Newport, RI, August 5-10th, 2012.

Photophysical Studies of the Solar Cell Sensitizer N3 – [Ru(dcb)$_2$(NCS)$_2$]. Ryan M. O'Donnell, Patrik Johansson, & Gerald J. Meyer. **Poster**, Photochemistry Gordon Research Conference, Easton, MA, July 10-15th, 2011.

Development of an Optoelectronic Device Based on Ruthenium Sulfoxide Complexes. Ryan M. O'Donnell, Yuhuan Jin, Justin Henthorn, & Jeffrey J. Rack. **Oral**, Ohio Inorganic Weekend, Case Western Reserve University, November 13th, 2009.

Sensitive Detection of Nitroaromatic Explosives. Ryan M. O'Donnell. **Oral**, Lawrence Livermore National Laboratory, August 28th, 2009.

Detection of Marijuana and Cocaine Metabolites in Adulterated Urine Using Solid Phase Extraction – Ion Mobility Spectrometry and Gas Chromatography – Mass Spectrometry. Ryan M. O'Donnell and Peter de B. Harrington. **Oral**, Pittsburgh Conference on Analytical Chemistry and Applied Spectroscopy, New Orleans, Louisiana, March 5th, 2008.

Applications of Ion Mobility Spectrometry and Differential Mobility Spectrometry in Drug Screening and Quality Control of Pharmaceuticals. Ryan M. O'Donnell and Peter de B. Harrington. **Poster**, Central Regional Meeting of the American Chemical Society, Covington, Kentucky, May 20-23, 2007.

OUTREACH & VOLUNTEER EXPERIENCE

Feb. 15th, 2014: **Johns Hopkins Math Tournament:** Volunteered at the 14th annual math competition attended by more than 200 local high school students.

May 29th, 2012 & May 31st, 2013: **Baltimore Polytechnic High School Chemistry Demonstrations.** Taught principles of combustion reactions and Tollens' Reagent to groups of 20 Advanced Placement high school chemistry students through hands on experiments and discussion.

Oct. 2011/2012/2013: **Science Night at Halstead Academy of Science and the Arts**. Performed rubber polymerization and scent diffusion experiments with elementary school students and their parents as part of an after-school science demonstration event. Approximately 275 students attended.

Oct. 2012/2013: **ACS National Chemistry Week.** Performed hands on experiments with 5th grade students at Riverview and Cross Country elementary schools in Baltimore. Topics included serial dilutions of dye molecules, hydrophobicity, magnetism with ferrofluids, and constructing batteries from household items (Cu/Zn).

March 2011/2012: **Maryland Science Olympiad Judge and Event Coordinator.** Prepared and oversaw the Maryland State "Optics" event for middle and high school students and a Regionals Tournament "Compute This" event for middle school students.

PROFESSIONAL MEMBERSHIPS

2012 – Present: **Inter-American Photochemical Society Member**
2009 – Present: **American Association for the Advancement of Science.**
2006 – Present: **American Chemical Society.** Division of Inorganic Chemistry member.

REFERENCES

Dr. Gerald J. Meyer – Graduate Research Advisor
Dept. of Chemistry, University of North Carolina, 919-962-6320, gjmeyer@email.unc.edu

Dr. D. Howard Fairbrother – Thesis Committee Member
Dept. of Chemistry, Johns Hopkins University, 410-516-4328, howardf@jhu.edu

Dr. Jeffrey J. Rack – Undergraduate Research Advisor
Dept. of Chemistry, Ohio University, 740-593-9702, rackj@ohio.edu